Theory and Applications of a Uniplanar Transmission-Line Metamaterial-Inspired Electromagnetic Bandgap Structure

by

Stuart Barth

A thesis submitted in partial fulfillment of the requirements for the degree of

Master of Science

in

Electromagnetics and Microwaves

Department of Electrical and Computer Engineering

University of Alberta

Abstract

A multitude of planar electromagnetic bandgap structures (EBGs) have been proposed for the suppression of parallel-plate waveguide (PPW) and surface-wave (SW) modes at microwave frequencies. Some of these structures have been well-modelled with transmission-line theory, however, these structures typically employ vias which prevent these structures from being used at high frequencies or in low-cost applications, where vias can be difficult or expensive to manufacture. Alternatively, EBGs have been proposed which overcome this limitation with a uniplanar design, such that they are simple to manufacture using standard lithographic processes. However, these structures generally suffer from the lack of a rigorous model, such that the bandgap properties are difficult to control without changing the overall size of the EBG.

This work seeks to overcome this limitation through the development of a uniplanar EBG structure which is shown to be well-described by a proposed multiconductor transmission-line model. Transmission-line metamaterial techniques are then used to miniaturize the EBG's constituent unit cells, without any loss of model accuracy. Although this EBG is inherently one-dimensional, it is shown that it can be arranged radially to effect suppression in two dimensions.

The EBG is created by loading the coplanar waveguide (CPW) conductors of a shielded, conductor-backed CPW (S-CBCPW) structure with series capacitors and shunt inductors, as inspired by transmission-line metamaterials. The bandgaps used in this work are shown to arise through modal coupling, in which the loaded CPW mode couples with the PPW and/or SW modes to prevent the transmission of power.

To demonstrate the effectiveness and versatility of this EBG, it is applied to two applications: the suppression of parallel-plate noise between two vias at X-band, and the suppression of the SW mode on a GPS antenna ground plane at L-band. It is shown that the full-wave simulated results agree well with the periodic analysis of the equivalent-circuit model developed in this work. Finally, the designed EBGs were manufactured and tested to verify these results. Several avenues of further study and applications are suggested.

Acknowledgements

I would like to begin by thanking my supervisor, Prof. Ashwin K. Iyer, for his support, guidance, and confidence in me. I have been privileged to work under someone who is not only an outstanding teacher, but also a passionate researcher who sets an example by seeking out the fundamental truth – no matter how obscure or mundane it might seem. His regular questioning of seemingly basic data undoubtedly shaped and refined this work into what it is.

Special thanks to my fellow graduate students – it wouldn't have been the same without you. I greatly appreciated all the stimulating conversation, and I only hope that it helped you as much as it helped me.

I would like to thank our lab managers Justin Pollock and Sanghamitro Das for their support with some of the antenna measurements – your time and assistance was much appreciated.

I would like to acknowledge the Natural Sciences and Engineering Research Council and NovAtel Inc. for sponsoring this research through a NSERC Collaborative Research and Development grant. Special thanks to Jerry Freestone and Ahmad Chamseddine at NovAtel for their support over the duration of this project, and to Tom for assistance with measurements.

Support was also provided by Rogers Corporation in providing substrates through their University program, and LPKF Laser & Electronics AG in providing the high quality X-band prototypes. The MATLAB code used to calculate dispersion based on the equivalent-circuit models employed DistMesh, a free meshing program created and maintained by Per-Olof Persson.

Lastly, I would like to thank my family - my mother, father, and my amazing wife Carly for their support over the length of this endeavor. For this, I am truly grateful.

Contents

List of Acronyms

EBG	Electromagnetic Bandgap Structure
TM	Transverse Magnetic
TL	Transmission Line
TEM	Transverse Electro-Magnetic
TE	Transverse Electric
MTL	Multiconductor Transmission Line
UC-EBG	Uniplanar Compact Electromagnetic Bandgap Structure
PBG	Photonic Bandgap Structure
DGS	Defected Ground Plane
FSS	Frequency Selective Surface
HIS	High Impedance Surface
AMC	Artificial Magnetic Conductor
SW	Surface Wave
GPS	Global Positioning System
TL-MTM	Transmission-line Metamaterial
CRLH	Composite Right-Left Handed
CBCPW	Conductor Backed Coplanar Waveguide
PPW	Parallel Plate Waveguide
CPW	Coplanar Waveguide
CSL	Coupled Slot Line
S-CBCPW	Shielded Conductor Backed Coplanar Waveguide
PMC	Perfect Magnetic Conductor
FEM	Finite Element Method
PBC	Periodic Boundary Condition
PML	Perfectly Matched Layer
HFSS	High Frequency Structural Simulator
PCB	Printed Circuit Board
SI	Signal Integrity
PI	Power Integrity
SIW	Substrate-integrated Waveguide
SMA	Sub-miniature A
LHCP	Left Hand Circularly Polarized
RHCP	Right Hand Circularly Polarized
AR	Axial Ratio
MPR	Multipath Ratio
L1	GPS L1 Frequency
L2	GPS L2 Frequency

List of Symbols

γ	Propagation Constant
k	Free Space Phase Constant
β	Phase Constant
Γ	Brillouin Gamma Point
X	Brillouin X Point
α	Attenuation Constant
ω	Angular Frequency
v_ϕ	Phase Velocity
v_g	Group Velocity
ϵ	Relative Permittivity
μ	Relative Permeability
d	Unit Cell Period (Direction of Propagation)
w	Unit Cell Width
s	CPW Strip Line Width
g	CPW Gap Width
h_u	Upper Dielectric Height
h_l	Lower Dielectric Height
t	Trace Thickness
γ_B	Bloch Propagation Constant
C	Capacitance
L	Inductance
Z_o	Characteristic Impedance
Y	Admittance
Z	Impedance
T	Diagonalization
γ_M	Modal Propagation Constant
ϵ_0	Vacuum Permittivity
μ_0	Vacuum Permeability
w_L	Inductor Width
l_{gc}	CPW Grounds Capacitor Length (g_c)
w_{gc}	CPW Grounds Capacitor Width
C_g	CPW Grounds Capacitance
C_s	CPW Strip Line Capacitance
R	Radial Component
θ	Angular Component
w_a	Average Unit Cell Width
g_{fg}	CPW Grounds Interdigitated Capacitor Finger Gap Width
w_{fg}	CPW Grounds Interdigitated Capacitor Finger Width
l_{fg}	CPW Grounds Interdigitated Capacitor Length
N_{fg}	CPW Grounds Interdigitated Capacitor Number of Fingers
g_{fs}	CPW Strip Line Interdigitated Capacitor Finger Gap Width
w_{fs}	CPW Strip Line Interdigitated Capacitor Finger Width
l_{fs}	CPW Strip Line Interdigitated Capacitor Length
N_{fs}	CPW Strip Line Interdigitated Capacitor Number of Fingers
c	Circular EBG Layout Inner Diameter
e	Circular EBG Layout Outer Diameter

List of Tables

List of Figures

Chapter 1

Introduction

1.1 Motivation

Planar structures have become nearly ubiquitous in the realization of microwave circuits, for example in the form of either printed circuit boards or monolithic microwave integrated circuits. Periodic planar structures with which microwave power can be transmitted [1–4], or suppressed [5–9], have been of great interest recently due to relatively simple design processes based on circuit and transmission-line theory. One preferred class of these structures are electromagnetic bandgap structures (EBGs), which operate by reflecting or redirecting/coupling incident power into other modes or propagation directions, over distinct frequency bands referred to as bandgaps.

The canonical example of an EBG is the Sievenpiper mushroom structure, which consists of "islands" of metal on top of a dielectric shorted to a common conductor backing with a via, as described in [10]. The bandgap properties of this structure can be simply described in terms of the loading inductance created by the structure's via, the loading capacitance created by the gaps between the edges of the structures, and the structure's period [11, 12]. Due to its relatively simple construction and the precise control of the suppressing frequency range offered by this device, the Sievenpiper and similar structures have been widely studied [7, 13–16].

Since many of these structures have been analyzed in detail, attention has been turning more recently to their efficient realization. Many planar microwave devices rely on the fabrication of non-planar elements such as vias between layers, which is still relatively difficult and/or expensive in miniaturized devices [17–19]. Subsequently, it is desirable that these devices be uniplanar such that they they can be simply manufactured in a cost-efficient process. Uniplanar devices are those which have all of their physical features existing on a single plane, but also may make use of solid conductors above and below this plane.

Many such structures have been proposed [20–24], which operate similar to the Sievenpiper structure in suppressing the transmission of power over one or more given frequency bands, but are uniplanar and as such can be efficiently manufactured. However, these structures generally suffer from the lack of a comprehensive and rigorous theoretical analysis by which to simply design their power transmission properties.

Furthermore, it is desired that these structures be miniaturized, since they typically have a period on the order of one-quarter to one-half of a guided wavelength. It has been demonstrated [25, 26] that metamaterial techniques can be used to miniaturized microwave circuits. A special class of metamaterials – transmission-line metamaterials – has been shown to integrate well into existing microwave circuit topologies with the use of simple reactive circuit components (i.e., inductors and capacitors), and furthermore can be simply modelled with transmission-line and circuit theory. These reactive components can be created in uniplanar environments, such that these techniques can be directly applied to uniplanar EBGs.

This thesis seeks to combine the excellent modelling of the Sievenpiper and related planar structures with the ease of fabrication afforded by uniplanar structures, to create a novel uniplanar EBG which can be well modelled with a high level of rigorous theoretical analysis. This will be accomplished with the use of a multiconductor transmission-line model and transmission-line metamaterial miniaturization techniques. In order to validate the performance of this structure, it will be applied to solve two common problems involving the suppression of microwave power: the suppression of parallel-plate noise in printed circuit board environments, and the suppression of the TM_0 surface-wave mode in global positioning system antenna ground planes.

1.2 Background

1.2.1 Periodic Structures

The periodic structures examined in this work are simply one or two-dimensional waveguides that have been periodically "loaded" with inclusions. Under this condition, the waveguide is known as the "host" and the inclusions are referred to as the "loading". While realistically, the inclusion of loading elements into a waveguide causes the waveguide to be discontinuous and allows the excitation of higher order modes, the assumption is generally made that the perturbations introduced by the inclusions are small enough that the waveguide can be considered homogeneous.

An early example of the use of periodic structures in the microwave domain is *artificial dielectrics* [27–31], in which waveguides or free space (the hosts) were loaded periodically by metallic components to yield a desired effective permittivity. Such techniques, whereby it was realized that periodic perturbations could induce an effective macroscopic response, were largely responsible for later developments involving periodic structures which led to metamaterials. A later example is known as *Yablonovite*, named after the researcher who both developed it theoretically [32] and later realized it [33]. Essentially, the material is a simple dielectric with a periodic array of holes drilled through it. In this case, the dielectric is the host

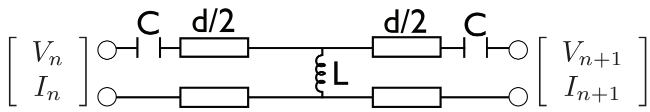

Figure 1.1: Example of a periodically loaded transmission-line.

and the loading is the holes. Transmission-line modelling is ideal for such structures, due to its combined simplicity and accuracy.

Transmission-Line Based Periodic Structures

Early applications of transmission-line (TL) theory for the design of periodic structures include microwave filters [34], for which lower-frequency filter theory was already well established without using TLs, and the analysis of artificial dielectrics [28]. The inclusion of TLs has allowed for extremely accurate modelling, and subsequently is used extensively in this work. One drawback of this technique is due to the limitation of TL theory to TEM modes: non-TEM modes cannot be modelled to the same level of accuracy (some TE and TM modes can be approximated using TL theory [35]).

The periodic inclusions of the periodic structure then must also be modelled in the circuit domain if they are to be integrated with TLs. Typically, these take the simple form of individual inductors or capacitors, but may be modelled as more complex networks. An example TL-based periodic structure is shown in Fig. 1.1. In this case, the TL is the host and the inclusions are the inductors and capacitors. Node index notation for an infinite structure is used, in which the left-hand terminal is designated node n, and the right-hand terminal is designated node $n+1$.

Bloch's Theorem

The periodic nature of these structures is analyzed by applying periodic boundary conditions to a single period (referred to in this work as a "unit cell"). Under the assumption that every period is identical, the fields take on properties such that (in the case of a one-dimensional array in x):

$$\begin{bmatrix} \vec{V}_{n+1} \\ \vec{I}_{n+1} \end{bmatrix} = \begin{bmatrix} \vec{V}_n \\ \vec{I}_n \end{bmatrix} e^{-\gamma d} \tag{1.1}$$

This result (for either voltages or currents) is known as *Bloch's* theorem [35], although the formulation used here is also referred to as *Floquet's* theorem [36–38]. This theorem allows for the extraction of the *Bloch modes* (with complex propagation constants γ) from a given unit cell. Bloch modes are the resulting periodic modes supported by the waveguide once the periodic loading is taken into account. It is the engineering of these Bloch modes that is studied in this work.

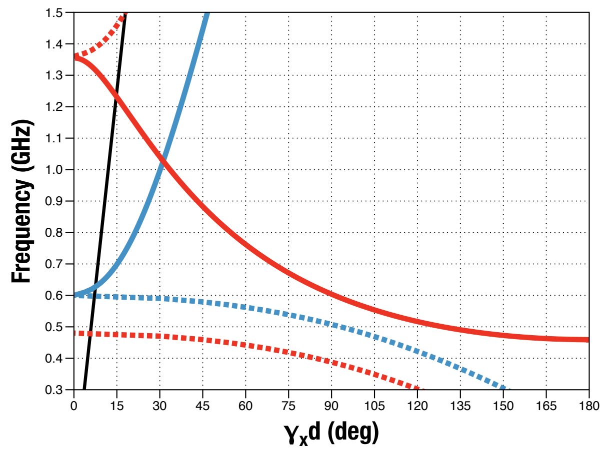

Figure 1.2: Example dispersion diagram showing both the real (dashed) and imaginary (solid) components of the propagation constants for two independent modes (red and blue).

1.2.2 Electromagnetic Bandgap Structures

Dispersion

EBGs are periodic structures which are specifically employed for their ability to suppress the propagation of one or more supported Bloch modes over certain frequency ranges. These modes will be displayed in *dispersion diagrams* (also known as $k-\beta$ diagrams) [39], which in this work will plot the complex *propagation* constants of various modes versus frequency. These diagrams will plot the propagation constants as observed along the principal directions of the irreducible Brillouin zone [41] – specifically those *propagating* (incurring phase) in the positive direction. In the Brillouin-zone diagram, the domain is transformed into the product of the propagation constant and the period of the structure in the direction of propagation being investigated, and is bound between 0 and π radians [42]. These endpoints are known as Γ and X, respectively – this terminology will be used extensively in this work.

An example dispersion diagram is shown in Fig. 1.2. The propagation constant is plotted on the horizontal axis (which corresponds to propagation along the x-axis in this example, as indicated by the subscript), and frequency is plotted on the vertical axis. A single diagram, as in this case, can only be used for a single direction of propagation – however, most waveguides are designed to guide waves in one dimension. In the dispersion diagrams presented in this work, both the real and imaginary (or attenuation and phase, respectively) components of the propagation constant will be shown where possible, where $\gamma = \alpha + j\beta$. Unless labeled otherwise, the solid lines will correspond to the imaginary components (β), while the dashed lines will correspond to the real components (α). The solid black line will always be shown for reference; it represents the dispersion of light in a vacuum. Different colors will be used to indicated different modes – in this example, the red and blue curves correspond to two independent modes. Although the diagrams will state that the dispersion is measured in terms of the imaginary component (degrees, in this case), the real component is, of course, measured in the analogous units of Nepers.

The term *dispersion* refers to the phase incurred per unit length of a given mode (the mode's phase constant) as a function of frequency. Modes which are referred to as non-dispersive have a linear relationship between incurred phase and frequency, whereas dispersive modes do not. Specific points on the dispersion diagram indicate the phase velocity of the modes. Specifically, the phase velocity of a mode at any point is related to the slope of the line from the origin to that point, determined by the equation

$$v_\phi = \frac{\omega}{\beta} \tag{1.2}$$

The group velocity is related to the slope of a line tangent to a mode's dispersion curve at any point. One physical interpretation of the group velocity is that it is the velocity of power transmission [40]. This is a critical definition to the objective of this work, since it implies that *power transmission can be controlled through the dispersive properties of waveguides.* For this reason, this work primarily involves the study of dispersion, and will only use scattering parameters to verify the observed dispersive properties. Group velocity is formally defined as

$$v_g = \frac{\partial\omega}{\partial\beta} \tag{1.3}$$

It is worth noting that modes can exist on either side of the light-line – indicating that the mode has either a larger or slower phase velocity than that of light. Transluminal velocities are not problematic – so long as the group velocity is smaller than the speed of light, causality is satisfied. The area inside the light-line is referred to as the "fast-wave" region for this reason, and similarly, the area outside of the light-line is referred to as the "slow-wave" region.

Modal Coupling

Modal coupling is a behavior described by coupled-mode theory [43], which explains that if modes with similar field profiles and dispersion angles exist at a given frequency, then the modes will couple to one another, and the dispersive properties of both will merge, forming a new, coupled mode containing properties of both isolated modes. An example of this behavior is shown in a dispersion diagram in Fig. 1.3, in which the isolated modes are shown along with the result of both weak and strong coupling. This coupling will be employed extensively in this work, as it is an extremely useful tool in the design of bandgap structures.

Backward Waves

It can be seen on the example diagram that the imaginary component of the propagation constant corresponding to the red mode in Fig. 1.2 possesses a negative slope. A negative slope, corresponding to a negative group velocity, is not unphysical, but rather indicates power being transmitted in the opposite

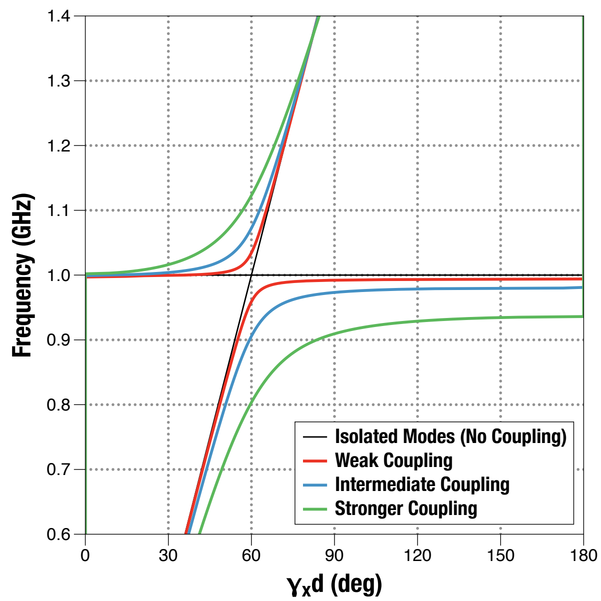

Figure 1.3: Example of the effects of modal coupling strengths on the dispersive properties of two modes.

direction from that of the forward modes. It should be noted that the phase velocity is still positive – that is, it possesses the opposite sign of the group velocity. This particular type of propagation (where the phase and group velocities are *anti-parallel*, is known as *backward-wave* propagation, and has been observed in electrical circuits for several decades [44, 45].

Complex Modes

When forward and backward modes couple, this coupling can result in the formation of *complex* modes [46]. These modes possess propagation constants with both real and imaginary components of the same order of magnitude, even in the absence of ohmic losses. Furthermore, for an infinite periodic structure, the net power carried by these modes in a given direction is zero, even though their group velocity is non-zero. Complex modes always exist in conjugate pairs for which $\gamma = \alpha \pm j\beta$. These two modes often possess different magnitudes, depending on excitation [47], but the net result is always zero power flow (in infinite structures). The physical interpretation of these modes is that power is transmitted by the forward constituent mode, but simultaneously coupled into the backward mode, such that the net result appears to be a lack of power transmission. The rate at which the power decays, and the phase it incurs while propagating, is given by the real and imaginary components, respectively, of the complex mode.

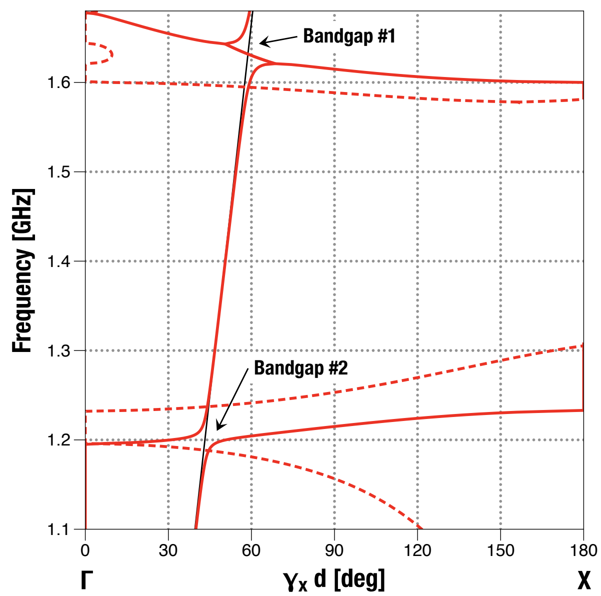

Figure 1.4: Dispersion diagram indicating two classes of bandgap. Bandgap #1 meets common definitions of a bandgap, while bandgap #2 meets only the definition given in this work.

Bandgaps

Traditionally, the term *bandgap* is derived from the semiconductor or optical domains, in which electrons or photons possessing a certain energy (proportional to frequency) cannot exist in a given structure (also known as a *forbidden* band). When used in the microwave domain, a bandgap is traditionally defined as a frequency range inside which a given mode, as well as modes with which it couples, do not propagate or are attenuated with distance in the absence of losses.

This definition will not be used in this work. Instead, a slightly modified definition will be used which reflects the developments described in Appendix A. A bandgap in the context of this work is hereby defined as a frequency range over which a given *isolated* mode does not propagate. This could be either because it is reflected or because it is coupled into other modes. An example of the differences between these two definitions is given in Fig. 1.4, in which the higher frequency bandgap (#1) satisfies both definitions of a bandgap, whereas the lower frequency bandgap (#2) only satisfies this work's definition of a bandgap. Both may be classified as bandgaps due to the fact that they redirect, or couple, energy out of the incident modes into a number of other modes. While attenuation (corresponding to reflection, or coupling into backward-directed modes) is observed in bandgap #1, it is not present in #2, since there is no reflection, but merely coupling into other forward-directed modes.

Bandgaps as studied in this work arise due to two distinct mechanisms. The first is due to modal *cutoff*, in which the mode has a propagation constant that is purely real (i.e., evanescent). The second mechanism is due to modal coupling. When modal coupling occurs, the Bloch modes take on dispersive properties which are a combination of their isolated counterparts. The fact that the isolated Bloch modes are not

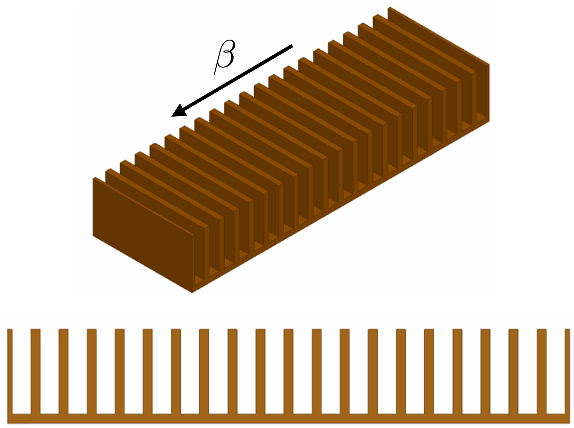

Figure 1.5: Layout of a corrugated metallic ground plane. Propagation is considered in the direction indicated. The structure is shown from an isometric viewpoint as well as from the side.

supported meets the definition of a bandgap used in this work.

Canonical EBGs

Bandgaps were first studied in the microwave domain in structures such as the previously introduced Yablonovite, which is classified as a *photonic crystal*. Photonic crystals are periodic structures arranged into a defined lattice, which generally exhibit bandgap behaviors attributed to Bragg scattering [48]. As such, it is generally agreed upon that photonic crystals have periods on the order of one-quarter to one-half of a guided wavelength, limiting their practicality for use in microwave applications which generally desire miniaturized solutions.

One of the first EBG structures developed was the corrugated ground plane [49, 50], although it was not recognized at the time as an EBG (the term, or even its progenitors, had not yet been created), as the study of the dispersive nature of periodic structures was still under development. The structure consists of a series of slits or grooves cut vertically into a solid conductor, as shown in Fig. 1.5. The EBG operates on the principle of transverse resonance as applied to the grooves, each of which behaves as a shorted TL, and therefore resonates when excited with frequencies for which the depth of the groove correspond to odd integer multiples of one-quarter of a wavelength.

As previously noted, one canonical EBG is the Sievenpiper mushroom structure (also named for the researcher who developed it), a constituent unit cell of which is shown in Fig. 1.6a. This EBG was initially introduced as a *photonic* bandgap structure (PBG), in reference to the photonic crystal structure after which it was modelled [10]. The unit cell consists of a PPW-type waveguide with gaps in the metallization of the top face, giving rise to "islands" of metals, and a via in the center of these islands connecting the top layer to the bottom. The suppression mechanism was described as an isolated *LC*

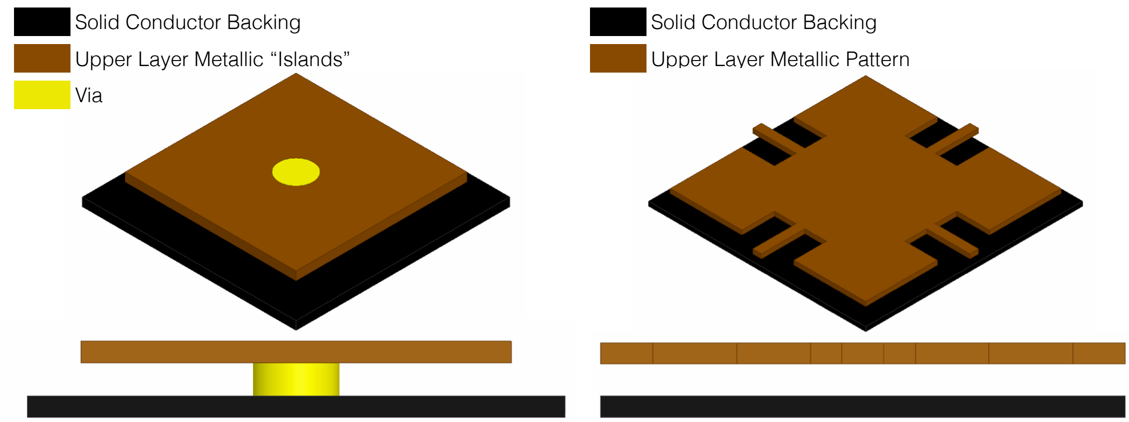

(a) (b)

Figure 1.6: Layout of a) the Sievenpiper mushroom structure, b) the UC-EBG structure. Both shown from an isometric viewpoint as well as from the side.

resonance, caused by a current loop through the via (modelled as an inductor) and the gaps between the metallic islands (modelled as a capacitance).

Another classic EBG structure is the *uniplanar compact* EBG (UC-EBG), a constituent unit cell of which is shown in Fig. 1.6b [51]. This EBG's unit cell consists of the patterning of the upper metallic layer of a substrate, and is typically backed by a solid conductor. The patterning is done in such a way that an LC resonance is formed by thin metallic strips (modelled as an inductor) and the gaps on either side of the conductors (modelled as capacitors).

A third EBG that has been extensively studied in the literature is the *shielded* Sievenpiper structure [47, 52–54]. This structure is identical to the Sievenpiper structure, with the exception that it is shielded above the second layer by a solid metallic conductor. Under this condition, the bandgap properties of the unit cell can be accurately determined with a MTL equivalent-circuit model.

EBG Pseudonyms

EBGs are also referred to in the literature with several different titles. However, many of these titles are not used to describe the bandgap behavior of EBGs, rather slightly different properties, and will therefore not be used in this work.

- Photonic Bandgap Structures (PBGs) were the historical origins of EBGs, for which the term "bandgap" is derived from the optical or semiconductor fields [51, 55]. As these structures were developed in the microwave field, the term "EBG" was used instead to indicate the designed operating frequency range.

- Defected Ground Structures (DGSs) are sometimes considered to be EBGs, but more generally are uniplanar structures which are created by selectively inserting gaps into solid ground planes [56,57]. Typically, these structures are not periodic, and therefore lack a rigorous means for analysis and are instead analyzed by investigating the resulting flow of currents on the ground plane alone [58].

- Frequency Selective Surfaces (FSSs), or Partially Reflecting Surfaces (PRSs) are also described as being related to EBGs in the literature [59–61]. However, the most common use of these devices in the majority of the literature is as a surface on which a free-space plane wave is incident normally or at an oblique angle. Since typically EBGs operate on guided modes travelling along a surface, FSSs and PRSs do not generally meet this definition.

- High Impedance Surfaces (HISs) and Artificial Magnetic Conductors (AMCs) are terms used to described a class of EBGs which are characterized by observing the reflection properties of an incident plane wave [10, 59]. Specifically, these structures are described as having ideal magnetic conductor properties at the frequency at which the reflection phase of an incident plane wave is zero degrees. It is generally understood that this magnetic conductor does not support TM_0 SW modes, and therefore acts an EBG for these surface wave modes. However, the characterization of these structures does not strictly find the properties of guided-wave modes, which EBGs are generally assumed to act on.

1.2.3 Parallel-Plate Noise Suppression

Modern printed-circuit boards for high-speed circuitry must increasingly compensate for the effects of "cross-talk" due to increasing number of layers, correspondingly thinner layers, increased trace and component density, and increased coupling due to higher clock frequencies and data throughput. One particular challenge in these systems is created by the routing of signals between layers through the use of metallized vias. When higher frequency signals pass through these vias, energy is parasitically coupled into modes supported by the dielectric – usually the parallel-plate mode guided by the solid power and/or ground planes on both sides of the dielectric [62]. This parallel-plate mode propagates through the surrounding medium, as depicted in Fig. 1.7a, where it can be coupled back into other traces and appear as noise, which can cause interference, false signalling, and generally degrade the performance of the hosted circuitry [63]. For this reason, the efficient suppression of the parallel-plate mode radiated by these vias is desired to maintain power and signal integrity in these systems.

Early methods of suppressing this noise consisted of *decoupling* (or *bypass*) capacitors [64, 65], which effectively short the two plates together at high frequencies. However, these only work for relatively low-frequency signals and higher frequency noise. A similar effect has been achieved by *embedded capacitance layers* [66, 67], in which the power and/or ground planes are spaced as closely as possible as to increase the capacitance between them, effectively shorting out high-frequency noise. Defected ground structures have also been used to suppress parallel-plate noise in multiplayer printed circuit boards, by reflecting incident microwave power, but their design is often highly empirical and lacks any unifying theory of

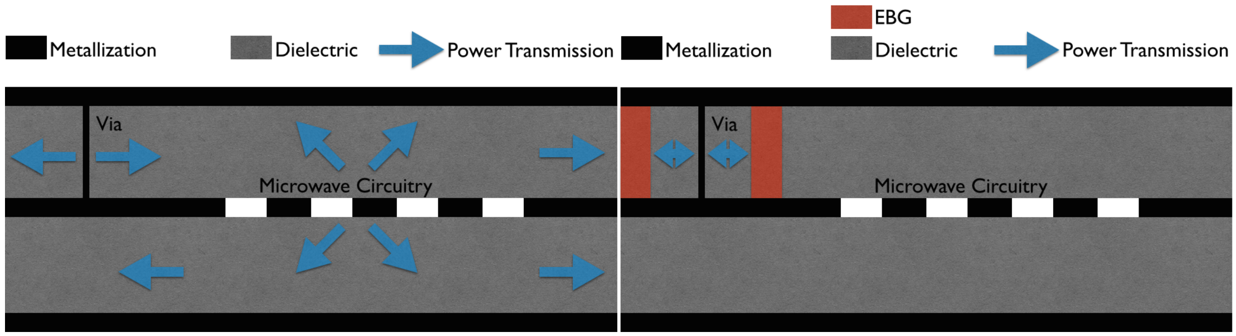

(a) (b)

Figure 1.7: Via-induced parallel-plate noise a) without suppression mechanism, b) with EBG suppression mechanism.

operation [68–71]. EBGs have been widely adopted [72–74] due to their ability to reflect microwave power similar to the defected ground structures, but also due to a deep level of understanding afforded by rigorously accurate models, allowing for a very well-defined design process. However, the structures used in this particular application fit the same categories as previously described: they are either uniplanar, or well-modelled, but not both.

One of two applications in this work investigates the suppression of parallel-plate noise at X-band by arranging EBGs around the vias such that the power reflects backwards, as depicted in Fig. 1.7b. A uniplanar, printable solution is investigated, such that the EBG is both easily integrated into the existing structure and suitable for high frequency operation.

1.2.4 Surface-Wave Suppression

The recent rise in the use of satellite-assisted positioning systems, such as the global positioning system (GPS), driven in large part by integration into a myriad of consumer electronic devices and other commonplace systems [75], has further increased the desire for positioning accuracy. While positioning signals transmitted by these satellites are of incredible precision, there are numerous factors which cause inaccuracies when the signals are received on the earth's surface. Even though effects such as the dispersion of the ionosphere and time dilation due to the planet's gravitational field are taken into account, more localized effects such as multipath interference, noise or signal distortion cause positioning inaccuracies [76].

Multipath interference is the phenomenon in which a signal is transmitted to a receiver along more than one physical path. Ideally, only one signal path exists – from the transmitting satellite, in a direct line-of-sight path to the receiver. However, due to the presence of other objects (typically large ground structures such as buildings) those signals can be reflected multiple times, and some of these reflections can arrive at the receiver after a significant time delay from the direct line-of-sight signal, causing an inaccuracy in the estimation of position. Signals reflected an odd number of times possess the reverse polarization (left-handed circularly polarized) from the original signal (which is right-handed circularly polarized), such that the majority of multipath signals possess left-handed circular polarization.

However, these reflected signals have been found to travel to the receiver near the horizon at an angle tangential to, or lower than, a plane parallel to the ground, as shown in Fig. 1.8. The coupling into surface waves at the edge of the ground plane allows the antenna to receive both right- and left-handed circular polarizations, since typically only the linearly polarized TM_0 surface wave (from hereon the term "SW" will imply the TM_0) mode is supported by the ground planes in this frequency range. It is this reception of left-handed circularly polarized signals which is undesired, and caused by this transmission of surface waves along the ground plane.

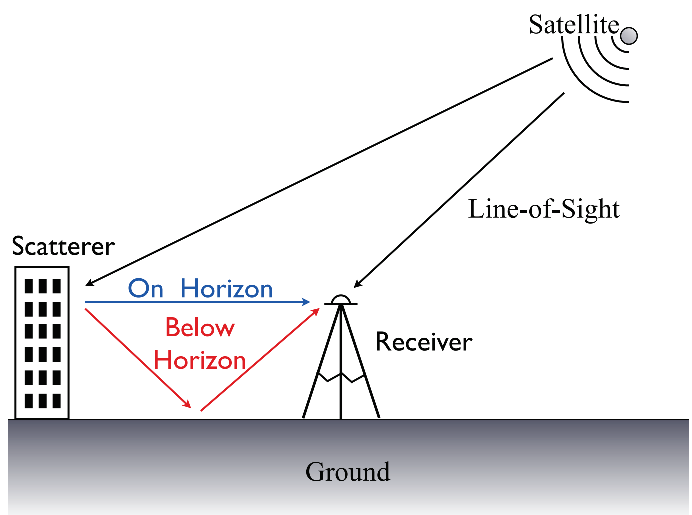

Figure 1.8: Example of Multipath Interference from a Satellite

Current solutions to this problem include suppressing the TM_0 surface-wave mode by surrounding the antenna with *corrugations*, which in a circular layout form *choke rings* [77, 78], which are generally expensive, physically large, and heavy. However, these undesirable factors are mitigated by the excellent surface-wave suppressing performance offered by these devices. An ideal solution would be one which offered a similar performance, but in a smaller, lighter form.

Such a solution was proposed in the Sievenpiper mushroom structure [10], and was quickly followed by other EBGs [5, 79]. Many of these EBGs were described as "high impedance surfaces" (HISs), or "artificial magnetic conductors" (AMCs), due to the fact that they present a high *surface* impedance to a normally incident plane wave, similar to an ideal (and fictitious) magnetic conductor. It has been implied that this surface impedance condition causes a SW mode propagating along the EBG surface to experience cutoff at the frequency which the EBG imitates an AMC. When applied to antenna ground planes, many of these designs involving EBGs cause the ground plane to be electrically large. Additionally, the common use of rectangular EBGs reduces the field symmetry around the ground's azimuth.

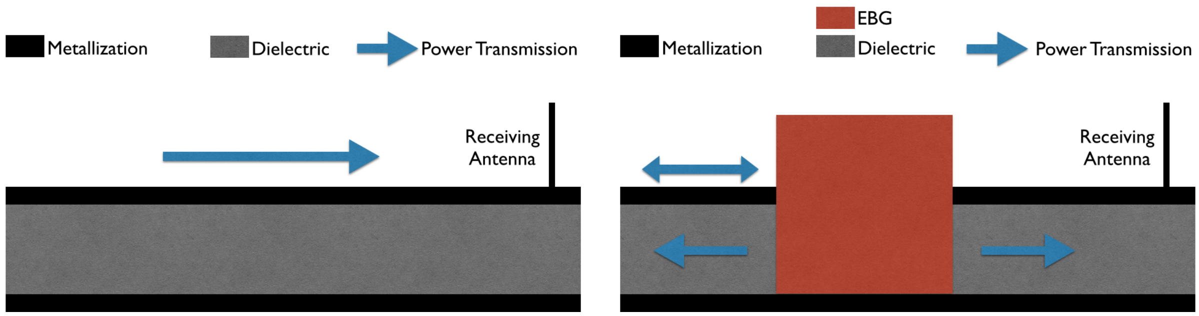

(a) (b)

Figure 1.9: Surface-wave transmission on an antenna ground plane a) without suppression mechanism, b) with suppression mechanism.

Another type of SW suppressing device is the *resistive* ground plane. This device is simply a surface to which a high resistivity has been applied, such that SWs travelling on it experience a high per-unit-length dissipation [80, 81].

The second of two applications in this work investigates the requirements to mitigate the effects of multipath interference by suppressing the SW mode, specifically by engineering the dispersive properties of the antenna ground plane. This is accomplished by preventing the SW mode from propagating, as shown in Fig. 1.9a – but unlike the previous cases of parallel-plate noise suppression, reflection of the power is not the only option. The power of the SW mode could also be coupled into other modes, so long as these modes are not received by the antenna – for example the parallel-plate mode of the metallized dielectric, as shown in Fig. 1.9b. Again, a preferred solution would be one that is uniplanar and printable, such that it is both easily integrated into the existing structure and easily manufactured in low-cost applications.

1.2.5 Metamaterials

The field of metamaterials involves engineering structures in such a way that they mimic and/or extend the behavior found in natural materials. The engineering of electromagnetic metamaterials in the microwave domain involves the creation of large periodic arrays of structures which resemble the arrangement of atoms or molecules in natural materials, so as to provide a macroscopic electromagnetic material response – i.e., an effective *relative* permittivity (ϵ) and permeability (μ) [82].

Some realizations of artificial dielectrics [27–29], as well as artificial electric and magnetic plasmas [30, 31], could be classified as metamaterials, although much of this work was done previous to the development of the metamaterials concept. Importantly, metamaterials have also used to create *left-handed* materials, which possess properties that cannot be found in natural materials [83, 84].

It has been demonstrated that metamaterials can also be realized through the use of TLs, resulting in TL-metamaterials (TL-MTMs) [85] (also referred to as composite right-left handed (CRLH) metamaterials [86]). TL-MTMs possess the advantage that their electrical size can be strongly determined by the values of their loading components, allowing larger factors of miniaturization than possible with other types of microwave metamaterials [25, 26].

The macroscopic response of a metamaterial is limited to the domain over which its constituent unit cells are electrically small. The limit of this domain is known as the *effective-medium* limit, and is usually taken to be $d \leq \lambda_g/10$, where λ_g is the guided wavelength of a specified Bloch mode supported by the unit cell. According to this definition, EBGs may or may not be classified as metamaterials. However, in this work, miniaturization techniques designed for TL-MTMs will be applied towards the miniaturization of EBG unit cells – such that the EBGs are less dependent on their period and more dependent on their propagation properties. Subsequently, since these periodic structures are generally too large to meet the effective-medium limit, the EBGs used in this work cannot strictly be considered metamaterials in the effective-medium sense, and so material parameter extraction will not be performed. However, as their operation will be described in terms of TL-MTM theory, they may be described as metamaterial-based or metamaterial-inspired.

1.3 Thesis Contribution and Layout

The theory and analysis of a uniplanar EBG structure is developed in chapter 2. A uniplanar host TL – the shielded conductor-backed coplanar waveguide – is introduced and loaded in a TL-MTM fashion with shunt inductors and series capacitors in the coplanar waveguide. The coupling of the parallel-plate-waveguide and coplanar-waveguide modes results from similar field distributions on the coplanar-waveguide grounds, and allows the uniplanar configuration. A rigorous analytical dispersion equation using multiconductor TL-theory is derived, and the results are compared to full-wave numerical eigenmode simulations. It is shown that the isolated Bloch modes may be extracted by a simple manipulation of the equivalent-circuit model and host TL medium, from which it is observed that the bandgaps arise due to interaction of the isolated modes. The nature of many of the key dispersion points are investigated and related to the equivalent-circuit model. Furthermore, it is demonstrated that the SW mode may be described as quasi-TEM, such that it can be modelled as a parallel-plate waveguide mode in the upper dielectric with the upper shield at a sufficiently large height. A method is introduced whereby the scattering parameters of the SW and the other modes may be extracted from a simulation involving a finite cascade of unit cells. These multi-mode scattering parameters are compared to the obtained dispersion, from which it is observed that the various modes experience different behaviors as predicted by the dispersion. The definition of a bandgap used in this work is validated through observing the scattering response of two coupled forward modes. A design variation is introduced which involves the use of an additional series capacitor, and it is shown that this allows for additional complexity in the designed dispersion of the unit cell. Lastly, it is shown that a cascade of rectangular unit cells can be transformed into a trapezoidal form, which can then be cascaded around a circle to produce an EBG which acts in two dimensions, as required by the following applications.

Chapter 3 details the realization of a parallel-plate-waveguide mode uniplanar EBG. Existing methods for the suppression of parallel-plate-waveguide modes are examined. A single layer, unidirectional EBG is designed to suppress the parallel-plate-waveguide mode between 2.4 and 6.0 GHz. The design is validated through a simulation of a finite number of unit cells, and then a fabricated structure is measured in experiment, which agrees well with the simulation. The parallel-plate-waveguide mode in this case is excited by a microstrip line and taper, for ease of measurement. Next, a dual layer EBG structure for suppression of X-band parallel-plate-waveguide modes in two dimensions was designed with the use of trapezoidal unit cells arranged into a ring. The unit cells were designed through observation of their dispersive properties, which were then verified through simulation of a cascade of three of these unit cells. Finally, a full two-dimensional ring-shaped EBG was simulated, in which the parallel-plate-waveguide mode in this case is excited by two coaxial probes (to simulate vias) inserted into the dielectric. This design was then fabricated and measured in experiment, which agreed well with the simulation.

Chapter 4 details the realization of a uniplanar EBG for the suppression of the TM_0 surface-wave mode in use as a multipath-interference-mitigating ground plane in a GPS antenna. Existing methods for the suppression TM_0 surface-wave modes are examined, followed by the design of a dual-band EBG by the introduction of a third capacitor into the coplanar-waveguide strip line of the EBG's constituent unit cells. The unit cell is designed by use of its simulated dispersive properties, which are then confirmed by investigating the TM_0 surface-wave mode suppression of a cascade of a finite number of unit cells. The unit cells are then transformed into a trapezoidal form, and arranged in a ring similar to the previous chapter. This EBG is then used as the ground plane for a dual-band GPS antenna, and the complete system is simulated to verify that left-handed circularly polarized realized gain and axial ratio are decreased, and multipath ratio is increased, on and near the horizon. The azimuthal far-field patterns are investigated to show that there is high azimuthal stability offered by this EBG. Finally, the EBG ground plane is manufactured and measured with the equivalent antenna element, and it is found that the measured results agree well with the simulation.

Chapter 5 summarizes the results of this work and highlights its key contributions. Related uncompleted studies are outlined, along with directions for future study of this EBG topology and dispersion modelling.

Chapter 2

Theory

2.1 Host Waveguide

A miniaturized, uniplanar EBG for the suppression of parallel-plate or surface-wave modes is sought. The coplanar waveguide structure is ideal because it can be loaded as a TL-MTM (with shunt inductors and series capacitors) in a uniplanar fashion. Furthermore, with the simple addition of a conductor backing, the structure will also be able to interact with parallel-plate type modes.

This waveguide, known as the conductor-backed CPW (CBCPW), is shown in Fig. 2.1, for which propagation is in the x-direction. It consists of four independent conductors, and therefore supports three quasi-TEM modes, as shown in Figs. 2.2a through 2.2c. These modes will be referred to in this work as the parallel-plate waveguide (PPW) mode, the coplanar waveguide (CPW) mode, and the coupled slotline (CSL) mode. This structure also supports a SW mode on the three upper conductors.

However, since this EBG will be used in multi-layer environments, it is appropriate to include an upper shield in the host waveguide as well, as shown in Fig. 2.3, and furthermore it will be shown that such a shield can be used in modelling the SW mode. This structure, the shielded conductor-backed coplanar waveguide (S-CBCPW), will be used for both PPW and SW suppression in this work. The fifth conductor – the shield – supports a fourth quasi-TEM PPW-type mode between the three center CPW conductors and the shield. To distinguish between the two PPW modes in this structure, the modes will be referred to as the “upper PPW” mode (supported in part by the shield) and the “lower PPW” mode (supported

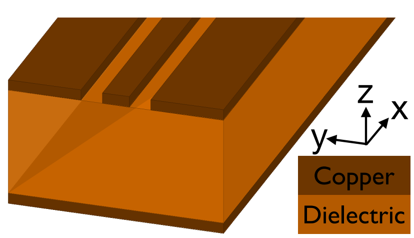

Figure 2.1: Example CBCPW Waveguide

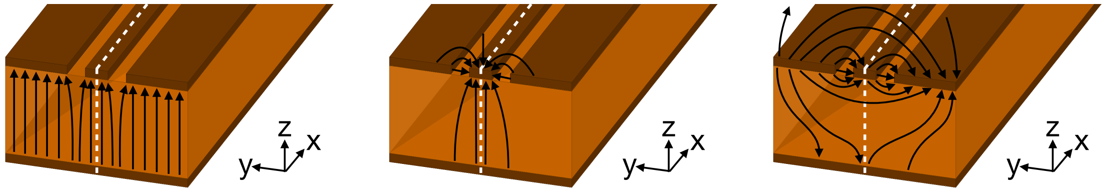

(a) (b) (c)

Figure 2.2: TEM modes supported by the CBCPW structure: a) PPW b) CPW c) CSL.

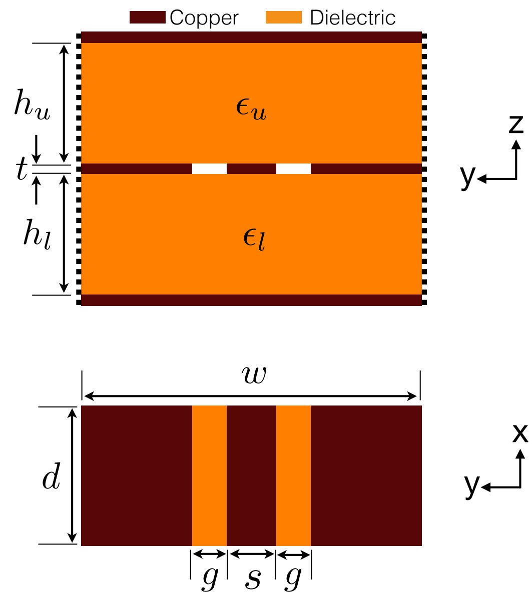

Figure 2.3: Layout of the S-CBCPW structure. The boundary conditions on the side are represented by the dashed lines and correspond to PMCs.

in part by the conductor backing).

Coupled-mode theory predicts that the CPW mode may couple with both the PPW modes, critically because the CPW ground planes support predominantly normal electric fields, similar to the PPW modes. In addition, it also predicts that the CSL mode will not couple with any other of these modes due to the anti-symmetry in its fields. This anti-symmetry can be observed in Figs. 2.2a through 2.2c, in which the white dashed line represents the plane of symmetry, which exists in the z-x plane. Modes which possess electric fields tangent to this plane will be referred to as *even*, while modes which have electric fields normal to this plane will be referred to as *odd*. Even modes couple with other even modes, and odd modes (the only one being the CSL mode, in this structure) only couple with other odd modes. Odd and even modes do not couple.

Consideration of extending this design to a two-dimensional surface which maintains the suppression of PPW modes along one dimension requires modelling periodicity in the transverse direction of the waveguide. Perfect magnetic conductors (PMCs) are used on the transverse vertical walls of the waveg-

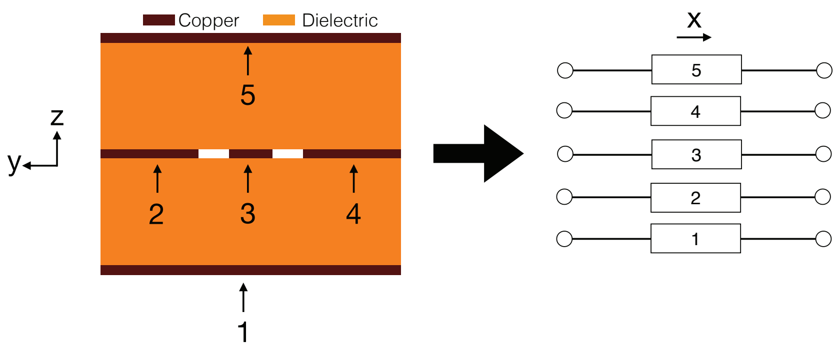

Figure 2.4: Mapping of the host S-CBCPW waveguide conductors to the equivalent-circuit model.

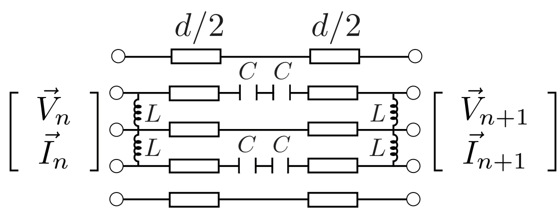

Figure 2.5: Equivalent-circuit model of the loaded S-CBCPW unit-cell.

uide in order to accomplish this. This boundary condition supports all quasi-TEM modes, including the CSL, which still has electric fields tangent to this plane, as indicated for the conductor backing in Fig. 2.2c.

The S-CBCPW possesses physical dimensions and dielectric properties as labelled in Fig. 2.3, in which propagation is assumed in the x-direction. The period of the unit cell in the direction of propagation is d, and the waveguide has width w, CPW stripline width s, CPW gaps width g, upper dielectric height h_u, and lower dielectric height h_l, metallic trace thickness t. The dielectrics possess relative permittivities of ϵ_u (the upper dielectric) and ϵ_l (lower dielectric). Both dielectrics are assumed to be non-magnetic.

2.2 Equivalent-Circuit Model

The host TL is modelled in the circuit domain using a MTL model. The mapping of the physical conductors of the S-CBCPW structure to the equivalent-circuit model is shown in Fig. 2.4. This conductor mapping will be used in the remainder of this thesis, unless stated otherwise.

As previously indicated, this waveguide is loaded in a TL-MTM fashion with series capacitors in the CPW grounds and shunt inductors in the CPW gaps, such that it supports a backward-wave CPW mode. The dispersion of this mode may then be precisely controlled by its geometric properties and loading component values. This results in the equivalent-circuit model shown in Fig. 2.5, in which the series capacitors have been inserted into the two CPW grounds (conductors 2 and 4), and shunt inductors are introduced between the CPW grounds and CPW strip line (conductor 3).

The equivalent-circuit model is analyzed by reducing it to a single network which can be described with an ABCD transmission matrix, i.e.:

$$\begin{bmatrix} \vec{V}_n \\ \vec{I}_n \end{bmatrix} = \begin{bmatrix} [A] & [B] \\ [C] & [D] \end{bmatrix} \begin{bmatrix} \vec{V}_{n+1} \\ \vec{I}_{n+1} \end{bmatrix} \tag{2.1}$$

The transmission network can in turn be described as a cascade of the transmission networks of each of its sub-components (the series capacitors, MTL sections, and shunt inductors):

$$\begin{bmatrix} [A] & [B] \\ [C] & [D] \end{bmatrix} = [T_L]\,[T_{TL}]\,[T_C]\,[T_C]\,[T_{TL}]\,[T_L] \tag{2.2}$$

each of which is an 8×8 matrix, due to the host waveguide being composed of 5 conductors. They are:

$$[T_L] = \begin{bmatrix} 1 & 0 & 0 & 0 & 0 & 0 & 0 & 0 \\ 0 & 1 & 0 & 0 & 0 & 0 & 0 & 0 \\ 0 & 0 & 1 & 0 & 0 & 0 & 0 & 0 \\ 0 & 0 & 0 & 1 & 0 & 0 & 0 & 0 \\ \frac{1}{j\omega L} & \frac{-1}{j\omega L} & 0 & 0 & 1 & 0 & 0 & 0 \\ \frac{-1}{j\omega L} & \frac{2}{j\omega L} & \frac{-1}{j\omega L} & 0 & 0 & 1 & 0 & 0 \\ 0 & \frac{-1}{j\omega L} & \frac{1}{j\omega L} & 0 & 0 & 0 & 1 & 0 \\ 0 & 0 & 0 & 0 & 0 & 0 & 0 & 1 \end{bmatrix} \tag{2.3}$$

$$[T_{TL}] = \begin{bmatrix} \cosh([\gamma]\,d/2)^T & -[Z_o]\sinh([\gamma]\,d/2) \\ -\sinh([\gamma]\,d/2)\,[Z_o]^{-1} & \cosh([\gamma]\,d/2) \end{bmatrix} \tag{2.4}$$

$$[T_C] = \begin{bmatrix} 1 & 0 & 0 & \frac{1}{j\omega C} & 0 & 0 & 0 & 0 \\ 0 & 1 & 0 & 0 & 0 & 0 & 0 & 0 \\ 0 & 0 & 1 & 0 & 0 & \frac{1}{j\omega C} & 0 & 0 \\ 0 & 0 & 0 & 1 & 0 & 0 & 0 & 0 \\ 0 & 0 & 0 & 0 & 1 & 0 & 0 & 0 \\ 0 & 0 & 0 & 0 & 0 & 1 & 0 & 0 \\ 0 & 0 & 0 & 0 & 0 & 0 & 1 & 0 \\ 0 & 0 & 0 & 0 & 0 & 0 & 0 & 1 \end{bmatrix} \tag{2.5}$$

where $[\gamma]$ and $[Z_o]$ are the 4×4 propagation constant and characteristic-impedance matrices, respectively, of the host MTL, and the conductor backing has been chosen to be the reference conductor [87]. $[\gamma]$ and $[Z_o]$ are determined from the host TL's per-unit length capacitance and inductance matrices ($[C]$ and $[L]$, respectively), using the following process.

The per-unit length capacitance and inductance matrices are converted into per-unit length admittance and impedance matrices (assuming lossless TLs) as follows:

$$\begin{aligned}[Y] &= j\omega\,[C]\\ [Z] &= j\omega\,[L]\end{aligned} \tag{2.6}$$

Then, $[Y]$ and $[Z]$ are used to extract the propagation constants and characteristic impedances of the four quasi-TEM modes supported by the host waveguide (i.e., the isolated unloaded modes), via the equations [87]:

$$\begin{aligned}[\gamma] &= ([Y]\,[Z])^{\frac{1}{2}}\\ [Z_o] &= [Z]\,[\gamma]^{-1}\end{aligned} \tag{2.7}$$

The application of (2.7) then results in a $[\gamma]$ which possesses off-diagonal entries. In order to obtain the propagation constants of each quasi-TEM mode, the matrix $[\gamma]$ can be *diagonalized* [88]. This process converts the propagation constants from the *terminal* (or *line*) domain to the *modal* domain [87], and is defined by:

$$[\gamma_M] = [T]\,[\gamma]\,[T]^{-1} \tag{2.8}$$

where $[T]$ is known as the *diagonalization* matrix. $[\gamma_M]$ is then the diagonalized matrix corresponding to the propagation constant of each quasi-TEM mode. Both $[\gamma_M]$ and $[T]$ can be determined simultaneously with a numerical tool such as an eigenmode solver. The hyperbolic trigonometric terms in (2.4) can then be defined as [87]:

$$\begin{aligned}\cosh([\gamma]\,d) &= \frac{1}{2}\,[T]\left(e^{[\gamma_M]d} + e^{-[\gamma_M]d}\right)[T]^{-1}\\ \sinh([\gamma]\,d) &= \frac{1}{2}\,[T]\left(e^{[\gamma_M]d} - e^{-[\gamma_M]d}\right)[T]^{-1}\end{aligned} \tag{2.9}$$

The matrix $[C]$ can be determined through an electrostatic computation, either analytically for simple cases such as the shielded Sievenpiper mushroom structure [52], or numerically with the use of processes such as those described in [87], for example, a finite-element-method solver. Importantly, the PMC transverse boundary conditions must be assumed in this process in order to derive the correct properties. Once $[C]$ is known, $[L]$ can easily be determined via simulating the host structure in a vacuum and by applying the equation [89]:

$$[L] = \epsilon_0\mu_0\,[C_{\epsilon=\epsilon_0}]^{-1} \tag{2.10}$$

At this point, (2.3) through (2.5) can be inserted into (2.2) to solve for the overall transmission matrix of the unit cell. Once the ABCD transmission matrix is known, Bloch's theorem (1.1) can be used to define the Bloch modes of the unit cell in terms of its transmission properties by inserting it into (2.1):

$$\begin{bmatrix}\vec{V}_n\\ \vec{I}_n\end{bmatrix} = \begin{bmatrix}[A] & [B]\\ [C] & [D]\end{bmatrix}\begin{bmatrix}\vec{V}_n\\ \vec{I}_n\end{bmatrix}e^{-\gamma_B d} \tag{2.11}$$

in which γ_B are the Bloch propagation constants. Equation (2.11) can then be phrased in the characteristic form of an eigenmode equation:

$$\det\left(\begin{bmatrix} [A] & [B] \\ [C] & [D] \end{bmatrix} - [I]\,e^{-\gamma_B d}\right) = 0 \tag{2.12}$$

Invoking the properties of block matrices [90] allows the simplification of this determinant prior to solving it. Specifically, the determinant can be simplified to:

$$\begin{gathered}\det\begin{bmatrix} [A] - [I]\,e^{-\gamma_B d} & [B] \\ [C] & [D] - [I]\,e^{-\gamma_B d} \end{bmatrix} \\ = \\ \det\left([D] - [I]\,e^{-\gamma_B d}\right)\det\left(\left([A] - [I]\,e^{-\gamma_B d}\right) - [B]\left([D] - [I]\,e^{-\gamma_B d}\right)^{-1}[C]\right)\end{gathered} \tag{2.13}$$

However, the properties of matrix determinants allow the following equivalence, for a general matrix $[X]$:

$$\det([X]) = \det\left([X]^T\right) \tag{2.14}$$

such that (2.13) can be written with (2.12) as:

$$\det\left(\left([D] - [I]\,e^{-\gamma_B d}\right)^T\right)\det\left(\left([A] - [I]\,e^{-\gamma_B d}\right) - [B]\left([D] - [I]\,e^{-\gamma_B d}\right)^{-1}[C]\right) = 0 \tag{2.15}$$

Furthermore, since

$$\det([X])\det([Y]) = \det([X]\,[Y]) \tag{2.16}$$

Equation (2.15) expands to:

$$\det\left(\left([D] - [I]\,e^{-\gamma_B d}\right)^T\left([A] - [I]\,e^{-\gamma_B d}\right) - \left([D] - [I]\,e^{-\gamma_B d}\right)^T[B]\left([D] - [I]\,e^{-\gamma_B d}\right)^{-1}[C]\right) = 0 \tag{2.17}$$

Additionally, the properties of symmetric, reciprocal networks [91] specify some useful relations:

$$\begin{gathered}[A] = [D]^T \\ [B]^T[D] = [D]^T[B] \\ [D]^T[A] - [B]^T[C] = [I]\end{gathered} \tag{2.18}$$

Then, (2.15) can be written as

$$\det\left(\left([D] - [I]\,e^{-\gamma_B d}\right)^T\left([A] - [I]\,e^{-\gamma_B d}\right) - [B]^T\left([D] - [I]\,e^{-\gamma_B d}\right)\left([D] - [I]\,e^{-\gamma_B d}\right)^{-1}[C]\right) = 0 \tag{2.19}$$

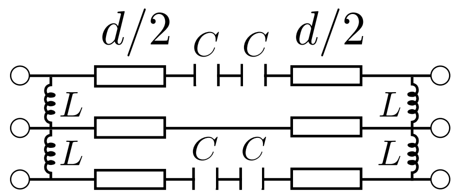

Figure 2.6: Equivalent-circuit model of the S-CBCPW unit cell, examining the isolated CPW and CSL modes.

which then reduces to:

$$\det\left([D]^T[A]-\left([D]^T+[A]\right)e^{-\gamma_B d}+[I]\,e^{-2\gamma_B d}-[B]^T[C]\right)=0 \tag{2.20}$$

After employing the unused relations from (2.18) and dividing through by $e^{-\gamma_B d}$, this yields:

$$\det\left([A]-[I]\cosh\left(\gamma_B d\right)\right)=0 \tag{2.21}$$

Equation (2.21) is the solution to the Bloch modes supported by the loaded S-CBCPW structure. The expanded expression of the determinant yields a quartic equation, which would be extremely difficult to solve, and therefore a complete analytic expression was not obtained as part of this work.

Importantly, the Bloch modes solved include their coupling effects. The isolated modes can also be solved for by removing the extraneous conductors from the above process. Figure 2.6 shows the equivalent-circuit model of the loaded S-CBCPW unit cell – similar to the previous unit cell, but in which the shield and conductor backing have been removed. In order to compute the dispersive properties of the Bloch modes, the center (CPW strip line) conductor is taken to be the reference, and the associated transmission matrices of each unit-cell component become:

$$\begin{gathered}
[T_L]=\begin{bmatrix} 1 & 0 & 0 & 0 \\ 0 & 1 & 0 & 0 \\ \frac{1}{j\omega L} & 0 & 1 & 0 \\ 0 & \frac{1}{j\omega L} & 0 & 1 \end{bmatrix} \\
[T_{TL}]=\begin{bmatrix} \cosh([\gamma]\,d/2)^T & -[Z_o]\sinh([\gamma]\,d/2) \\ -\sinh([\gamma]\,d/2)\,[Z_o]^{-1} & \cosh([\gamma]\,d/2) \end{bmatrix} \\
[T_C]=\begin{bmatrix} 1 & 0 & \frac{1}{j\omega C} & 0 \\ 0 & 1 & 0 & \frac{1}{j\omega C} \\ 0 & 0 & 1 & 0 \\ 0 & 0 & 0 & 1 \end{bmatrix}
\end{gathered} \tag{2.22}$$

The transmission matrix $[T_{TL}]$ is the same as it was previously; however, its matrices $[\gamma]$ and $[Z_o]$ have changed. Specifically, the rows and columns of $[C]$ and $[L]$ corresponding to the removed conductors in the equivalent-circuit model have also been removed, reducing the rank of the resulting $[\gamma]$ and $[Z_o]$ matrices.

An example of this modelling is shown in Figs. 2.7a and 2.7b, in which the attenuation constants and the CSL mode have been removed for clarity. Fig. 2.7a shows the isolated lower PPW and CPW modes, as well as the new mode and bandgap formed as a result of their coupling. This coupled mode is then plotted along with the isolated upper PPW mode, and the new mode and second bandgap formed as a result of their coupling in Fig. 2.7b.

The properties of the host S-CBCPW (designed for relatively small coupling levels) are $d = 10mm$, $w = 10mm$, $s = 1mm$, $g = 1mm$, $h_l = 40mm$, $h_u = 40mm$, $\epsilon_l = 10.2$, $\epsilon_u = 1.0$, and $t = 35\mu m$. A finite-element-method (FEM) electrostatic simulation of this structure yields the following capacitance and inductance matrices:

$$[C] = \begin{bmatrix} 95 & -60 & -34 & -0.9 \\ -60 & 120 & -60 & -0.4 \\ -34 & -60 & 95 & -0.9 \\ -0.9 & -0.4 & -0.9 & 2.2 \end{bmatrix} pF/m \qquad [L] = \begin{bmatrix} 5.24 & 4.93 & 4.80 & 5.00 \\ 4.93 & 5.31 & 4.93 & 5.00 \\ 4.80 & 4.93 & 5.24 & 5.00 \\ 5.00 & 5.00 & 5.00 & 10.0 \end{bmatrix} \mu H/m \tag{2.23}$$

Loading components of value $L = 10nH$ and $C = 2pF$ were used. The isolated CPW mode was obtained by using the three-conductor model of Fig. 2.6, whereas the coupled system was obtained by using a four-conductor model in which conductor backing of the S-CBCPW was considered, but the shield was not. The capacitance and inductance matrices are simply modified by removing the corresponding row and column from each. The coupled S-CBCPW system was then obtained using the five-conductor model of Fig. 2.5. The isolated lower and upper PPW modes were obtained simply by modelling a plane wave in a medium with the corresponding dielectric constants ϵ_l and ϵ_u, which was found to be a very good approximation.

As shown in Figs. 2.7a and 2.7b, there is a moderate amount of coupling between all modes, resulting in the formation of bandgaps where the isolated mode dispersions intersect. Critically, it becomes apparent that the bandgap phenomenon is due to modal coupling – specifically, only due to the interaction of any given two (in this case) isolated modes. The isolated forward lower PPW mode couples with the isolated backward CPW mode to form the lower-frequency bandgap, while the relatively isolated backward CPW mode couples with the isolated forward upper PPW mode to form the higher-frequency bandgap. In the completely coupled case (the "Coupled S-CBCPW" mode), the bandgap between 1.35 GHz and 1.55 GHz is formed by both the CPW and lower PPW modes, but does not largely affect the upper PPW mode, while the bandgap between 1.61 GHz and 1.78 GHz is formed by both the CPW and upper PPW modes, but does not greatly affect the lower PPW mode. Therefore, it is expected that if the CPW mode were to be excited in this periodic medium, it should experience suppression in *both* the ranges of 1.35 GHz to 1.55 GHz, and 1.61 GHz to 1.78 GHz, whereas the lower PPW mode would only

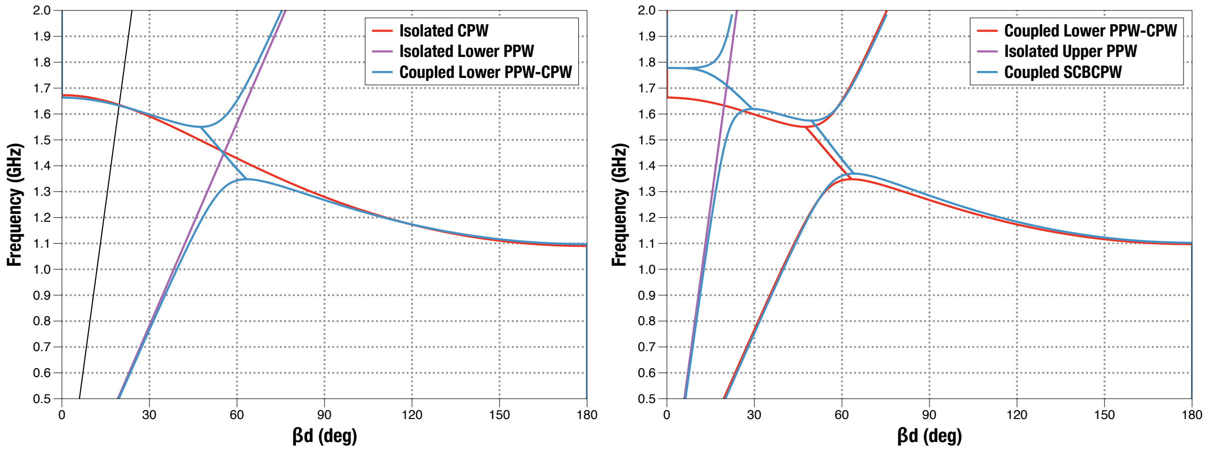

(a) (b)

Figure 2.7: Example computation of isolated and coupled modes in the loaded S-CBCPW unit cell: a) isolated and coupled CPW and Lower PPW modes, b) isolated and coupled CPW-Lower PPW and Upper PPW modes. Attenuation constants and CSL mode omitted for clarity.

experience suppression between 1.35 GHz and 1.55 GHz, and the upper PPW mode would only experience suppression between 1.61 GHz and 1.78 GHz.

2.3 Equivalent-Circuit Interpretation of Key Dispersive Properties

In order to aid in the understanding and design of such unit cells, the fields at some of the key frequencies were investigated and related to the equivalent-circuit model. Fig. 2.8 shows a relatively complex example dispersion diagram, which exhibits many distinct behaviors. The unit cell being modelled was designed to be heavily asymmetric in the vertical direction, as to examine the effects of lower and upper PPW modes with different properties. The host S-CBCPW has properties $d = 5mm$, $w = 10mm$, $s = 0.2mm$, $g = 0.5mm$, $h_l = 1.524mm$, $h_u = 100mm$, $\epsilon_l = 3.66$, $\epsilon_u = 1.0$, and $t = 35\mu m$. Loading components of value $L = 1.6nH$ and $C = 0.8pF$ are used.

The key frequencies are labelled e_1 through e_4 for the even modes and o_1 through o_3 for the odd modes. In order to understand the nature of these behaviors, the currents in the equivalent-circuit model are investigated at each point. Figures 2.9a through 2.10c display these quantities, for which the red lines indicate current flow (at a time-phase angle of 0^o, corresponding to t = 0s). Propagation is defined from left to right (the positive x direction). These results were obtained by observing the fields produced by the numerical eigenmode simulations, and are therefore approximations. However, there is much insight to be gained about the operation of this structure from these equivalent-circuit models.

Between these points lie several distinct frequency ranges, which are characterized by unique modal behaviors. Below e_1, only the PPW mode propagates, but it becomes very dispersive as it couples with

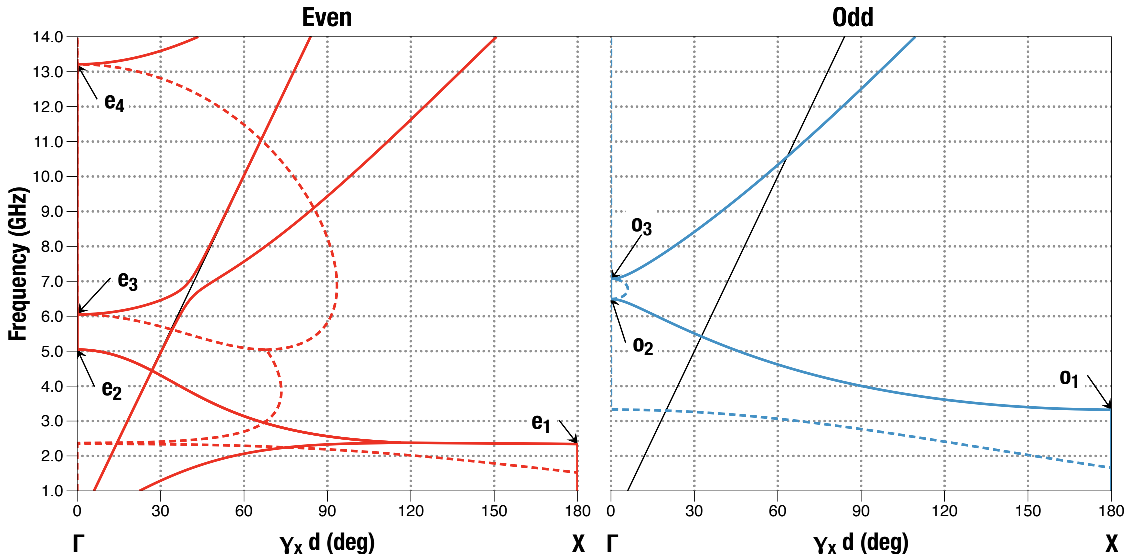

Figure 2.8: Example complex dispersion diagram with labelled frequencies of interest.

the CPW mode around e_1. The range between e_1 and e_2 is a complex-mode band, in which both real and imaginary (propagating and attenuating) components exist simultaneously. The range between e_2 and e_3 is one in which both the PPW and CPW modes are cut off. Above e_3, the forward PPW mode propagates, and above e_4, the forward CPW mode propagates.

Point e_1 (corresponding to the equivalent circuit of Fig. 2.9a) is the X-point and Bragg frequency of the CPW mode. Currents at this point incur 180^o of phase, such that there is no net current flow between unit cells (a standing wave caused by Bragg reflection). As indicated, the boundaries on the outer edges of the unit cell can be described as open circuits. Both the capacitors and the inductors are in the main conducting paths of the currents, such that they both contribute to determining the frequency of this point. This frequency is lower than it would be in the isolated case due to coupling with the lower PPW mode (specifically, the conductor backing).

Point e_2 (corresponding to the equivalent circuit of Fig. 2.9b) corresponds to a Γ-point, such that there is no propagation. At this point, the net current on the conductor backing becomes non-zero (it has net zero current in the complex-mode region), which cuts off the complex mode due to the fact that the PPW mode dominates over the CPW. The frequency of this point is controlled by the coupling of the CPW and PPW modes, which can be controlled through the width of the CPW grounds or the dielectric height.

The point e_3 (corresponding to the equivalent circuit of Fig. 2.9c) is the point at which propagation of the PPW mode is restored. The currents bypass the inductors and instead flow to the adjacent unit cell, corresponding to short-circuit conditions on the outer terminals of the unit cells. Since there is no current flow through the inductors, the loading capacitors at this point are in resonance with the per-unit-length series inductance of the CPW conductors, such that they primarily control this frequency.

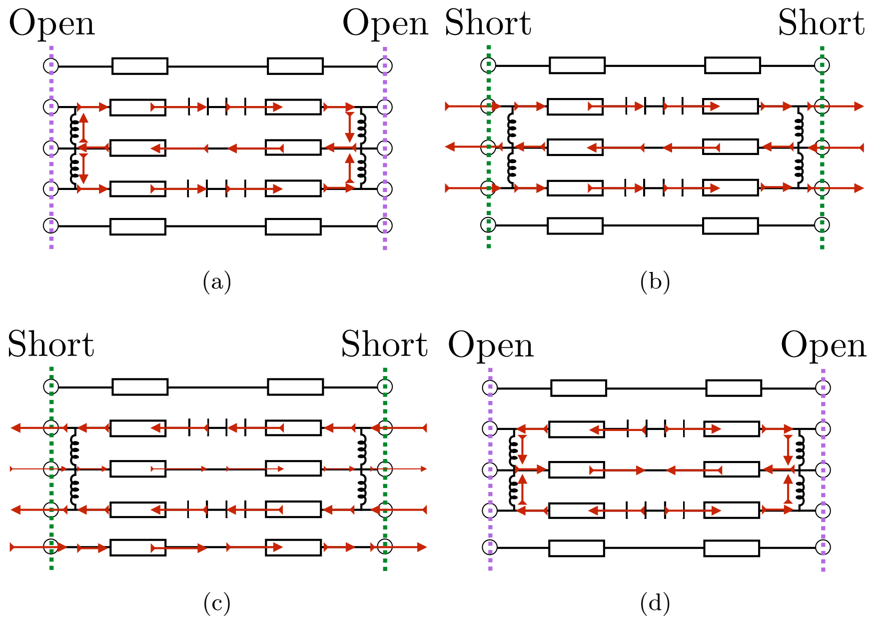

Figure 2.9: Equivalent-circuit model with overlaid currents (red, at t = 0s), sized to convey magnitude, corresponding to points: a) e_1, b) e_2, c) e_3, d) e_4

The currents in the CPW strip line are contradirected to those on the CPW grounds, indicating that the properties of the CPW mode still have an influence on this frequency; however, these currents are relatively weak, indicating the dominance of the PPW mode.

The point e_4 (corresponding to the equivalent circuit of Fig. 2.9d), corresponds to the Γ-point of the forward-propagating region of the CPW mode. There is no current flow between unit cells, corresponding to open-circuit conditions. Since there is no net current flow through the capacitors, the loading inductors at this point are in resonance with the shunt capacitance of the transmission-line segments. Interestingly, there is no longitudinal current flow on the conductor backing – further confirming that this is a CPW mode. The high frequency of this point is attributed to capacitive coupling of the CPW TL segments with the conductor backing, which reduces the shunt capacitance of the CPW gaps (a similar effect to that reported in [47]).

The point o_1 (corresponding to the equivalent circuit of Fig. 2.10a) is the CSL equivalent of e_3, which is the X-point of the CPW mode. There is no current flow through the boundaries, which again corresponds to open circuits. There is also no net current flow through the center conductor, which in the field domain supports oppositely directed currents on either side of the conductor. Again, this point is primarily controlled by both the loading capacitors and inductors.

Point o_2 (corresponding to the equivalent circuit of Fig. 2.10b) is the Γ-point of the backward propagating region of the CSL mode. The current does not flow between unit cells due to the effective open

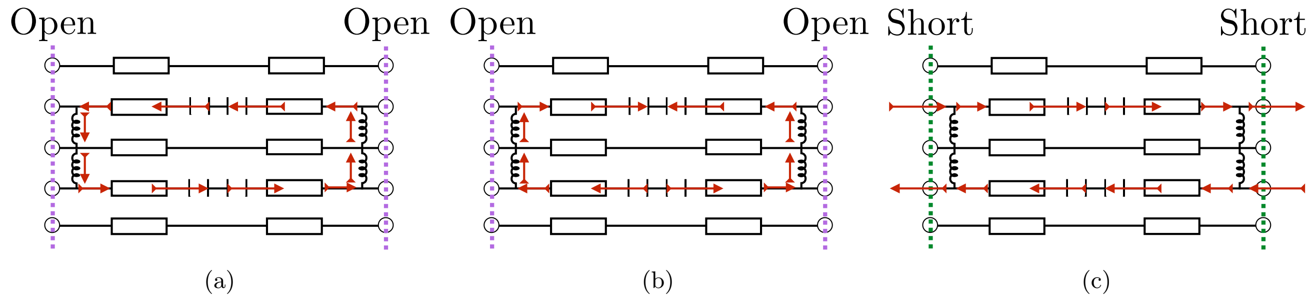

Figure 2.10: Equivalent-circuit model with overlaid currents (red, at t = 0s), sized to convey magnitude, corresponding to points: a) o_1, b) o_2, c) o_3

circuits on the ports, and as such all of the currents pass through the loading inductors. The currents form loops passing through the inductors and TL sections, and it is implied that the currents pass through the CPW gaps (not shown) to complete the loops. Therefore, no currents pass through the capacitors, and the frequency of this point is controlled primarily by the loading inductance.

The point o_3 (corresponding to the equivalent circuit of Fig. 2.10c) corresponds to the CSL Γ-point similar to e_4 for the CPW mode. All of the current flow is between unit cells, corresponding to a short-circuit at the terminals. Since there is no current flow through the inductors, the loading capacitors at this point are in resonance with the shunt inductance of the transmission-line segments, and are primarily responsible for controlling the frequency of this point.

2.4 Parametric Sweeps

A parametric sweep was conducted on several of the unit cell's variables in order to determine the validity of the the claims made by the equivalent-circuit model. Specifically, the first three even points were observed for changes to the unit cell parameters L, and C, g, s, w. The base case was taken to be the previously investigated unit cell, although for simplicity the upper PPW and CSL modes, as well as the real (attenuating) component of the propagation constant were not included in the analysis.

Each variable was incremented twice in small steps, so as to gauge the effect of the variable on the dispersion. The results are plotted as dispersion diagrams in Figs. 2.11a through 2.11e. The effects on key frequencies are also summarized in Table 2.1, which describes the trends of these frequency points, and from which some basic properties may be inferred. Specifically, increasing the loading inductance L shifts e_1 downwards. The upper limit of the complex-mode coupling region (e_2) is increased, and the Γ-point where the PPW propagation is restored (e_3) is unaffected, resulting in an increase in the width of the bandgap. This behavior suggests that L determines the strength of the even-mode coupling. Increasing the loading capacitance C and gap width g, or decreasing the strip width s, shifts the modes uniformly

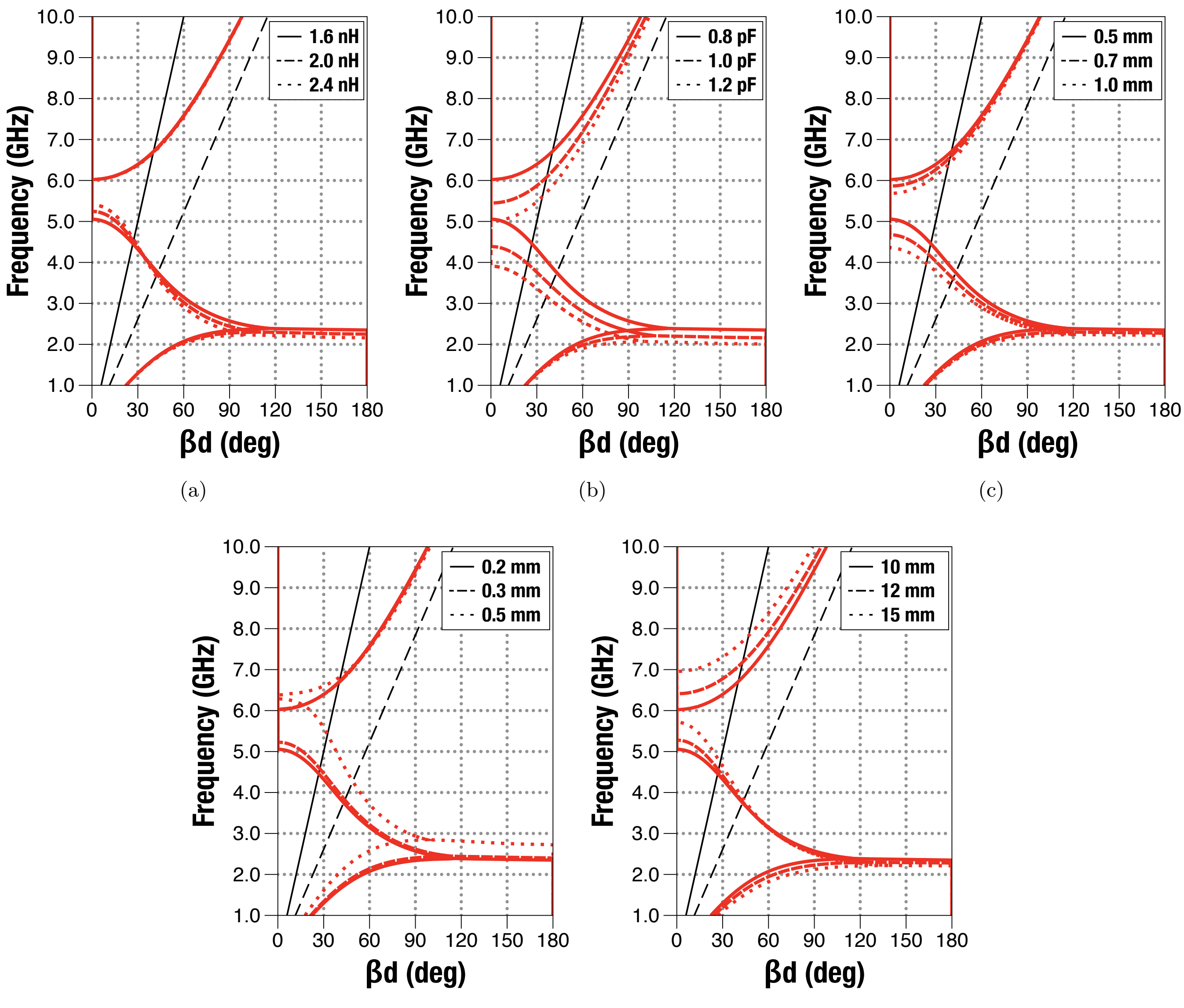

Figure 2.11: Dispersion diagrams for swept variables: a) loading inductance L, b) loading capacitance C, c) gap width g, d) strip width s, e) unit cell width w.

Table 2.1: Key frequencies and trends in the parametric study of L, C, s, g and w. Changes relative to base case indicated with arrows ↓ (decreasing trend) and ↑ (increasing trend).

[GHz]	e_1	e_2	e_3
Base case	2.36	5.06	6.02
L = 1.0 nH	2.25 ↓	5.25 ↑	6.02
L = 1.2 nH	2.16 ↓	5.41 ↑	6.02
C = 1.0 pF	2.16 ↓	4.39 ↓	5.44 ↓
C = 1.2 pF	2.00 ↓	3.91 ↓	5.01 ↓
g = 0.7 mm	2.27 ↓	4.68 ↓	5.86 ↓
g = 1.0 mm	2.22 ↓	4.36 ↓	5.68 ↓
s = 0.3 mm	2.40 ↑	5.23 ↑	6.03 ↑
s = 0.5 mm	2.72 ↑	6.29 ↑	6.39 ↑
w = 12 mm	2.28 ↓	5.29 ↑	6.40 ↑
w = 15 mm	2.21 ↓	5.72 ↑	6.95 ↑

downward in frequency. Thus, the above four parameters may be used to control the lower edge of the bandgap, which can be used to further miniaturize the unit cell. This behavior is also evident in the isolated modes, for which it was found that C, g, and s each influence both the Γ- and X-points of the CPW mode. Lastly, increasing the cell width w decreases e_1, which forms the lower edge of the bandgap, while simultaneously increasing e_3, which forms the upper edge of the bandgap. This indicates that the unit cell width also enhances the coupling between the even modes, since the bandgap expands to both lower and higher frequencies. Although e_3 is not controlled by the value of L in this case, it should be noted that this frequency corresponds to the Γ-point of the isolated CPW backward mode, which can be controlled be either L or C, depending on its design (as described in [85]).

The understanding of these parameters proves helpful in the design of miniaturized EBGs meeting desired specifications on operating frequency, bandgap width, and even suppression level. Notably, for the desired bandgap, the electrical size of the unit cell ranges from $\lambda_g/13$ to $\lambda_g/5$, where λ_g is the wavelength in the dielectric. This demonstrates the strong degrees of miniaturization possible with the TL-MTM approach.

2.5 Finite Element Method Full-Wave Simulations

The dispersive properties of the unit cells examined with the equivalent-circuit model previously introduced can be further validated with the use of FEM simulations. Ansys HFSS [92] was used to simulate both the dispersive properties of the unit cells with its eigenmode simulator, and the multi-modal scattering parameters with its driven modal simulator, as has been done previously in the literature [93].

The unit cell used has the properties $d = 10mm$, $w = 10mm$, $s = 0.5mm$, $g = 0.5mm$, $h_l = 1.524mm$, $h_u = 100mm$, $\epsilon_l = 4.4$, $\epsilon_u = 1.0$, and $t = 35\mu m$. $L = 10nH$ and $C = 5pF$. These values were chosen in order to demonstrate a miniaturized unit cell, and to demonstrate the result of large LC loading values on

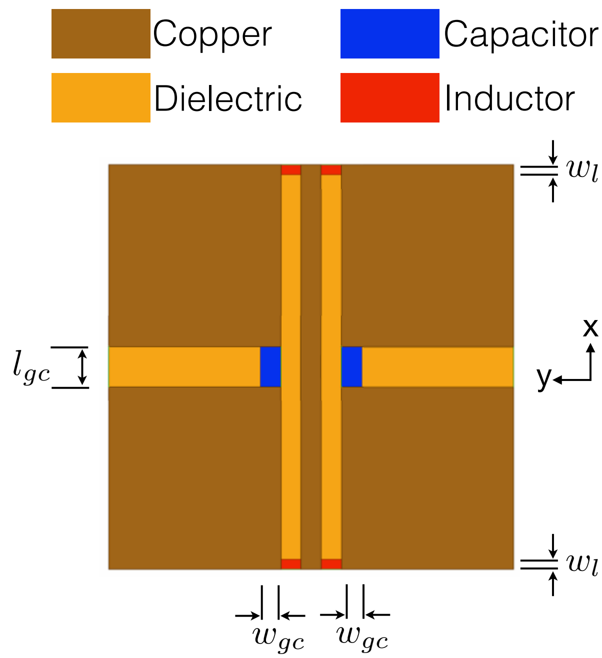

Figure 2.12: Layout of simulation unit cell in HFSS. Image shows middle CPW layer as viewed from the top.

the level of SW suppression. This is modelled by inserting lumped inductive and capacitive components into the host TL, as indicated in Fig. 2.12, which shows the middle CPW layer as viewed from the top. Additional parameters are needed to model this unit cell in two dimensions: $l_{gc} = 0.5mm$ is the length of the slit cut into the CPW grounds in order to insert a loading capacitor element without shorting it out. The width of this loading capacitor is $w_{gc} = 0.5mm$. The width of the loading inductors are $w_l = 0.5mm$.

2.5.1 Eigenmode Simulations

The eigenmode simulator in HFSS extracts the frequencies of Bloch modes for a given structure. In order to obtain a full dispersion diagram, master-slave periodic boundary conditions (PBCs) are applied in the direction of propagation, to which a variable angle is applied as a phase delay between the boundaries. This variable is then swept from 0 to 180 degrees in order to obtain the full diagram. Figs. 2.13a through 2.13c show the simulation setup. As previously discussed, the transverse boundaries are PMCs, and the open boundary at the top (i.e., normal to z) is approximated by using a perfectly matched layer (PML).

The results of this simulation, and the obtained Bloch modes of the equivalent-circuit model are shown in Fig. 2.14 (slightly different loading values were used between the two simulations, an issue that will be addressed shortly). Generally, the results agree well, especially around the Γ-point. Due to the large variation in modal profiles around this point, the domain from 0^o to 30^o was studied at a higher resolution than that above 30^o. The PPW mode propagates from DC to around 0.6 GHz, at which point it interacts

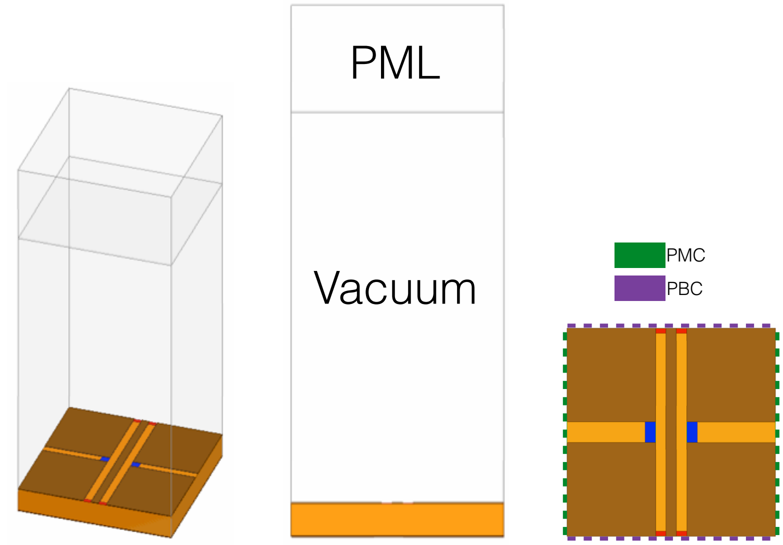

Figure 2.13: Eigenmode simulation setup of the proposed unit cell: a) isometric view, b) front view showing vacuum region and PML, c) top view showing PBC and PMC boundary conditions.

with the backward CPW mode to form a bandgap up to 1.2 GHz. Above this frequency, it propagates as a regular forward mode. The backward CPW mode propagates in a narrow bandwidth around 0.4 GHz to 0.6 GHz, at which point it also experiences the same bandgap as the PPW mode, but is not restored until around 3.5 GHz where it propagates as a forward mode. The backward CSL mode starts propagating around 0.5 GHz, has a small bandgap from 1.3 GHz to 1.7 GHz, and then propagates as a forward mode above 1.7 GHz. The upper PPW/SW mode propagates at nearly every frequency, but experiences a very weak bandgap around 1.3 GHz where it couples with the forward PPW mode.

The differences between the equivalent-circuit model and the HFSS eigenmode data are attributed the physical realization of the unit cell. For example, the loading capacitors in the two-dimensional simulation are in parallel with the capacitance afforded by the transverse gaps in which they are placed. These gaps provide a frequency-dependent capacitance which will have a small effect on results. Similarly, the loading inductors possess a physical length in the direction of propagation, which can result in current flow between the CPW strip line and grounds that is not exactly on the edges of the unit-cell, as expected by the equivalent-circuit model. Additionally, there is some inductance in the CPW conductors caused by the constraining of the currents through the inductive strips that is independent of the value of the inductance specified on the inductive surface. Unfortunately, it appears that there is no realistic method of mitigating these effects (in HFSS). For example, increasing the length of the slit for the loading capacitors (l_{gc}) may reduce the parasitic parallel capacitance, but will also cause the host waveguide to appear increasingly discontinuous at higher frequencies. Similarly, decreasing the width of the loading inductors (w_l) may help to have the inductor appear to be operating at a single point in space, but will also constrain the currents further such that additional net inductance will be experienced by the Bloch modes.

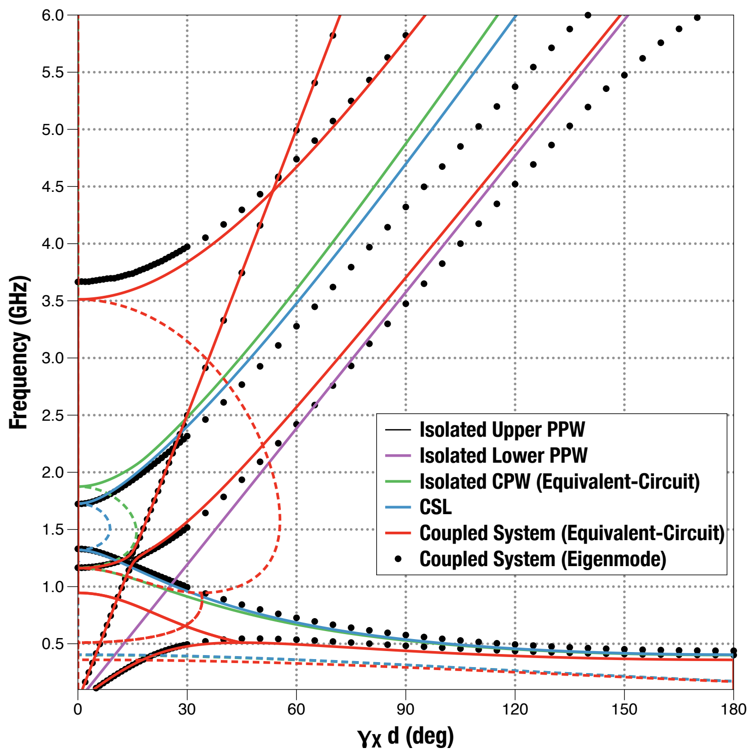

Figure 2.14: Equivalent-circuit model dispersion versus data obtained for an HFSS eigenmode simulation.

The values of the loading elements in the equivalent-circuit model have therefore been slightly adjusted to accommodate these physical discontinuities of the two dimensional host waveguide. These differences become increasingly noticeable near the Γ-point, where *all* of the current passes through either the series capacitors or the shunt inductors. In order to offset these differences, a loading capacitor value of 6pF was used in the equivalent-circuit model (up from 5pF in the HFSS model), and a loading inductor value of 11nH was used in the equivalent-circuit model (up from 10nH in the HFSS model).

There is a also a noticeable divergence at higher frequencies and phase angles. This is also attributed to the physical discontinuities of the waveguide used for the insertion of the loading components. Due to these discontinuities, the onset of the Bragg stopbands occurs at a lower frequency than they would for a continuous waveguide. This effect results in additional phase shifts as the modes approach the X-point. The slight difference between the equivalent-circuit model and the eigenmode solution at the Γ-points is attributed to the frequency-dependent nature of the parasitic reactance caused by these discontinuities.

2.5.2 Transmission Simulations

To further validate the dispersive nature of this periodic structure, and to examine the behavior of each isolated mode, the multi-modal scattering parameters were simulated using a driven modal setup that will be referred to as a *transmission* simulation. In a transmission simulation, an unloaded waveguide with the same properties as the unit cell's host medium is used to guide the quasi-TEM modes in and out of a finite cascade of unit cells – one unloaded waveguide on each end of the EBG. Modes are excited and terminated (with an appropriately matched impedance) via a waveport at each of the ends of these unloaded waveguides. Several other types of simulations such as the incident plane wave test, transmission-line test, and antenna transmission test have been used extensively in the EBG literature, but are not adequate for determining multi-mode scattering parameters, especially for the SW mode (see Appendix B), and therefore will not be used in this work. It is important from the perspective of the theory introduced in this work that the distribution of power into the various modes is known. Therefore, being able to examine and quantify the coupling of power between modes for various excitations is critical, and can only be examined with this type of setup.

The simulation setup is shown in Fig. 2.15. The same PMC boundary conditions are present on the transverse faces of the simulation domain, and a copper shield was used to bound the top of the domain, which supports the upper PPW mode. The two waveports cover the longitudinal ends of the simulation domain – one on each side, and each of which excites four modes on the unloaded waveguides. Nine unit cells were cascaded, and the length of the unloaded waveguide on either end of the periodic structures was 50mm.

The results of this simulation are shown in Fig. 2.16a, along with the previously obtained equivalent-circuit model dispersion data (imaginary component only) for reference, and a simplified version showing only the S11 and S21 of each mode in Fig. 2.16b. In addition to the insertion and return losses of each mode, the coupling to the other modes is indicated as well in order to gauge the effects of modal coupling as predicted by the dispersion. As expected, both the lower PPW and CPW modes experience a bandgap between 0.5 and 1.15 GHz, at which point propagation is restored to the lower PPW, while the CPW bandgap extends to around 3.6 GHz. The CSL mode is cut off below 0.4 GHz, and additionally experiences cutoff between 1.3 and 1.7 GHz. The upper PPW mode propagates everywhere, but is disturbed slightly around 1.25 GHz where it couples with the lower PPW mode. The lower PPW and CPW modes couple well in the complex-mode bandgap, in which approximately 10% of the (Lower PPW, CPW) reflected power is in the (CPW, Lower PPW) mode. As expected, the CSL mode does not couple well with any others. The upper PPW mode couples slightly with the lower PPW mode around 1.25 GHz (traditional SW characterization methods will not be used for reasons discussed in Appendix B). These results agree well with the predicted dispersion. The slight increase of rejection at higher frequencies for the lower PPW and CPW modes is attributed to the early onset of the Bragg stopbands as observed in the dispersion simulation.

As detailed in Fig. 2.16a, the responses of the system to excited upper and lower PPW modes confirm the nature of modal power transmission within the EBG. When a lower PPW mode is excited (corresponding to the second column) below 0.3 GHz, the majority of the power is transmitted through in the same mode, with a small portion coupling to the CPW mode in both directions. Some minor

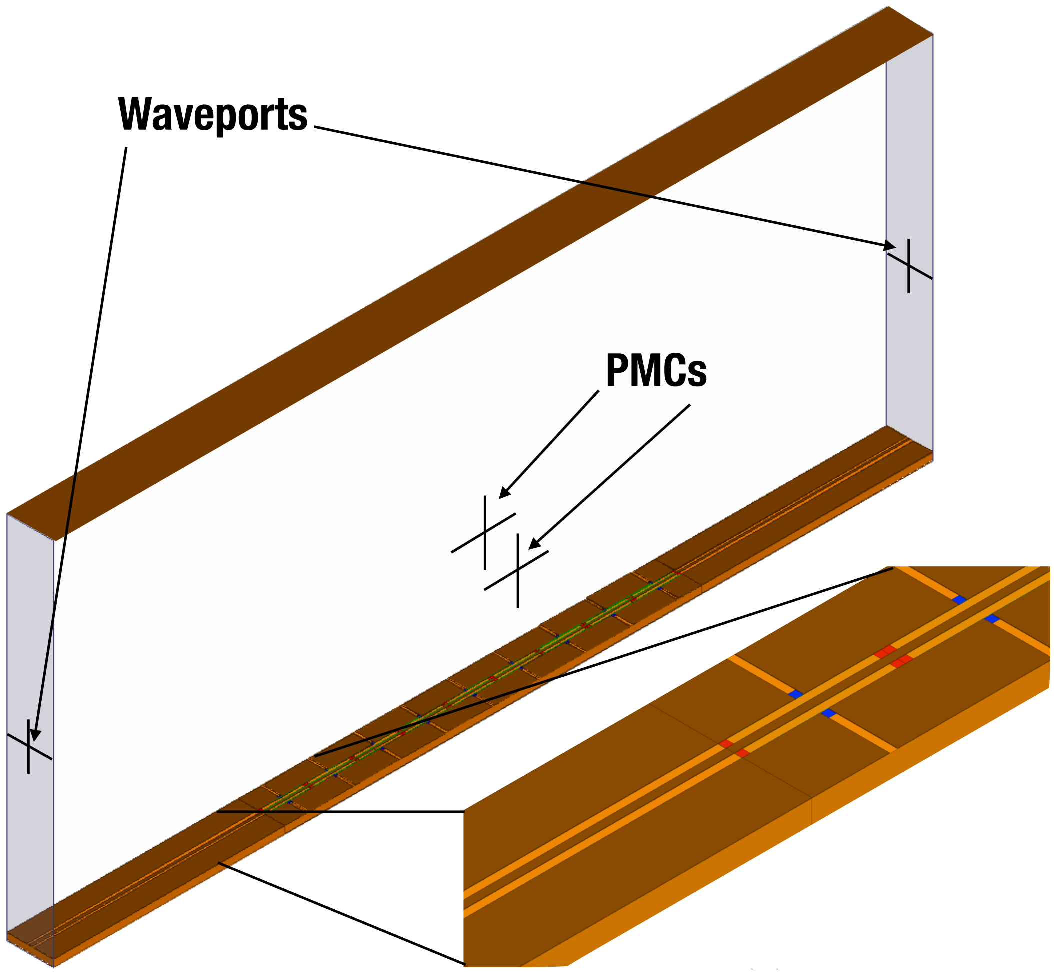

Figure 2.15: Transmission simulation setup of nine unit cells with unloaded feed waveguides.

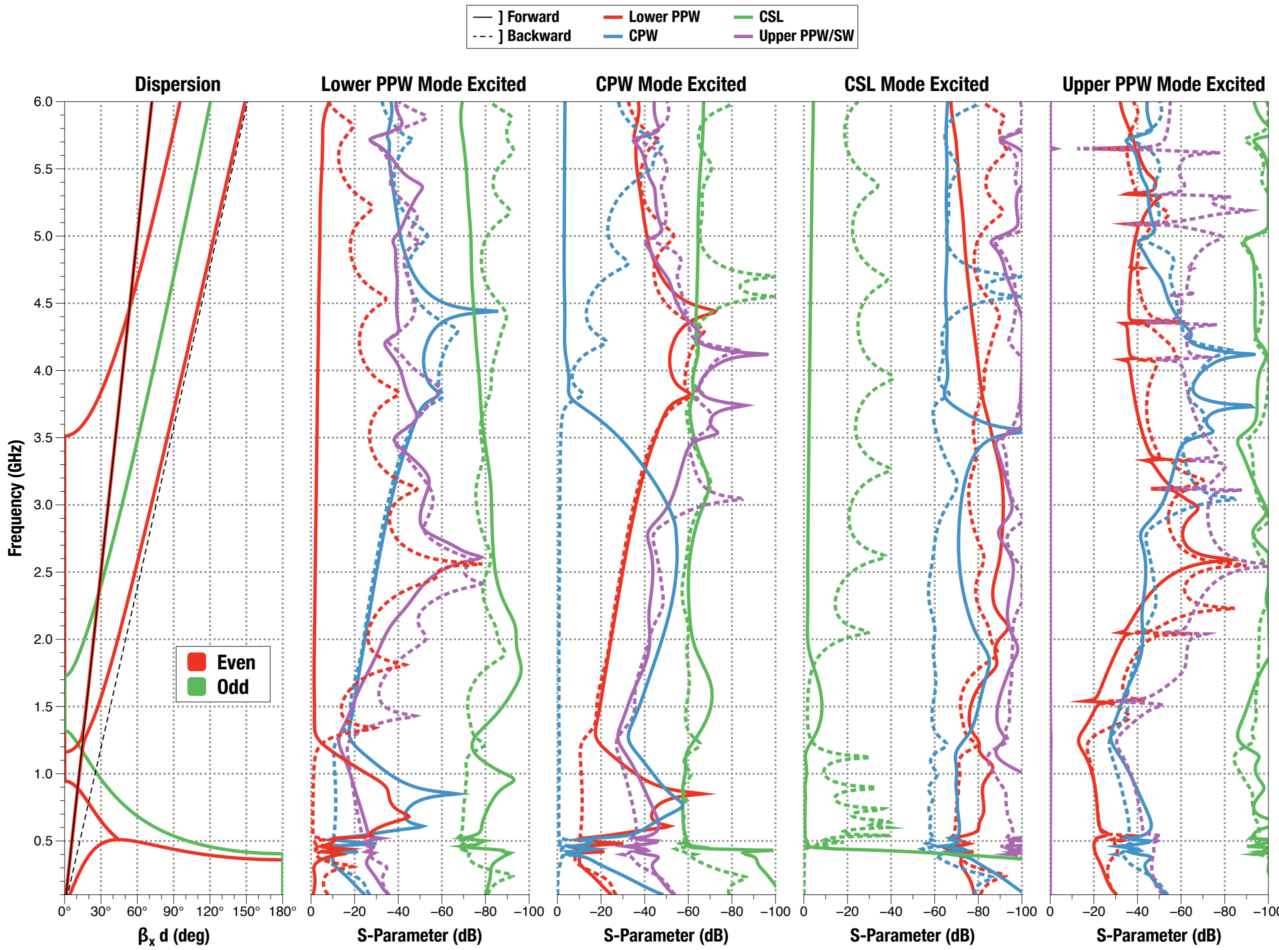

(a)

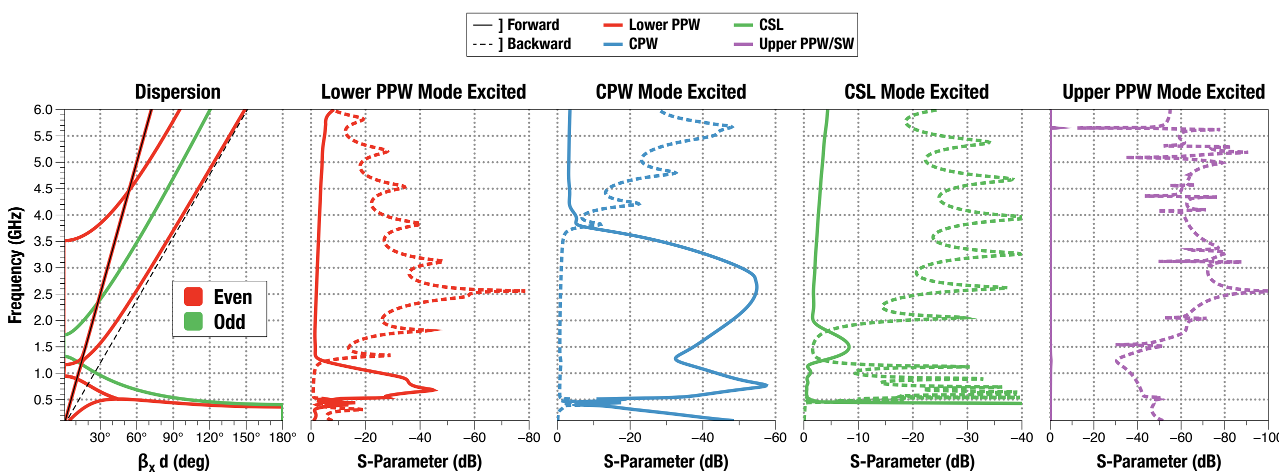

(b)

Figure 2.16: Equivalent-circuit model dispersion data (imaginary component only shown) along with simulated HFSS transmission data. Each transmission column represents the case of a single excited mode, while the colors of the curves in each column represent the magnitude of the scattering parameters for a given mode. Solid lines indicate the forward response (the power received on the opposite side of the unit cells from the excitation port), while dashed lines indicate the backward response (the power received on the same side as the excitation port). Fig. part a) shown the complete multi-mode scattering parameters, while b) shows only the S11 and S21 of each individual mode, for clarity.

reflections in the same mode are observed, which increase in magnitude as the frequency increases to 0.5 GHz. In the lower PPW bandgap region, most of the power is reflected as a lower PPW mode, but some is coupled backwards as a CPW mode, and an even smaller amount is coupled into both the forward and backward upper PPW modes. Near 1.3 GHz, the transmission of the lower PPW mode is restored, but a small portion of the power is equally transduced into the backwards CPW and forward upper PPW mode. Transmission of the lower PPW mode is essentially undisturbed above 1.3 GHz. At no point is there much coupling with the CSL mode, as expected due to the even-odd asymmetry.

When a upper PPW mode is excited (corresponding to the fifth column) below 1.5 GHz, the majority of the power is coupled to the forward or backward lower PPW mode, with a smaller amount coupling into the CPW mode or reflecting. At 1.3 GHz, there is a maximum of coupling into the lower PPW and CPW modes, as well as reflection, as expected from the dispersion – but the magnitude of coupling is not sufficiently large as to effect noticeable suppression of the upper PPW mode. Above 1.3 GHz, there is negligible coupling to other modes. As expected, there is negligible coupling to the CSL mode, similarly due to the even-odd asymmetry.

Finally, it can be shown (see Appendix C) that the upper PPW mode is an adequate model for the SW mode under certain conditions. This allows one to observe the transmission properties of the SW mode with the high degree of accuracy afforded by the developed MTL model.

2.6 Additional Loading Elements

Since the dispersive properties of the loaded S-CBCPW structure are now well-understood, the dispersion may be further augmented by adding additional loading components in a controlled manner. Specifically, it is desired to obtain a second bandgap region to suppress the upper PPW (SW) mode for the GPS antenna application at both the L1 and L2 frequencies. The coupled PPW-CPW modes were previously shown to affect the upper PPW mode in Sec. 2.5, which can be used for the first bandgap. The second is introduced in Appendix A. By combining the two methods, it should be possible to achieve two bandgaps.

Specifically, it is desired to cut off the PPW mode at low frequencies. As previously noted, the lower PPW mode propagates at low frequencies due to the uninterrupted CPW strip line. Therefore, by capacitively loading the CPW strip line (in a series configuration) as well as the CPW grounds, the lower PPW mode can be cut off below a desired frequency.

The resulting equivalent-circuit corresponding to this configuration is shown in Fig. 2.17. C_s is the value of the capacitor in the CPW strip line, while C_g is the value of the capacitor in the CPW grounds. This addition also changes the transmission matrix in the equivalent-circuit model for the series capacitors,

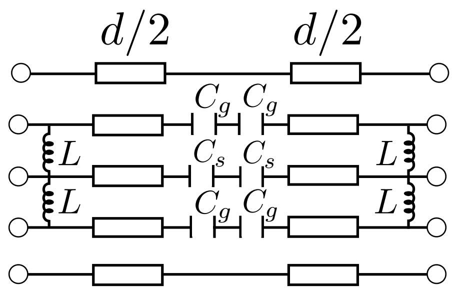

Figure 2.17: Equivalent-circuit model of a unit cell with series capacitor in the CPW strip line.

which from (2.5) becomes:

$$[T_C] = \begin{bmatrix} 1 & 0 & 0 & \frac{1}{j\omega C_g} & 0 & 0 & 0 & 0 \\ 0 & 1 & 0 & 0 & \frac{1}{j\omega C_s} & 0 & 0 & 0 \\ 0 & 0 & 1 & 0 & 0 & \frac{1}{j\omega C_g} & 0 & 0 \\ 0 & 0 & 0 & 1 & 0 & 0 & 0 & 0 \\ 0 & 0 & 0 & 0 & 1 & 0 & 0 & 0 \\ 0 & 0 & 0 & 0 & 0 & 1 & 0 & 0 \\ 0 & 0 & 0 & 0 & 0 & 0 & 1 & 0 \\ 0 & 0 & 0 & 0 & 0 & 0 & 0 & 1 \end{bmatrix} \tag{2.24}$$

Using this model by inserting a 1pF capacitor into the CPW strip line of the unit cell used in Sec. 2.3 results in the dispersion shown in Fig. 2.18, which is compared to the original case (given by C_s large). There is a small, but sufficient bandgap introduced at approximately 3.8 GHz in the upper PPW mode at approximately 20^o. The lower PPW mode is cutoff below 3.5 GHz, as desired. The series loading capacitance of the CPW mode is decreased, resulting in an overall higher frequency range for this mode. Notably, the CSL mode is not affected, as it does not have any net current on the CPW strip line.

2.7 Extension to Two Dimensions

The previous work assumes that the EBG only operates in one dimension, however, the applications suggested previously both operate in at least a two-dimensional (2D) environment. Therefore, a simple transformation from one dimension to two is sought. A full two-dimensional solution is outside of the scope of this work, but a solution can be obtained which keeps the simple one-dimensional properties of the unit cell.

Returning to the applications, it can be seen that the goal to achieve in this work is to prevent ei-

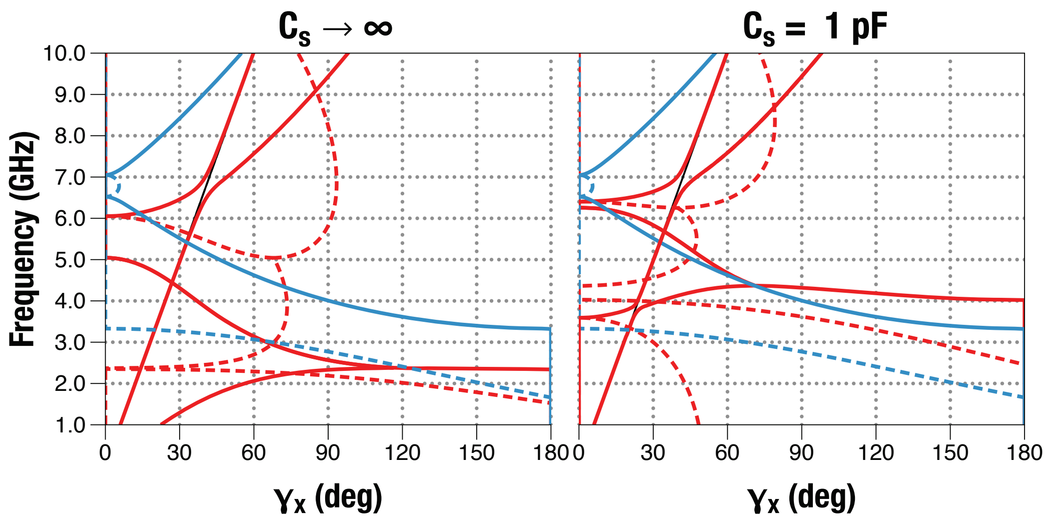

Figure 2.18: Dispersion of the a unit cell with and without CPW strip line capacitor.

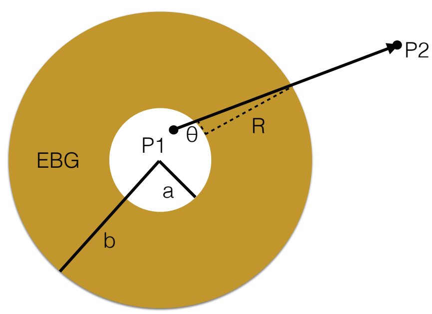

Figure 2.19: Example circular layout indicating the any propagation through the EBG can be decomposed into R and θ components.

ther the PPW or SW modes from reaching a certain point, or reciprocally, from propagating away from a point. In a 2D environment, a point can be contained within a circle, such that any ray traced from a point inside the circle must pass through the circle radius R, as indicated in Fig. 2.19. If the geometry is specified such that the angular component θ is much smaller than R, then an EBG which acts along R is sufficient. Critically, this is only a one-dimensional EBG – such that the previous designs only need a slight modification in order to be arranged into a circle.

This can be achieved by slightly deforming a cascade of one-dimensional unit cells from a rectangle (in the 2D domain), an example of which is shown in Fig. 2.20a, into a trapezoid, an example of which is shown in Fig. 2.20b. While this distortion of each unit cell is achieved by only adjusting the width w of each unit cell, it has been found that for small angles, the trapezoidal cascade of unit cells can be approximated as

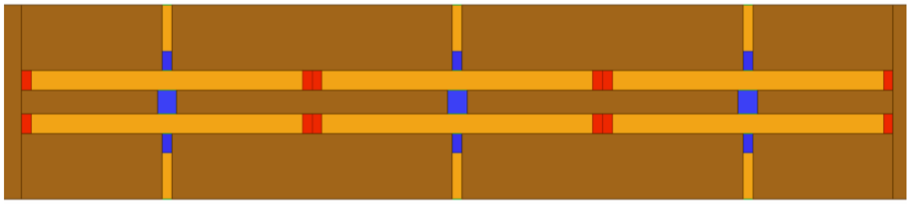

(a)

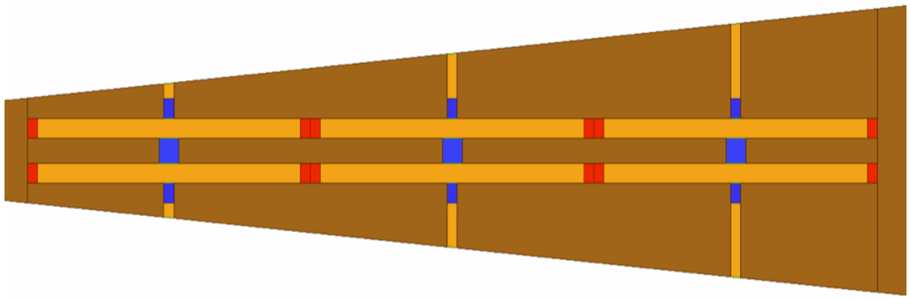

(b)

Figure 2.20: Configurations of cascaded unit cells showing the middle CPW layer as viewed from above, propagation in the horizontal direction, for a) rectangular unit cells, b) trapezoidal unit cells.

a rectangular cascade with an effective width w_a, which is the average width of the unit cells. Therefore, the dispersive properties determined for a unit cell of width w_a still holds for the trapezoidal arrangement, and the circular EBG still works well for suppression along R. This type of EBG arrangement has been previously investigated, [94–96], and was shown to be able to produce bandgaps in two dimensions.

Finally, the trapezoidal unit cells can be arranged in a circle, giving rise to the circular EBG, as shown in Fig. 2.21. This configuration will be used in the following sections for the suppression of the upper PPW and SW modes.

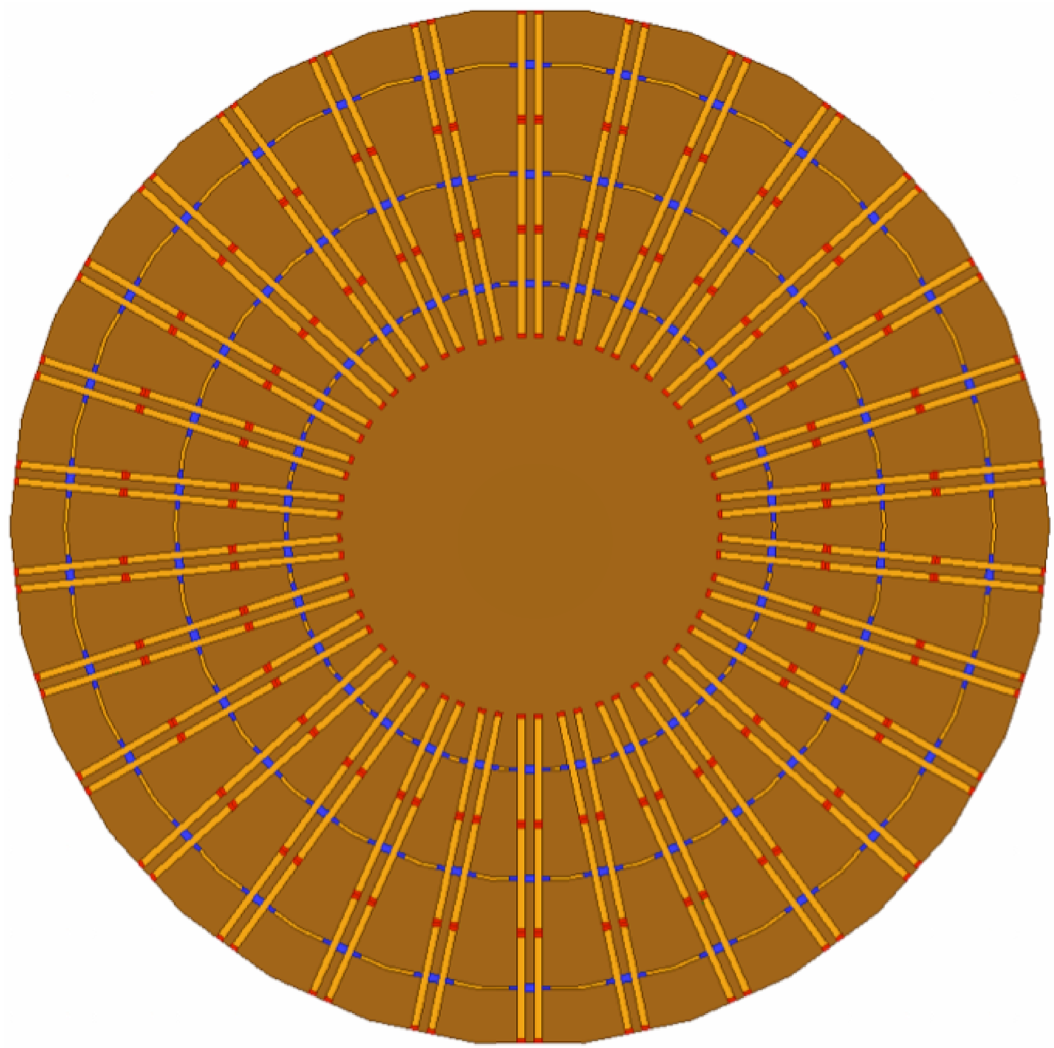

Figure 2.21: Example circular layout composed of trapezoidal unit cells.

Chapter 3

An EBG for the Suppression of Parallel-Plate Noise at X-Band

This chapter contains material that was included in a submission to the IEEE Transactions on Microwave Theory and Techniques, which at the time of this writing is under review.

3.1 Objectives

A uniplanar, printable EBG which effectively suppresses the PPW mode in the X-band (8 - 12 GHz) will be designed to validate the claims previously made. This should be achieved with a miniaturized solution, for which the EBG is under one wavelength long, and whose constituent unit cells are smaller than or equal to one-quarter wavelength at the center frequency (10 GHz). This EBG should suppress the PPW mode in two dimensions, and should involve a uniplanar EBG design that does not utilize vias. The use of lumped components should be avoided, as a fully printable solution is desired.

The resulting suppression will be validated by observing the transmission between two coaxial probes (which simulate PPW noise excitation by vias) with and without the EBG. The case with the EBG should show at least 20 dB suppression over the case without the EBG. The EBG will be designed and validated with the use of dispersion and transmission simulations, and the resulting EBG will be simulated in a complete dual-layer PPW environment. This setup will be fabricated and measured in experiment to confirm these results.

3.2 Existing Solutions

The suppression of parallel-plate noise is of interest in planar environments which are effectively shielded by metallic conductors, of which there are several prominent examples:

- High-frequency multilayered printed-circuit boards (PCBs) and monolithic microwave integrated circuits (MMICs) contain multiple ground, power, and signal planes which are typically interconnected with vias for the purpose of routing signals or power [62, 63, 97]. The suppression of parallel-plate noise is necessary to preserve signal integrity (SI) and power integrity (PI), due to increasing clock speeds in electronic circuitry and miniaturizing dimensions, which results in greater coupling between layers and traces.

- Closely spaced substrate-integrated-waveguide (SIW) components can interact due to leakage into the surrounding parallel-plate medium [98, 99].
- The introduction of shielding planes to suppress backward radiation in aperture-coupled patch antennas [100] can cause the signal to couple parasitically to the new parallel-plate mode, preventing some energy from being radiated by the antenna.

In these situations, the unwanted excitation of parallel-plate modes can cause interference and false signalling, as well as reduction of antenna radiation efficiencies, degrading the overall performance of these systems. Several solutions have been proposed and utilized to overcome these challenges.

3.2.1 Decoupling/Bypass Capacitors

Decoupling (or bypass) capacitors are used to effectively short two layers together at high frequencies [64, 65, 101–104]. The capacitor serves as a low-impedance path for high-frequency noise components, effectively shorting the layers together, and preventing the propagation of these signals. However, these capacitors are typically required to have fairly large values, and therefore take up a considerable amount of space – an undesirable characteristic in high-density circuits.

3.2.2 Embedded Capacitance Layers

A newer method by which to apply decoupling capacitance is with the use of *embedded capacitance layers* [66, 67], which are layers that are separated by an extremely thin dielectric. This thin dielectric serves to greatly increase the capacitance between layers, allowing for decoupling capacitor-type performance without taking up valuable surface space.

3.2.3 Defected Ground Structures

Defected ground structures are used to suppress parallel-plate noise by constraining the flow of currents on a given conductor [68–71]. They are generally realized by etching patterns into the conductors, such that these are uniplanar devices. While usually efficient, these devices generally lack a unifying theory of operation, causing their design to be highly empirical and difficult.

3.2.4 EBGs

A recently developed technology that has been widely adopted is the electromagnetic bandgap structure, which as been developed in several forms. Simple photonic crystal-like structures have been created which are similar to free-space devices composed of alternating layers of materials with different dielectric constants [105]. The Sievenpiper mushroom structure has been analyzed in detail and used in the suppression

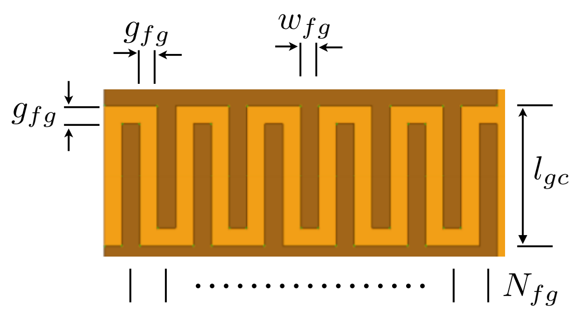

Figure 3.1: Layout of the interdigitated capacitors with relevant features indicated.

of PPW noise, for which it is readily suited [12, 47, 52–54, 106]. Many uniplanar solutions have been proposed, including several adaptations of the UC-EBG [23,107–114] . Unfortunately, these uniplanar devices are generally not modelled with the same level of accuracy as the Sievenpiper mushroom structure, and generally lack equivalent-circuit models which employ TL theory in order to determine their dispersive properties – instead typically being modelled solely with individual lumped LC elements. It is the goal of this section to develop a uniplanar EBG for PPW mode suppression, the dispersive properties of which can be accurately modelled.

3.3 Single Layer One Dimensional EBG

3.3.1 Design

In order to verify the PPW-mode suppression ability of this design, a single-layer (i.e., without an upper shield) EBG was first designed and tested. This particular EBG was designed to be fully printable in a 200μm process, and suppress PPW signals between 2.4 GHz and 6.0 GHz on a 60 mil, RO-4350 dielectric ($\epsilon = 3.66$).

Unit Cell

The unit cell period d was chosen to be 5mm, to demonstrate the possible miniaturization. At the high end of the stopband (6.0 GHz), the unit cell was then less than $\lambda_d/5$ in length, and less than $\lambda_d/13$ at the lower edge of the bandgap (2.4 GHz), where λ_d is the wavelength in the dielectric, which is appreciably small. A minimum CPW strip line width ($s = 0.2$mm) and gap widths of $g = 0.5$mm were chosen to assist in the miniaturization process. Strip inductors of width $w_L = 0.1$mm and a unit cell width $w = 10$mm were chosen to facilitate a moderately wide bandgap (since two inductors are connected in parallel between unit cells, the inductor size was still valid for this process). To achieve sufficient miniaturization, an interdigitated capacitor was used to obtain a relatively high capacitance value. The layout of this capacitor, as detailed in Fig. 3.1, has a finger width w_{fg} and finger gap g_{fg} both of 0.2mm size to maximize capacitance. The length of the capacitor is $l_{gc} = 1.6$mm, and the number of fingers used was $N_f = 11$. This design resulted in the layout shown in Fig. 3.2 (only the upper layer is shown).

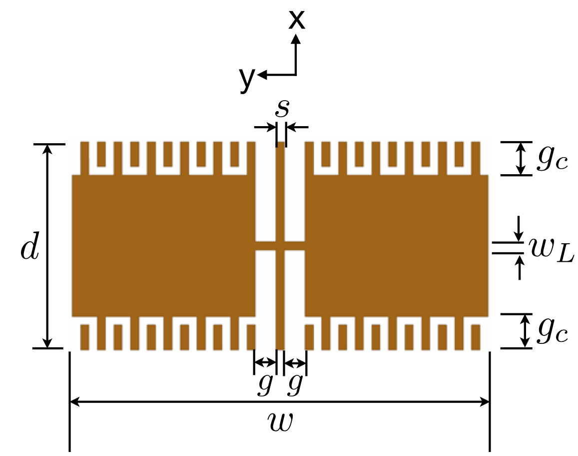

Figure 3.2: Layout of the top surface of the designed EBG unit cell.

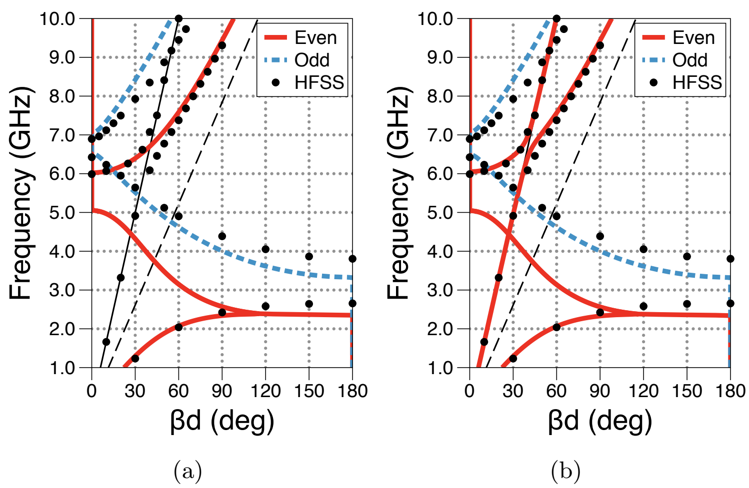

Figure 3.3: Equivalent-circuit and HFSS dispersion data, a) without upper PEC shield, and b) with upper PEC shield. Black dots are HFSS data.

Dispersion

This unit cell corresponds to the one investigated previously in Sec. 2.3, for which it was found that the equivalent lumped inductive and capacitive loading corresponded to L = 1.6 nH and C = 0.8pF, respectively. The analytical equivalent-circuit model dispersion is compared to the FEM (HFSS) simulated dispersion in Figs. 3.3a and 3.3b, which were computed with an equivalent-circuit model without and with an upper shield, respectively.

All sets of data indicate a PPW bandgap between roughly 2.4 GHz and 6.0 GHz. Additionally, the case with the shield (at a height of 100mm) seems to best reflect the HFSS data, indicating that this EBG does support a small SW bandgap. The divergence of the equivalent-circuit model and HFSS data at high phase angles is most likely due to the frequency-dependence and large physical length of the interdigitated capacitors.

Transmission

The PPW mode bandgap was tested by performing a transmission simulation across nine cascaded unit cells, as shown in Fig. 3.4a, for which a short section of unloaded PPW was used to interface the wave-ports to the EBG. The results of this simulation are shown in Fig. 3.4b, for which a stopband with 10dB insertion-loss points of 2.6 and 6.4 GHz was observed, which is very close to the design criteria, and also very close the dispersion data given by the HFSS eigenmode simulation. It should be noted that the resonant behavior below the bandgap region is owed to Fabry-Perot resonances of the highly dispersive coupled PPW-CPW mode.

3.3.2 Experiment

To confirm the simulation results, a PCB containing the designed, fully printed EBG was fabricated. Using a 60-mil Rogers RO-4350 substrate, a 5×9 grid of unit cells was connected to a PPW, in order to sufficiently approximate the simulation setup. This PPW was then linearly tapered to a 50Ω microstrip (MS) line for ease of measurement. The fabricated structure is shown in Fig. 3.5, along with the appropriate dimensions. The total length of the EBG is 45mm, and the total width is 50mm. The length of the PPW region on either side of the EBG is 10mm, and the microstrip sections are 20mm long and 3.3mm wide. The linear tapers connecting the PPW and MS were 50mm long. SMA connectors were used to interface a Keysight N5244A vector network analyzer (VNA) with the PCB to perform the measurements.

The measured data are plotted in Fig. 3.6 along with the simulated data, and it is clear that they exhibit very good general agreement, despite the finite width of the EBG section and the large taper and microstrip sections, which were not included in the simulation model. In both data the bandgap behavior of the EBG is clearly visible between 2.6 GHz and 6.4 GHz, as indicated by the dashed vertical lines. Discrepancies in the upper passband may be attributed to the frequency response of the microstrip and taper sections in the fabricated device.

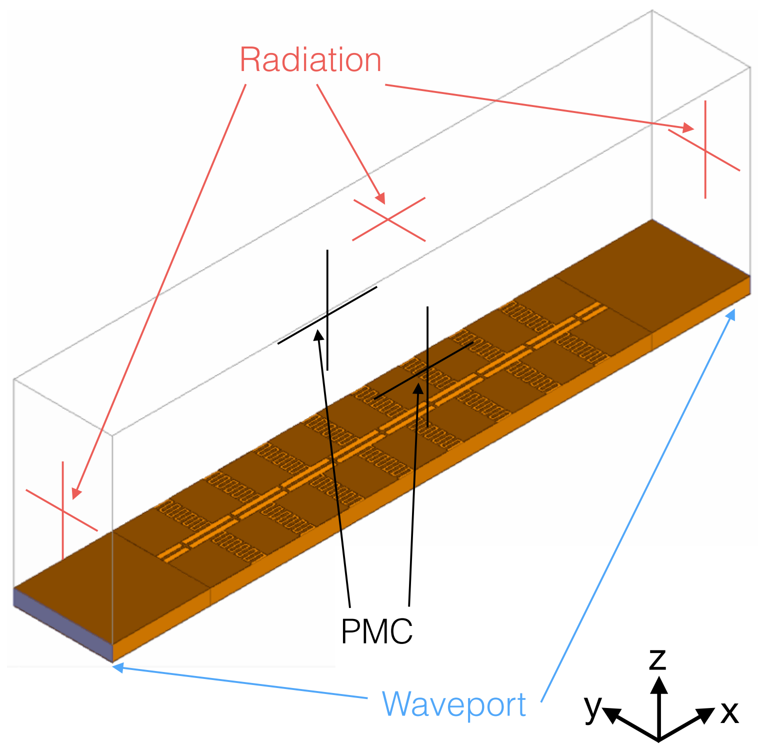

(a)

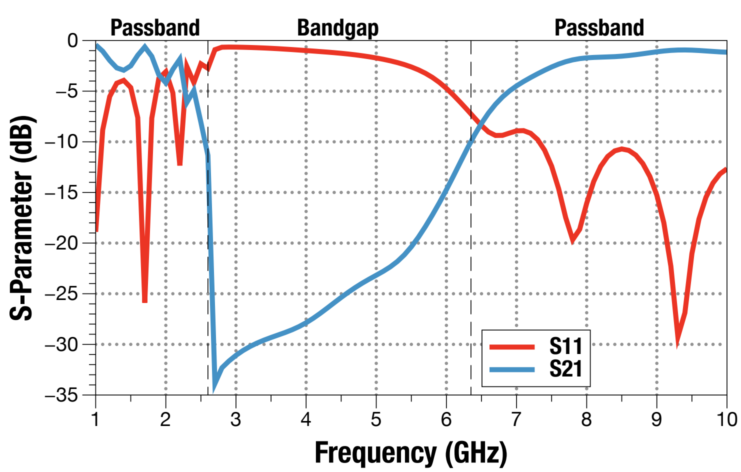

(b)

Figure 3.4: Transmission simulation of nine cascaded unit cells: a) simulation setup, b) resulting scattering parameters.

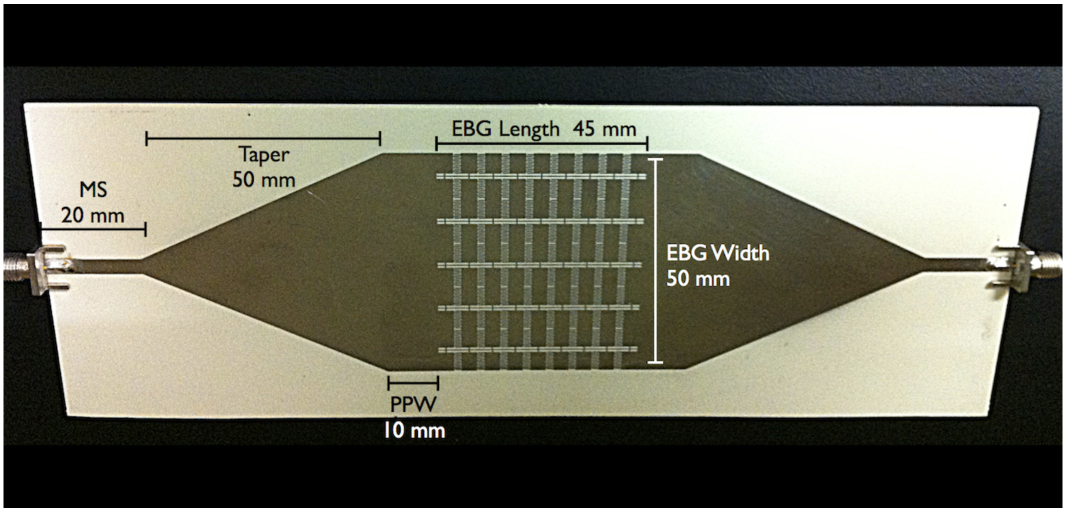

Figure 3.5: Fabricated PCB with MS, taper, and PPW regions of dimensions as indicated.

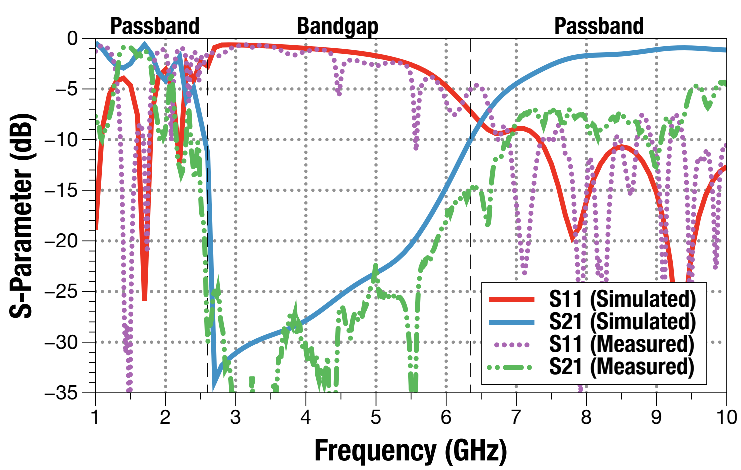

Figure 3.6: Simulated and measured scattering parameters.

3.4 Dual Layer Two Dimensional EBG

3.4.1 Design

Since one dimensional suppression of the PPW mode has been confirmed, a more realistic scenario will now be investigated. An EBG will be designed for use in a multilayer topology to suppress power transmission in two dimensions at X-band, and will be validated by its ability to suppress cylindrical PPW waves.

Unit Cell

The host medium was chosen to be constructed of one layer of RO-3010 dielectric ($\epsilon = 10.2$), 10 mils thick, and another layer of FR-4 ($\epsilon = 4.4$), 60 mils thick. The copper traces were chosen to possess a thickness of 17μm (1/2 oz.), which is common for these dielectrics. The minimum feature size was specified at 100μm, corresponding to a high-quality PCB lithography process.

The design of a structure inside of such a multilayer environment for operation only inside the X-band was very difficult to achieve. As previously investigated, the coupling between the PPW and CPW modes depends strongly on the capacitance between the conductor backing and the CPW grounds. Due to the extremely thin dielectric ($h_u = 10mils$) and the high dielectric constant ($\epsilon_u = 10.2$), this capacitance is greatly inflated from the previous case, resulting in a very wide bandgap. In order to reduce the bandwidth to cover just the X-band, the loading inductance was decreased to an extremely small value, and the unit cell width was decreased to the smallest possible value. Therefore, to achieve miniaturization, a large loading capacitance is required. The initial period chosen for the unit cells was $d = 2mm$, since this would satisfy the electrical size criteria previously specified, at $d = \lambda_g/4.7$. However, it was found that in order to create a sufficiently large interdigitated capacitance, the period of the unit cell would need to be extended to $d = 2.5mm$, which increases the electrical length of the unit cell to just under one-quarter wavelength ($d = \lambda_g/3.8$).

Dispersion

Fig. 3.7 shows the equivalent-circuit model dispersion of a unit cell with a width equal to the period of $w = 2.5mm$. The loading parameters were chosen such that $L = 0.5nH$ and $C = 0.1pF$. Subsequently, there is an extremely large upper PPW bandgap from approximately 5 to 14 GHz, and there is evidence of strong coupling between the upper and lower PPW modes from 15 to 18 GHz, which could also suppress the upper PPW mode.

Fig. 3.8 shows the dispersion result of decreasing the loading inductance value to $L = 0.01nH$ and subsequently increased the loading capacitance value to $C = 0.5pF$. As can be seen the bandgap is still wider than 4 GHz, as the dominant effect of decreasing the loading inductance value was to shift the upper edge of the PPW bandgap down to around 12 GHz. Additionally, it had the effect of shifting the CPW Γ-point upwards; subsequently, the attenuation corresponding to the CPW mode is larger than π/d Np, and cannot be seen in the figure.

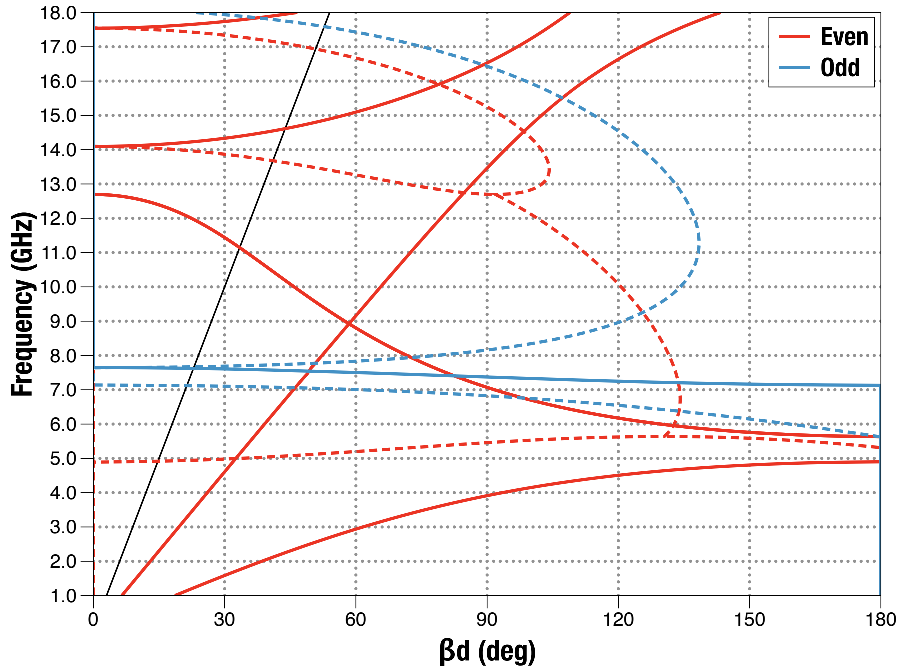

Figure 3.7: Equivalent-circuit model dispersion of a unit cell with a relatively large width and inductance, and relatively small capacitance. The PPW bandgap is much wider than desired.

In order to further reduce the size of the bandgap, the unit cell width was decreased to $w = 1.4mm$. The resulting dispersion diagram is shown in Fig. 3.9, which indicates an appropriately wide bandgap of roughly 4 GHz. However, the frequency range is not correct (approximately 6 - 10 GHz).

In order to correct the frequency range of the bandgap, the capacitance was adjusted to a lower value, such that the bandgap should shift uniformly upwards in frequency. Through an interactive process involving the transmission simulation for trapezoidal unit cells (as detailed in the next section), it was found that an optimal design was achieved by using an equivalent capacitance of $C = 0.4pF$. There are two main reasons for this iterative operation: the interdigitated capacitor is both physically large, such that it significantly perturbs the host waveguide (which is not taken into account by the equivalent-circuit model), as well as possessing a frequency-dependant value, and the transformation from a rectangular to trapezoidal unit cell does slightly impact the performance of the unit cell. The layout of the finalized printed unit cell is shown in Fig. 3.10a. The final properties were $d = 2.5mm$, $w = 1.4mm$, $s = g = w_{fg} = g_{fg} = 0.1mm$, $w_L = g_c = 0.7mm$, $N_{fg} = 3$. The dispersion corresponding to the final equivalent-circuit model, as well as the eigenmode simulation from HFSS are shown in Fig. 3.10b, which show good agreement, with a small (approximately 0.5 GHz) frequency shift around the Γ-point. The resulting bandwidth is slightly larger than desired, but was judged to be sufficiently close to the design criteria.

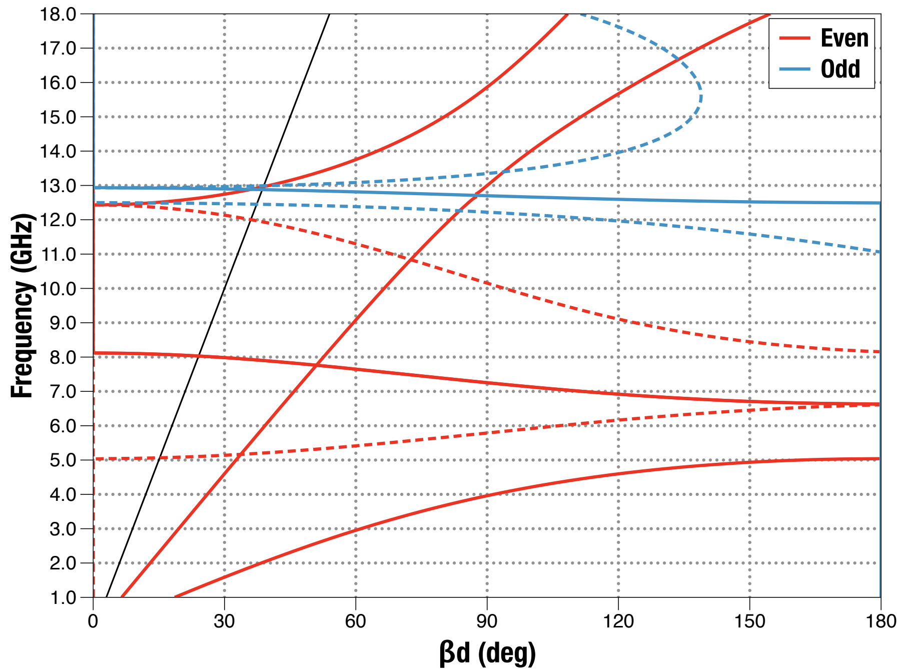

Figure 3.8: Equivalent-circuit model dispersion of a unit cell with a relatively large width and capacitance, and relatively small inductance. The decrease of the inductance predominantly shifted the upper limit downwards. The attenuation of the CPW mode is larger than π/d Np above 5 GHz.

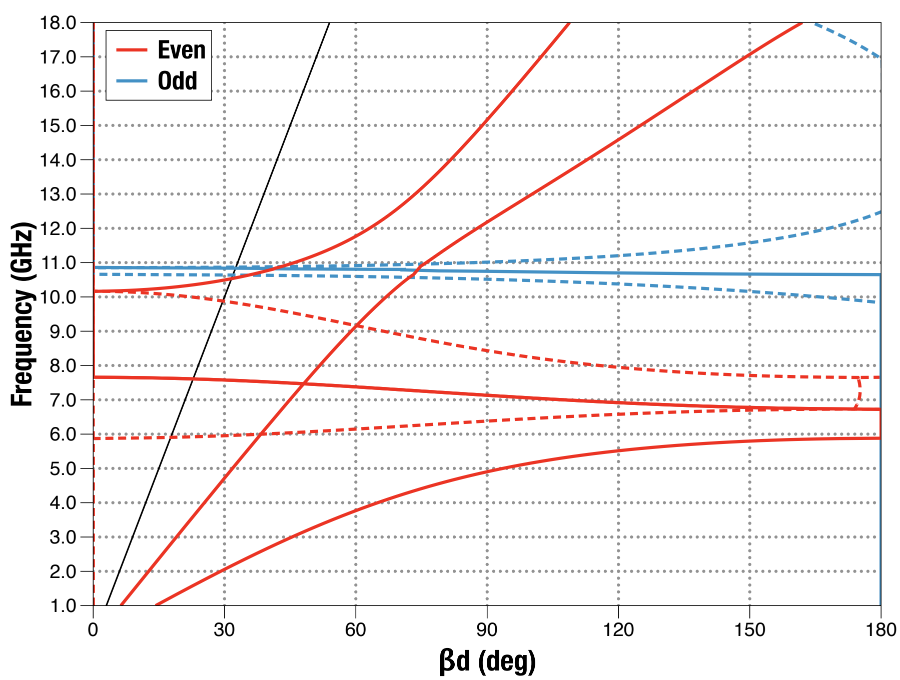

Figure 3.9: Equivalent-circuit model dispersion of a unit cell with a reduced width (1.4mm). The PPW bandgap is an appropriate width, but does not cover the correct frequency range.

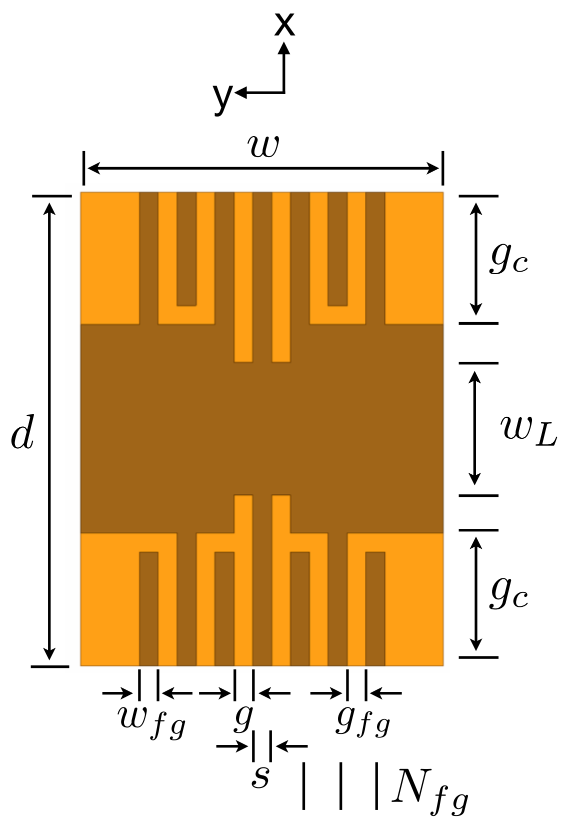

(a)

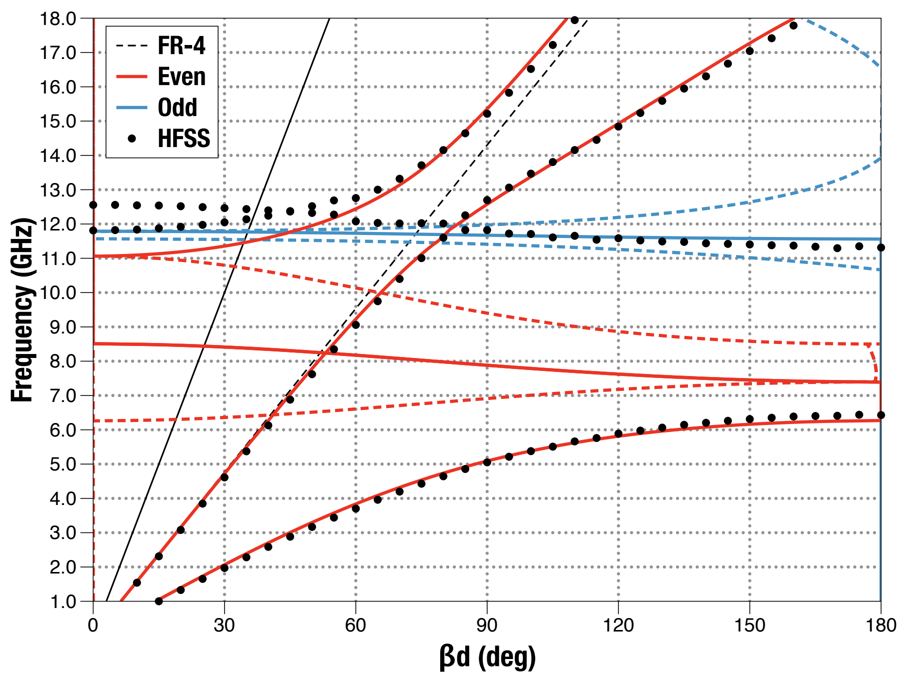

(b)

Figure 3.10: Finalized rectangular printed unit cell: a) physical layout, b) equivalent-circuit model dispersion of the final unit cell compared with the HFSS eigenmode simulation (black dots).

Transmission

The PPW mode bandgap was further validated with the use of rectangular transmission simulations, firstly on the designed rectangular unit cell. Three unit cells were cascaded, as shown in Fig. 3.11a, in order to keep the total length of the EBG under one wavelength long. The reason that the unit cells were terminated in the manner shown (with half of the interdigitated capacitors shorted to the connecting unloaded PPW) is the result of several factors unique to this design.

An ideal termination would be as dictated by the equivalent-circuit model – that is, a capacitor of value C. However, this value is double than the existing interdigitated the capacitance, which is $C/2$, and therefore should take roughly double the amount of space (since the minimum feature size is already being used, the only way to increase capacitance is to increase the length of the capacitor interdigitations). Unfortunately, there is insufficient free space in the unit cell for this to occur, as it was previously shown that the width of the unit cell cannot be increased without further increasing the frequency range of the bandgap. An alternate solution would be to extend the length of the interdigitations into the unloaded PPW. However, this would be increasing the effective length of the unit cells, such that the equivalent-circuit model would not accurately realized. Subsequently, it was decided that all of the unit cells should have the same *physical* parameters, rather than electrical parameters, since an electrically accurate termination could not be realized.

The resulting scattering parameters are shown in Fig. 3.11b. The upper PPW mode bandgap agrees very well with the dispersion, showing 10 dB insertion loss points of approximately 6.2 and 12 GHz. The peak rejection is around -30dB, indicating approximately 10dB of rejection per unit cell. The coupling between the forward upper and lower PPW modes shows two peaks around 5.5 and 13 GHz. The peak at 13 GHz is attributed to the region of maximal coupling between the two modes (corresponding to the highest suppression of the *lower* PPW mode), whereas the cause of the peak around 5.5 GHz is unknown.

The next step in the design of the two-dimensional EBG is to distort the rectangular unit cell into a trapezoidal form. Using an average unit cell width of 1.9mm, it was found that an arc length of 10^o was sufficient with a inner circle radius of 7.5mm (in order to avoid truncation of the capacitor interdigitations), inner unit cell width of 1.3mm, and outer unit cell width of 2.6mm, as shown in Fig. 3.12a. The resulting scattering parameters are shown in Fig. 3.12b, which show that the upper PPW mode bandgap fits adequately into the prescribed bandwidth.

3.4.2 Simulation

Once the suppression properties of the trapezoidal section were confirmed, the full two-dimensional EBG was simulated and verified with the use of two vias connected between the shield and the middle conductive layer, used to excite the upper PPW mode. A finite 80×60 mm section of the dual-layer PPW was

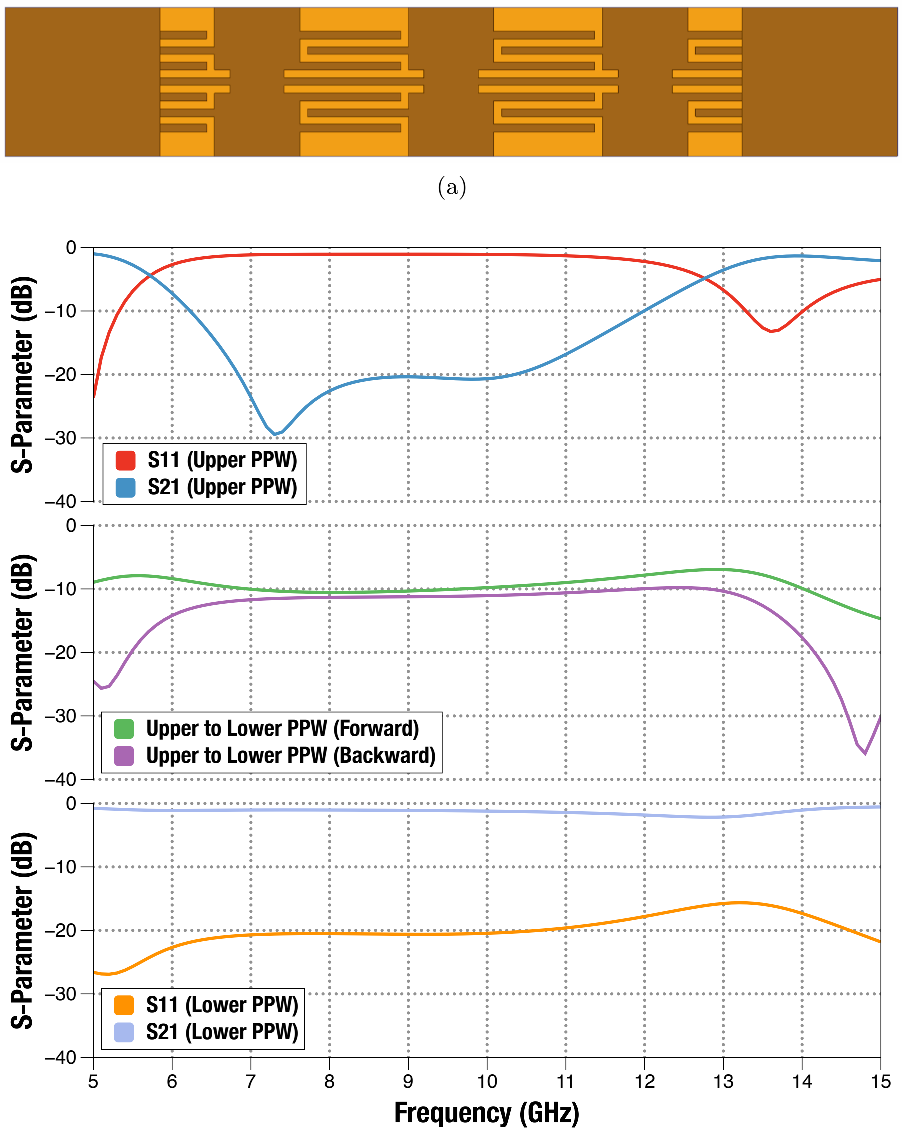

(a)

(b)

Figure 3.11: Transmission of rectangular printed unit cell cascade: a) physical layout, b) resulting scattering parameters.

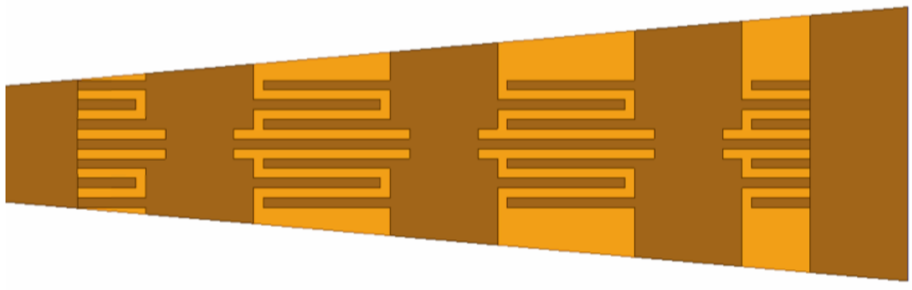

(a)

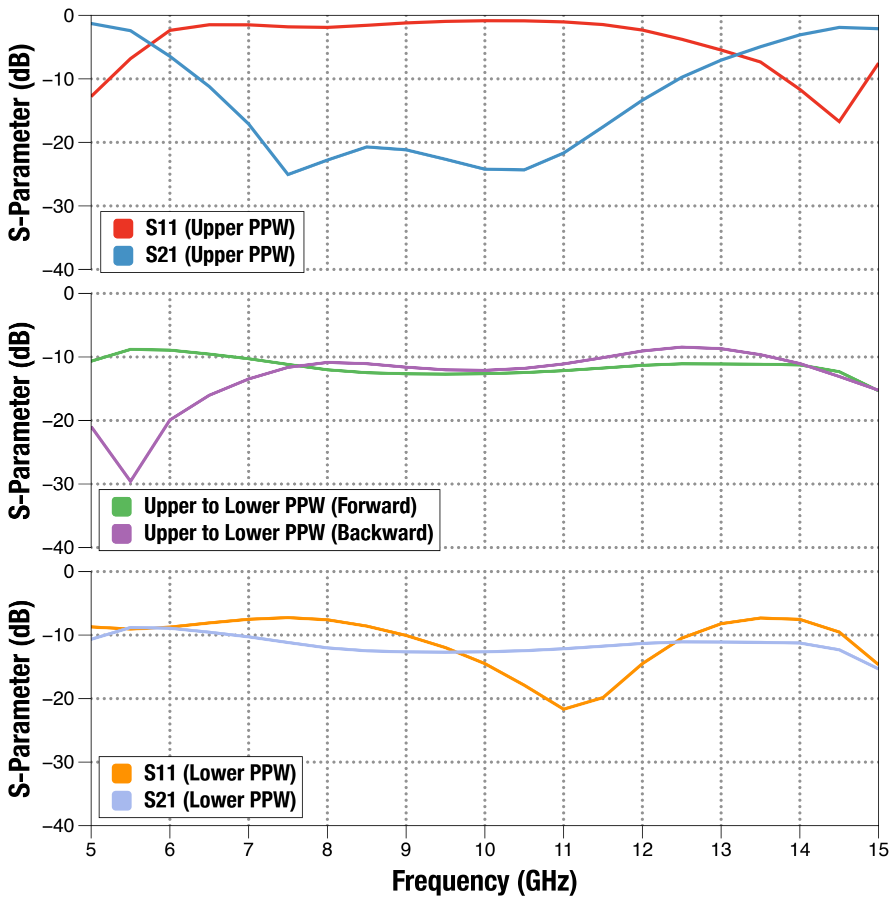

(b)

Figure 3.12: Finalized trapezoidal printed unit cell cascade: a) physical layout, b) resulting scattering parameters.

created, and the EBG formed by removing sections of copper in the middle conductive layer. 36 periods of the trapezoidal EBG were arranged around one of the vias to form a closed circle. The vias were used for both excitation and detection, and were designed to be matched to 50-Ω, teflon-filled SMA connectors, and were separated by 20mm. The distance between the center of the excitation via and the inner radius of the EBG was 7.5mm, as used in the design of the trapezoidal EBG transmission simulation. This layout is shown in Figs. 3.13a and 3.13b.

The resulting scattering parameters of this arrangement are shown in Fig. 3.14, in which suppression of up to roughly 45 dB is observed over approximately 7 to 11.5 GHz when the EBG is present. Interactions at the interface between the coaxial SMA connectors and RO-3010 dielectric, as well as resonances between the vias and the radial EBG structure, do obscure the suppression near 7 and 11.5 GHz, but nevertheless maintain significant improvement over the case without the EBG at all stopband frequencies. The "noise" in the scattering parameters is a result of the finite size of the PCB, the outer edges of which are very effective open circuits. The large, two-dimensional nature of the PPW then supports a large spectrum of resonances, which give rise to a strong frequency-dependance in the insertion and return losses. It should be noted that the return loss in the case with the EBG (measured at the via inside the EBG) is extremely smooth – since the EBG does not support these resonances.

The fields at 5 GHz (outside the stopband) and 10 GHz (inside the stopband), are shown in Figs. 3.15c through 3.15f. Figs. 3.15c and 3.15d show the complex magnitude current densities on the top surface of the middle conductive layer – outside and inside the bandgap, respectively. As expected, the currents at 10 GHz show a drop in the field level by approximately two orders of magnitude (40 dB), confirming the suppression suggested by the scattering parameters. The null between the EBG and the excitation via is evidence of the standing wave created by the signal being reflected by the EBG, and is noticeably absent at 5 GHz where the EBG essentially transmits the PPW mode. Figs. 3.15e and 3.15f show the complex magnitude magnetic fields on an orthogonal plane which passes through both vias. It can be seen in these figures that the field decay primarily takes place inside the EBG region as expected. There is some field leakage into the FR-4 layer, but it appears to be confined within the EBG region and is relatively small in magnitude (approximately 10 dB lower than the maximum fields in the RO-3010 dielectric). At 5 GHz, the fields are still constrained by the EBG (the currents must still pass through the thin CPW strips), but the transmission is similar to the case without the EBG, as indicated by the field strengths over the outer-most unit cells. There is also slightly less leakage into the lower dielectric, indicating that the upper PPW mode is better guided by the EBG at this frequency.

3.4.3 Experiment

In order to confirm the simulated scattering parameters, the design detailed in the previous section was manufactured and tested. The printed structure was laser etched courtesy of LPKF [115], and the bottom

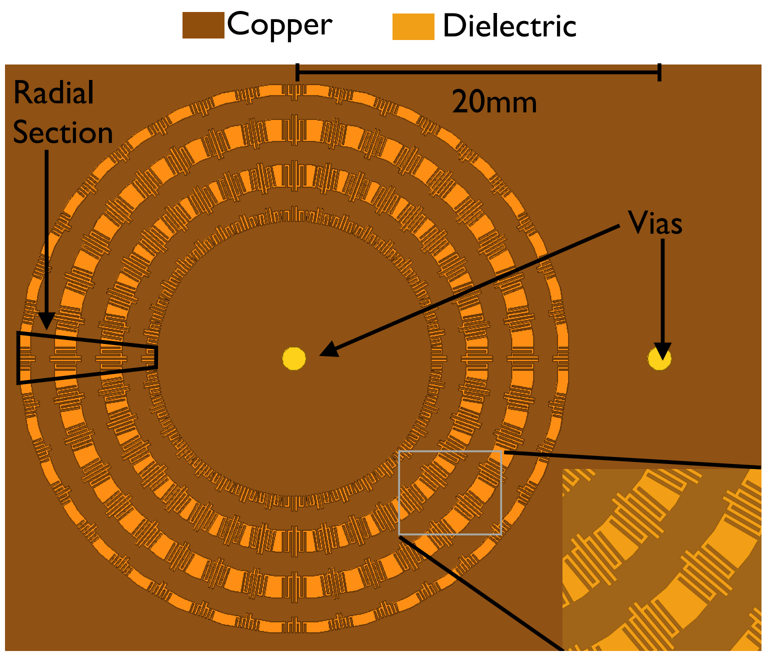

(a)

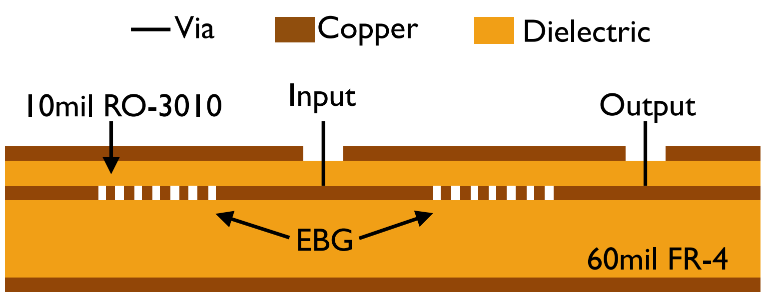

(b)

Figure 3.13: Example setup for two-layer via-induced PPW noise suppressing radial EBG a) top view, b) side view.

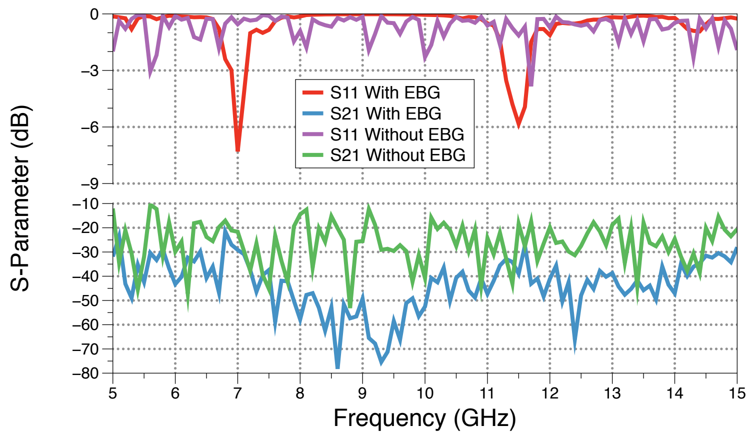

Figure 3.14: Simulated scattering parameters between two vias in a PPW with and without the EBG.

of the fabricated PCB is shown in Fig. 3.16. A microscopic examination of the structure showed that the resulting EBG was realized very accurately, especially in the interdigitations of the innermost unit cell, which was etched accurately down to a feature size of at least 40μm, as indicated by the inset.

The vias were realized by inserting the pin of flush-mount sub-miniature 'A' (SMA) connectors through the drill holes, and soldering the pin to the EBG layer. The bodies of the SMA connectors were soldered to the reverse side of the PCB (the shield). This assembly was then connected to a similarly sized slab of 60mil FR-4, with the copper cladding removed from one side (this side was placed adjacent to the conductive layer containing the EBG).

The two layers (FR-4 and RO-3010) were compressed together to ensure accuracy using two clamps on the long ends of the PCBs. The pressure was distributed with the use of a hard plastic O-ring with a rectangular aperture (approximately 25mm thick) and a layer of firm styrofoam (approximately 14mm thick). The entire assembly is detailed in Fig. 3.17, and photographs of this setup are shown in Figs. 3.18a (side view) and 3.18b (top view). A layer of masking tape was used to hold the two dielectrics together, and prevent them from sliding laterally.

The resulting scattering parameters are fairly similar to those of the simulated structure, but there is a noticeable frequency shift between the two data sets – the measurements seem to fit well within the X-band, whereas the simulated data shows the same profile, but frequency shifted downwards by nearly 0.5 GHz (7%). It was found that in order to match the data, the value of ϵ_u needed to be decreased to 9.7, as allowed by the specified manufacturing tolerance, and the creation of a 2 mil air gap between layers, which is reasonable since the layers were only mechanically compressed together and not bonded. These results are shown in Fig. 3.19, which shows much better matching with the measured data. The more subtle suppression above 12 GHz is attributed to coupling between the PPW modes of the two layers, as predicted by the dispersive properties.

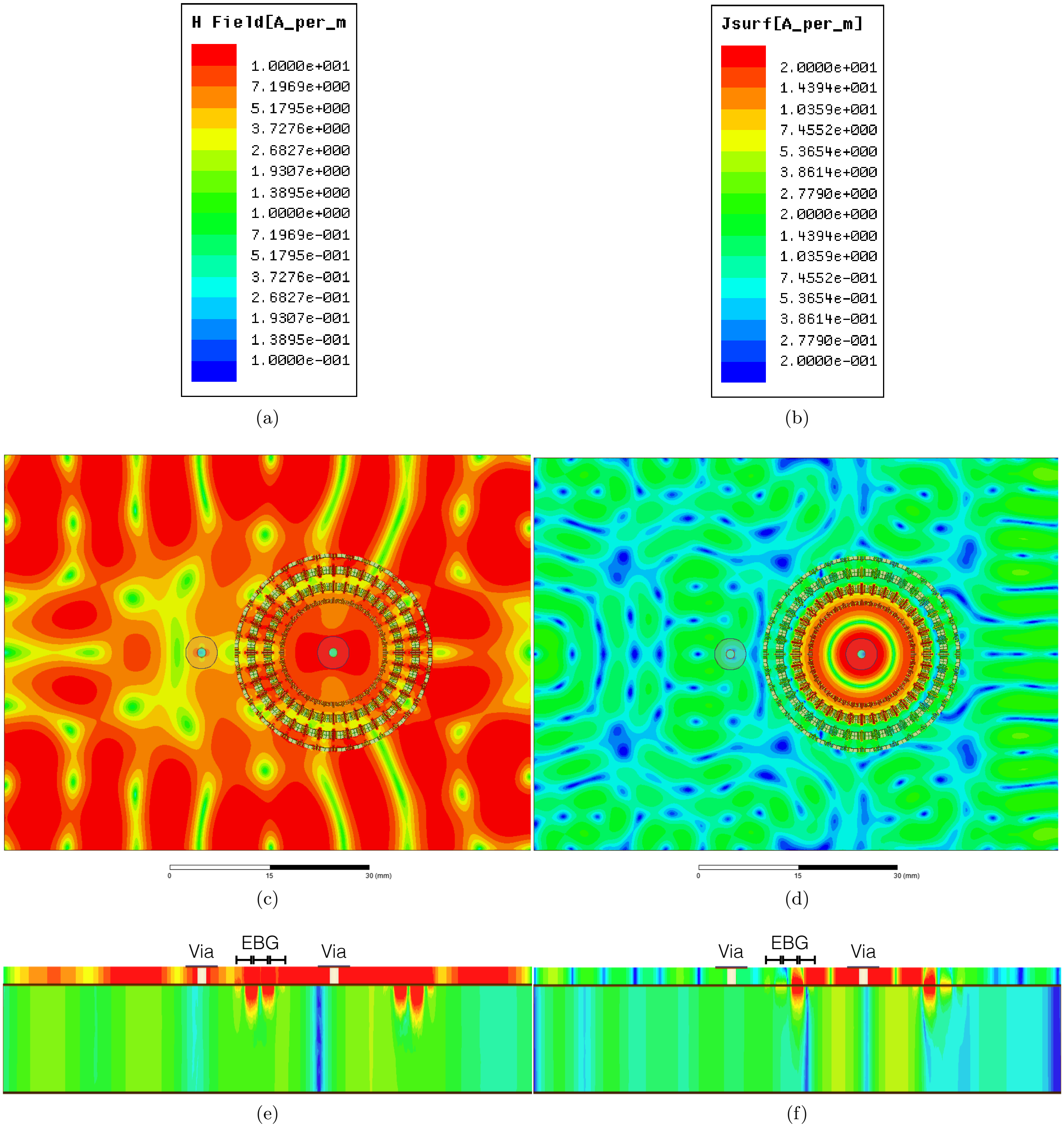

Figure 3.15: Simulated complex-magnitude fields: a) legend for magnetic fields, b) legend for surface currents, c) surface currents at 5 GHz, d) surface currents at 10 GHz, e) magnetic fields at 5 GHz, f) magnetic fields at 10 GHz.

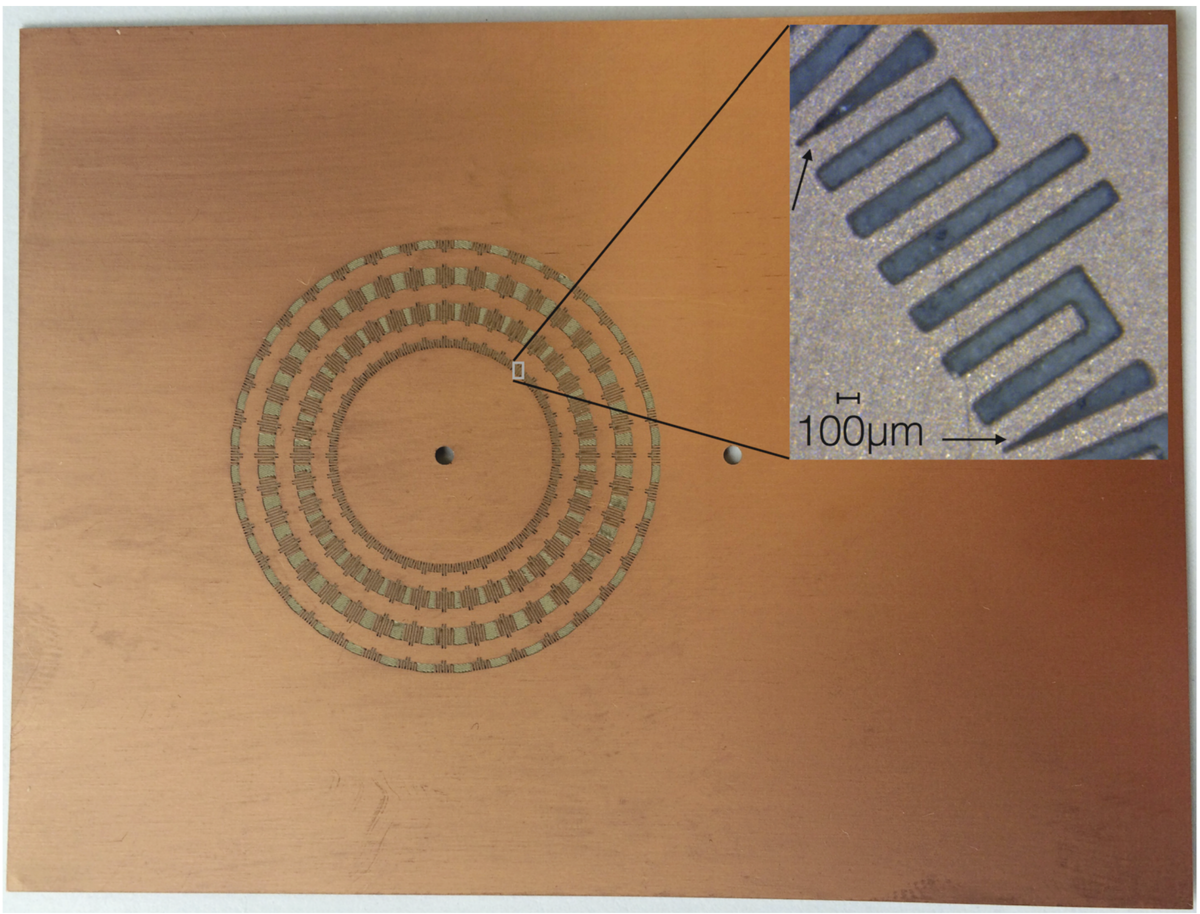

Figure 3.16: Fabricated experimental setup (case with EBG). The inset shows the accuracy of the etching process, indicating the small feature sizes.

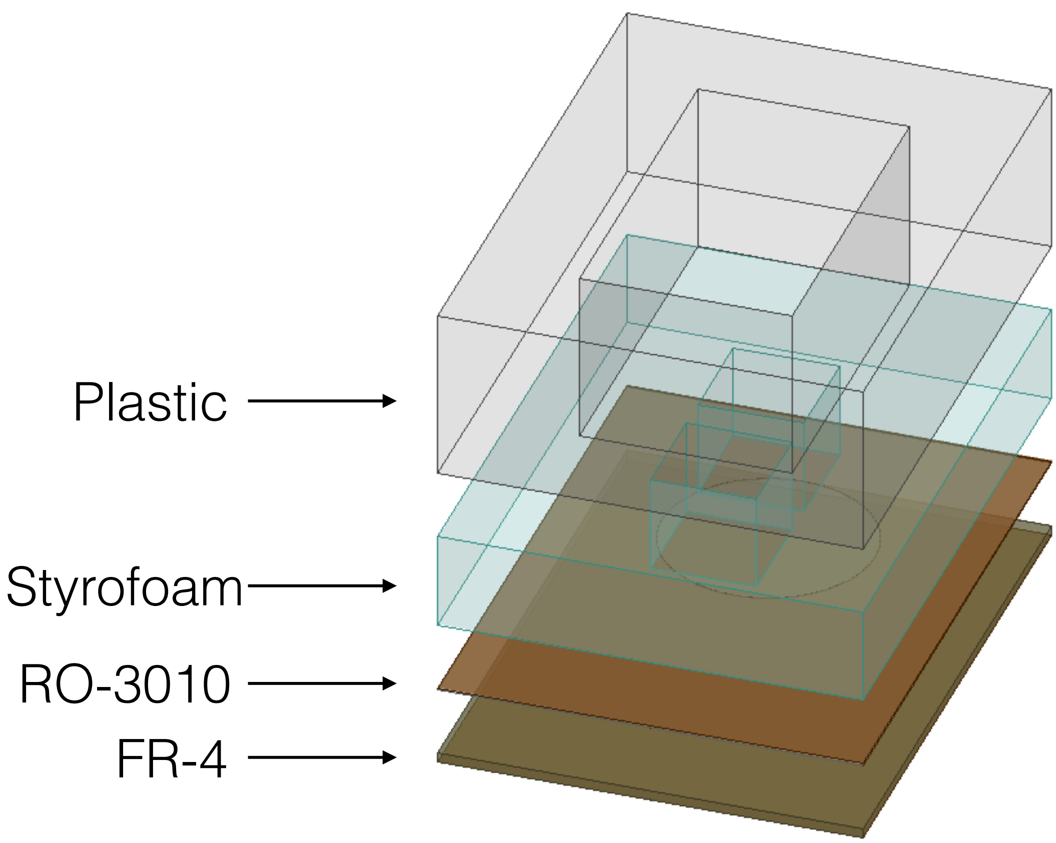

Figure 3.17: 3D model detailing various layers in experimental setup.

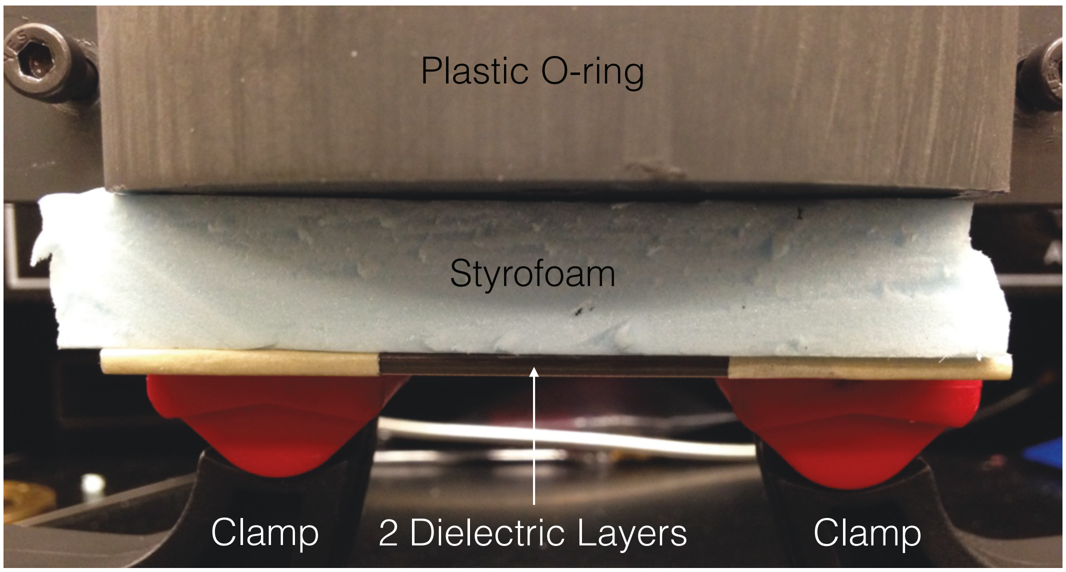

(a)

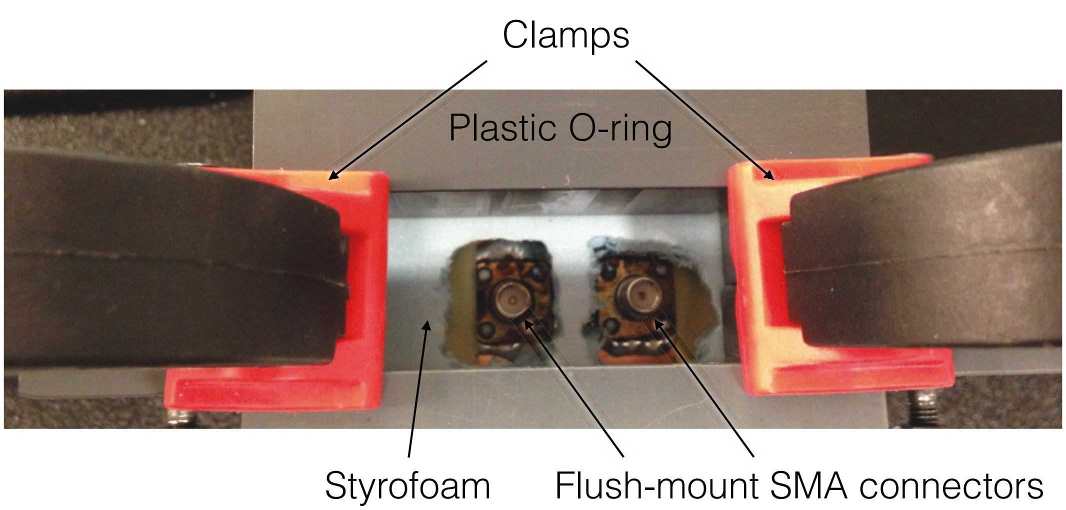

(b)

Figure 3.18: Photogrpahs of experimental setup for measurement of the PPW-noise suppressing EBG: a) side view, b) top view.

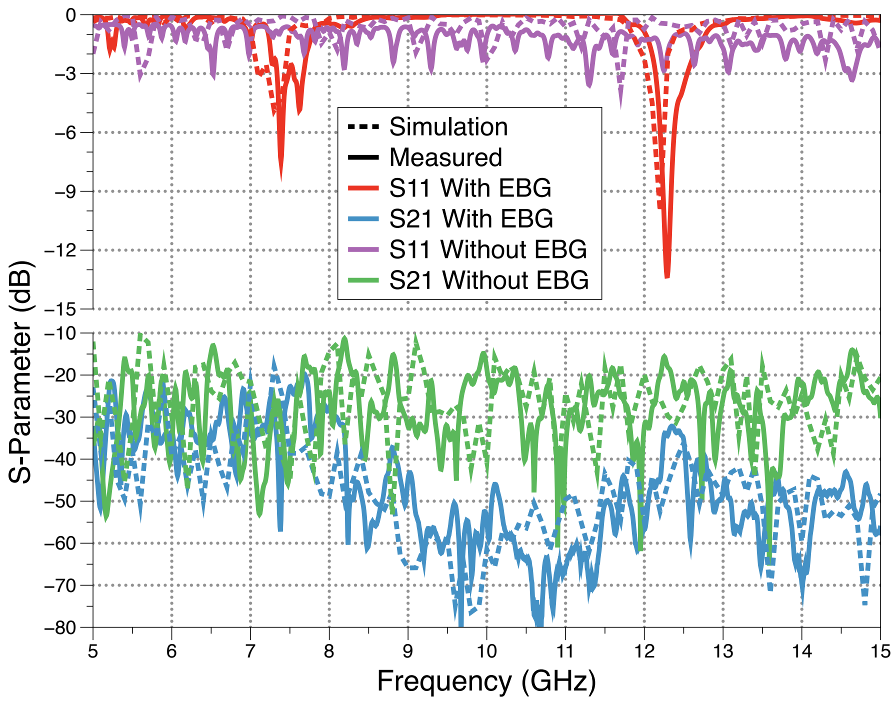

Figure 3.19: Simulated (dashed) and measured (solid) scattering parameters between two vias in a PPW, with and without the EBG.

This discrepancy can be attributed to anticipated variations in the upper dielectric permittivity, or possibly also a small reduction in the dielectric thickness. It may be possible that the thin (10 mil) dielectric was compressed slightly during manufacturing, resulting in a small reduction in the capacitance value of the interdigitated loading capacitors, and shifting the bandgap upwards.

In summary, the measurements seem to validate the fact that a bandgap is present in the upper PPW mode for suppression in two dimensions, and its operating frequency range can be tailored by specific design of the EBG.

Chapter 4

A TM_0 Surface-Wave Suppressing Ground Plane for GPS Antennas

4.1 Objectives

An EBG which effectively suppresses the SW at GPS L1 (1.575 GHz) and L2 (1.228 GHz) frequencies will be designed as another validation of the theory presented in this work. This will be achieved with a miniaturized solution, for which the EBG extends no more than 100mm away from the original antenna ground plane. This extension should be relatively thin, such as provided by a standard dielectric substrate (e.g., 60 mils), and involves a uniplanar EBG design that does not require the use of vias. The use of lumped components will be avoided, as a fully printable solution is desired.

The resulting radiative properties will be characterized through four specific properties: right-handed circularly polarized (RHCP) and left-handed circularly polarized (LHCP) realized gains (gain relative to input power), the axial ratio (AR), and the multipath ratio (MPR), defined in this work as:

$$MPR = \frac{RHCP\,(\theta)}{LHCP\,(180^o - \theta)} \tag{4.1}$$

The RHCP should exhibit a high azimuthal symmetry, with no more than 1dBi variation. The MPR should be at least 10 dB on the horizon, and the LHCP should exhibit at most -20 dBi realized gain on and near the horizon. The RHCP realized gain should be as large as possible.

The surface-wave suppression will be confirmed by dispersion and transmission simulations, and the resulting antenna simulations and measurements should reflect this performance by a reduction in gain (preferably, LHCP gain only, but RHCP gain loss may be unavoidable) on and near the horizon. The resulting radiation pattern should also exhibit high azimuthal symmetry, which is difficult to achieve when using square or rectangular EBGs.

4.2 Existing Solutions

Several solutions for SW suppression in GPS antennas have previously been proposed and realized. This section reviews some of the popular technologies that have been applied specifically to GPS antennas.

4.2.1 Resistive Ground Planes

Early attempts at suppressing the SW mode in a compact manner resulted in the development of the resistive ground plane [80,81,116]. These ground planes possess a very high resistivity, such that currents associated with the SW mode are highly attenuated via ohmic losses. Since this ground plane does not depend on any resonant conditions, it does not need to have features with an electrically resonant size, allowing a very thin, light, ground plane. Unfortunately, the final results obtained by using these ground planes are not as desirable as those obtained with other methods, such that this technology is not widely used.

4.2.2 Choke Rings

Choke rings are composed of a series of thin, hollow, metallic cylinders which are arranged concentrically around the antenna element [77, 78]. These structures are essentially corrugated ground planes arranged around an antenna in a circular fashion. Choke rings operate very well, with high degrees of suppression and relatively large bandwidths, but are undesirable due to their weight, size, and cost – since they are generally made from solid metal and must be near one-quarter wavelength in height.

The corrugated ground plane that forms the choke ring structure operates on a fairly simple resonance principle. At frequencies for which the depth of each corrugation is integer multiples of one-quarter wavelength (corresponding to a vertically arranged shorted quarter-wavelength TL), the fields in the corrugation resonate with a field profile that can couple to the SW mode. This coupling causes the formation of a bandgap, such that the choke ring could be classified as an EBG, similar to the corrugated ground plane.

4.2.3 Planar EBGs

SW suppressing planar EBGs (such as the Sievenpiper mushroom structure) have been widely used in GPS antennas [117–121]. As previously described, the SW bandgap presented by these EBGs causes the reflection of SW modes, similar to the choke rings, but in a smaller, lighter, and more cost-efficient form. A fully printable, uniplanar EBG is designed and analyzed in this chapter.

4.2.4 Artificial Magnetic Conductors

Artificial Magnetic Conductors (AMCs, equivalent to the previously introduced PMCs) are generally considered related to EBGs, and for that reason are usually created out of EBG structures [122, 123]. The origins of this link can be traced back to the first EBGs [10, 124], in which the SW suppression ability of the EBGs was described by modelling the EBG surface at its bandgap center frequency as a magnetic conductor, which theoretically do not support TM surface-wave modes.

Unfortunately, ideal AMCs do support TE modes, specifically the TE_0 mode, which has no cutoff frequency. This result can be simply arrived at by invoking duality, as specifically mentioned in [10]. The presence of the TE_0 mode is not an issue in linearly polarized antennas, but critically since GPS antennas operate on circular polarizations, the presence of the TE_0 surface-wave mode is just as detrimental as the presence of the TM_0 surface-wave mode, such that an AMC should be just as undesirable as a PEC ground plane (this can, of course, be verified in simulation, where ideal PMCs can be easily used). Therefore, the AMC properties of the EBGs developed in this work will not be investigated.

4.3 Design

4.3.1 Unit Cell

The S-CBCPW structure is an ideal host waveguide for this problem, since it is uniplanar and can be used to suppress the SW mode (approximated by the upper PPW mode). Furthermore, since the shield is not needed in reality (it is only need to model the SW), a single copper-clad dielectric can be used in realizing the EBG. In order to help achieve miniaturization, a high dielectric constant material was used. The high dielectric constant has little bearing on the SW mode, but allows the CPW and PPW Bloch modes to naturally exist at lower frequencies. Additionally, the printed capacitive loading elements (i.e., interdigitated capacitors) will gain a slight increase to their capacitance for an equivalent physical size.

To meet these requirements, Rogers RO-3010 was chosen as the dielectric material, due to its high and stable dielectric constant. The exact choice of dielectric material led to the following S-CBCPW parameters: $h_l = 1.270mm$ (50 mils), $h_u = 100mm$, $\epsilon_l = 10.2$, $\epsilon_u = 1.0$, and $t = 17\mu m$ (1/2 oz.).

Through the study of equivalent-circuit models, it was found the the size of the SW bandgaps depended heavily on the period d and the inductive loading L. Specifically, small values of d or large values of L generally made the SW bandgaps so small that they would be nearly unusable, as shown in the parametric sweep of Fig. 4.1. This figure details the bandgap region for a unit cell with properties $d = 10mm$, $w = 10mm$, $h_l = 1.524mm$, $h_u = 100mm$, $\epsilon_l = 10.2$, $\epsilon_u = 1.0$, $g = 0.5mm$, $s = 0.5mm$, $t = 35\mu m$, $C_s = 2.5pF$, $C_g = 0.1pF$, and a swept loading inductance L. Additionally, too large of capacitance in compensation would remove the ability to tune the operating frequency. Therefore, the unit cell was designed to have a moderate period of $d = 30mm$, which was chosen such that three unit cells could fit into the total 100mm length. Additionally, in order to achieve suppression at both L1 and L2, two bandgaps are required, and subsequently the equivalent-circuit model with the capacitor in the CPW strip line in addition to the CPW grounds was chosen.

The circular layout of the EBG previously used was chosen in order to satisfy the requirements of sup-

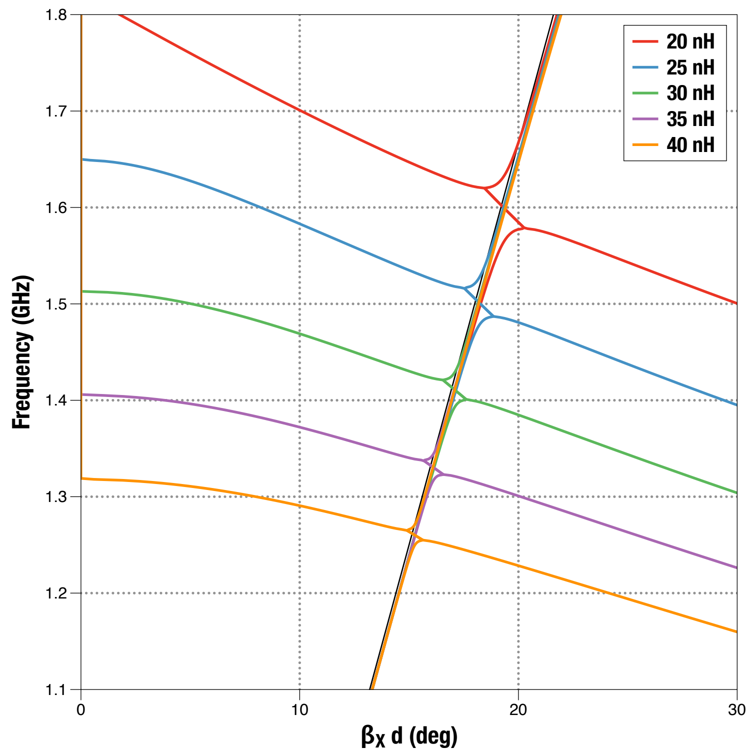

Figure 4.1: Example of a unit cell with a relatively small period and high inductive loading. The SW bandgap diminishes quickly with increasing loading inductance. Only imaginary component shown for clarity.

pression at all angles around the azimuth, and furthermore a unit cell average width $w_a = 20mm$ was chosen in order to help satisfy the requirement of azimuthal symmetry (a smaller width corresponds to a smaller azimuthal period, and hence higher azimuthal homogeneity). In order to allow adequate space for printed loading capacitors, especially embedded in the CPW strip line, a strip width $s = 2.5mm$ was chosen. Additionally, to allow space for meandered inductors, a gap width $g = 2.0mm$ was chosen. Initially, discrete reactive surfaces were used to model the loading components, similar to the previous chapter. The physical properties of these surfaces were $l_{gc} = 0.5mm$, $w_{gc} = 0.5mm$, and $w_l = 0.5mm$.

4.3.2 Dispersion

The values of the loading components were then determined by examining the dispersive properties of the unit cell. Firstly, observing the unloaded modes revealed that the lower PPW mode has an X-point near 1.6 GHz. This is useful in design, because then the loaded PPW mode will be bound between its cutoff frequency, determined by the values of the loading capacitors, and this X-point frequency. Next, the modes must be loosely coupled in order to allow both the upper and lower regions of the coupled CPW-PPW modes to couple with the SW mode. Since for thin dielectrics, the coupling between the PPW and CPW modes is typically very high, the dispersions of these modes must be judiciously chosen such that there is minimal phase matching between the two. As it was previously indicated that the PPW mode would be bound between two frequencies, it is possible to choose the CPW mode such that it it close, but not too much so, to the PPW mode on the dispersion diagram. Furthermore, to achieve dual band operation, both the upper and lower regions of the CPW can be tailored such that these regions enclose the PPW mode, with the backward wave region below and the forward wave region above. The Γ-point of the forward region was chosen to be close to the X-point of the PPW mode, such that the loading inductance could be minimized.

Once the value of inductance was minimized, the values of the loading capacitors were set by adjusting the bandgaps to exist at GPS L1 and L2. Through parametric study it was found that the the loading capacitors in the CPW grounds (C_g) controlled primarily the frequency of the L1 bandgap, while the loading capacitor in the CPW strip line (C_g) controlled primarily the frequency of the L2 bandgap. Finally, the unit cell period was finely adjusted to allow for final adjustment of bandgap frequencies.

This design process resulted in the loading component values $L = 1.5nH$, $C_g = 0.6pF$, $C_s = 2.5pF$, and period $d = 29mm$. It should be noted that the modal coupling takes place between both forward-forward modes, and forward-backward modes. These types of coupling are acceptable, since all that is needed is the suppression of the SW mode. The power in the PPW mode is dissipated in the dielectric, where it does not effect the antenna element. The resulting dispersion diagram, along with the isolated modes, is shown in Fig. 4.2. The dispersion is fairly complex, can be analyzed in light of the studies previously undertaken regarding the equivalent-circuit nature of each point. The lower Γ-point around L2 and the upper X-point around L1 remain roughly similar in the coupled and isolated systems. The Γ-points of both the CPW and PPW modes in the coupled system have shifted upwards, indicating that the parasitic effects of both the conductor backing and loading inductance serve to shift these frequencies upwards. The extreme phase mismatch of the isolated CPW and PPW modes allows for a relatively small complex-mode bandwidth.

4.3.3 Transmission

The designed unit cell was then tested in a transmission simulation, which due to the PMCs on its transverse boundaries simulate an infinite array in the transverse direction, first in its rectangular form. Three unit cells employing lumped loading elements were cascaded as shown in Fig. 2.20a, and the resulting scattering parameters are shown in Fig. 4.3. These results indicate a maximum of approximately 9 dB SW suppression near L1 and approximately 2 dB suppression near L2. The coupling of the SW mode into the lower PPW mode is also shown, indicating that the power of the SW is indeed being transduced into the PPW mode around the bandgap regions. Since the L1 SW bandgap is caused by an essentially flat mode, power couples almost uniformly in both the forward and backward directions. The L2 bandgap is formed by the intersection of the SW mode with a slightly forward directed mode, hence there is slightly more power coupled to the forward direction.

Next, the rectangular transmission unit cells were transformed into a trapezoidal configuration with a 12^o arc length. Specifying a short end width of approximately 10mm gives a long end length of approximately 30mm and average width of approximately 20mm. The results of this simulation are also shown in Fig. 4.4, which indicates a roughly similar scattering parameter set to the rectangular case, as expected. Small differences such as the shift in rejection frequencies and a slight rebalance in the forward-backward coupling with the lower PPW mode is expected due to the slightly different behavior of each unit cell.

Finally, the lumped loading components were converted into printable components, specifically in the form of strip inductors and interdigitated capacitors. These components were designed to be manufactured using a standard etching process with a $200\mu m$ minimum feature size. Using empirical equations for these components [125, 126], initial designs were created which were within approximately 50% of the desired value. Parametric sweeps were then completed on the various physical parameters were completed to achieve the desired capacitance. The parameters of the interdigitated capacitors, detailed in Figs. 4.5a and 4.5b, are, for the CPW strip line capacitor $N_{fs} = 7$ fingers, length $l_{sc} = 4.7mm$, finger spacing $g_{fs} = 0.2mm$, and finger width $w_{fs} = 0.2mm$. The CPW ground capacitors have properties $N_{fg} = 9$ fingers, length $l_{gc} = 0.6mm$, finger spacing $g_{fg} = 0.2mm$, and finger width $w_{fg} = 0.2mm$. The strip inductors have a width of $w_l = 1.0mm$.

The results of a transmission simulation using this structure are shown in Fig. 4.6. Importantly, this was the final design used for this GPS antenna ground plane. The final values were determined via a parametric sweep in the *antenna* simulation, introduced and described in the next section, which is why

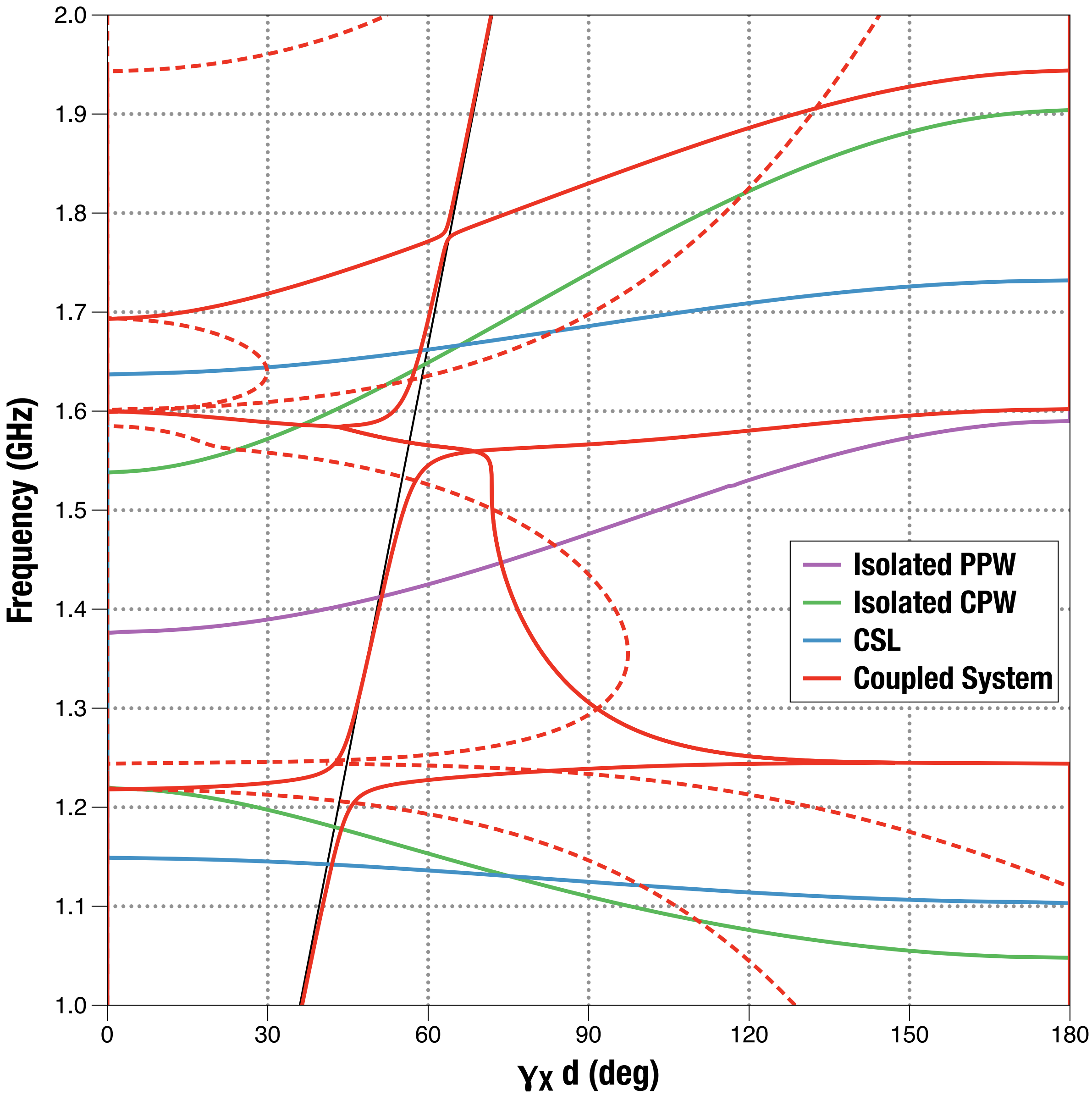

Figure 4.2: Designed dispersion diagram based on equivalent-circuit model. The isolated PPW (purple) and isolated CPW (green) modes couple strongly to give the coupled (red) modes. Only the real (attenuating) components of the coupled system are shown for clarity.

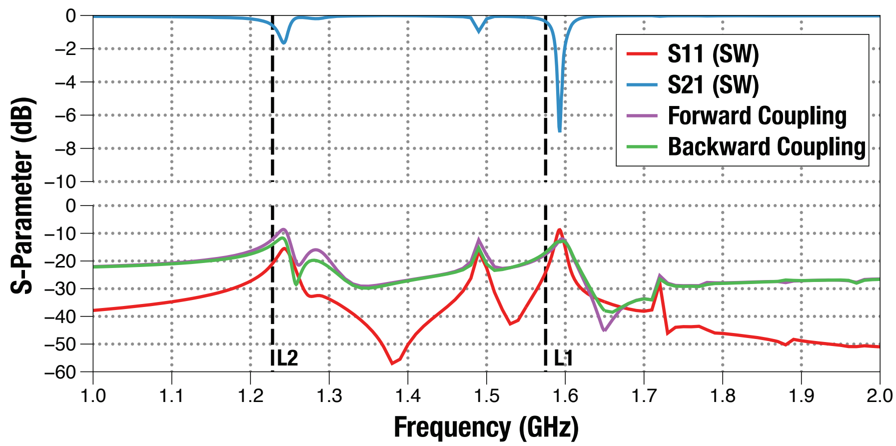

Figure 4.3: Transmission simulation results of three rectangular EBG unit cells with lumped loading components, showing both the SW (Upper PPW) mode scattering parameters, and coupling with the lower PPW mode.

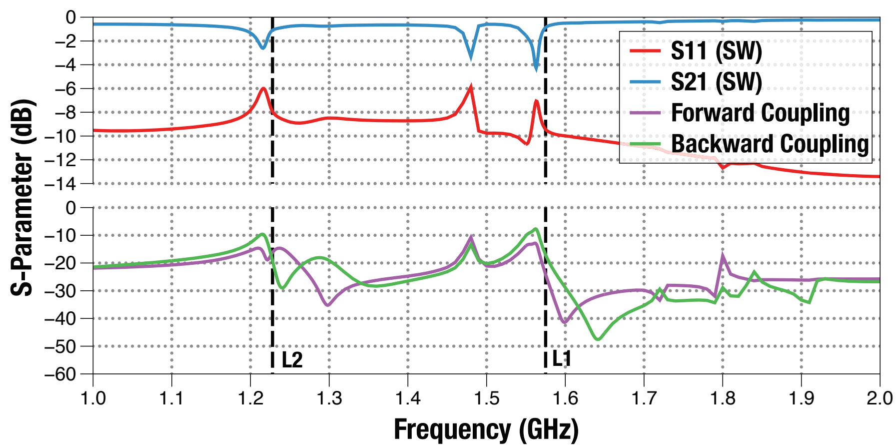

Figure 4.4: Transmission simulation results of three trapezoidal EBG unit cells with lumped loading components, showing both the SW (Upper PPW) mode scattering parameters, and coupling with the lower PPW mode.

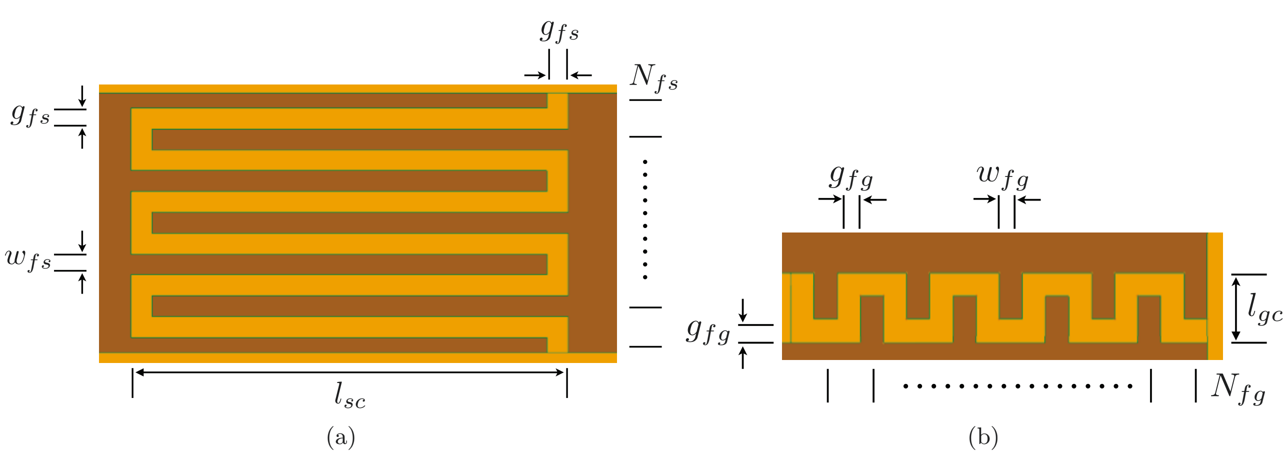

Figure 4.5: Layout of the interdigitated capacitors of a) the CPW strip line, b) the CPW grounds.

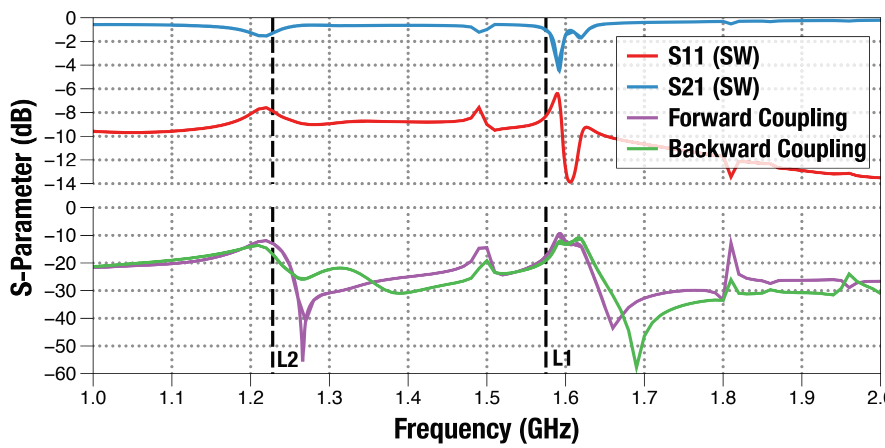

Figure 4.6: Transmission simulation results of three trapezoidal EBG unit cells with distributed loading components, showing both the SW (Upper PPW) mode scattering parameters, and coupling with the lower PPW mode.

the resonances do not appear exactly at the L1 and L2 frequencies. The are two main reasons for this difference. The first is that the resonant dips (especially around L1) potentially correspond to *Fabry-Perot* (FP) resonances, for which there is an integer multiple of 180^o incurred over the three unit cells. Such resonances have been found to be associated with strong reflection of the SW mode, and provide a higher level of rejection over a very small bandwidth than the bandgaps do. Unfortunately, because the even Bloch modes possess essentially flat dispersion properties in the vicinity of these bandgaps, the FP conditions occur at frequencies very close to those of the bandgap. This superposition makes it extremely difficult to discern which frequencies correspond to the bandgap regions and which correspond to FP resonances. Furthermore, since these FP resonances tend to scatter fields very well, they do not tend to contribute positively to desired radiation pattern shaping. The frequencies at which they occur are also dependent on the total number of unit cells employed, such that they are not predictable based on dispersive properties alone. Therefore, while it may appear that some off-band frequencies possess better rejection, those frequencies are not associated with desired properties of the antenna ground plane. The second reason is the propagation along the angle θ (as defined in the two-dimensional radial model), which is is not modelled in the transmission simulation. While it was was previously shown to have a small effect on the dispersive properties of the SW or lower PPW modes, the effect still may result in the shift of these resonances by a few MHz.

The resulting unit cell was simulated in an eigenmode simulation, and compared to the equivalent-circuit model in Fig 4.7. The result is very similar to Fig. 4.2, as expected, and used equivalent-circuit model loading components of values $L = 2.2nH$, $C_s = 2.8pF$, $C_g = 0.9pF$. The bandgaps are not quite centered on GPS L1 and L2, most likely due to the fact that this is a rectangular approximation of the trapezoidal unit cell. As well, the divergence of the equivalent-circuit model and the eigenmode data around 1.2 GHz and towards the X-point is attributed to the length of the CPW strip line's interdigi-

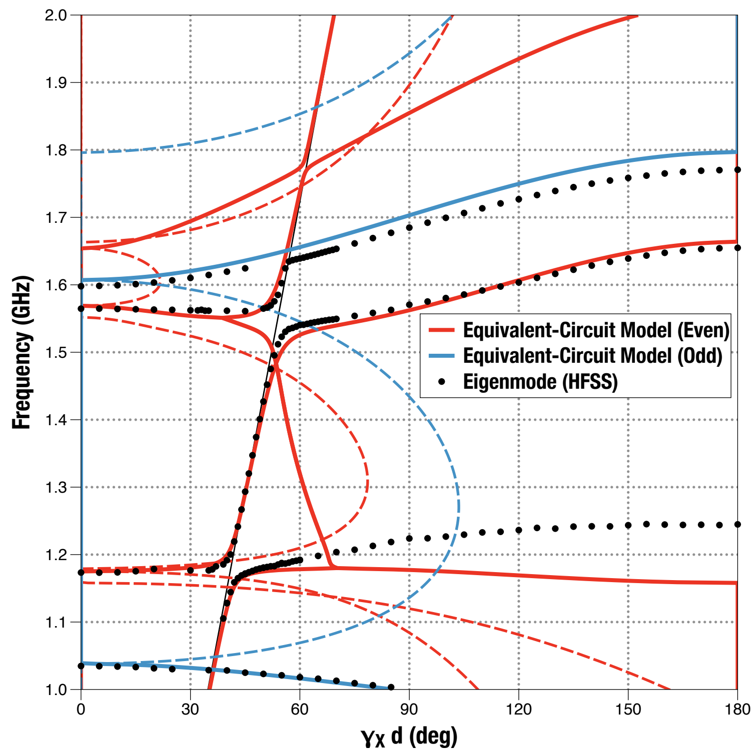

Figure 4.7: Dispersions of the final printed unit cell and the equivalent-circuit model.

tated capacitor, which is most likely approaching its self-resonance (is moderately inductive). This is not taken into account by the equivalent-circuit model, and could be remedied by shortening the length of the capacitor and instead making it wider than the strip it is embedded in.

4.3.4 Antenna Ground Plane

This EBG unit cell was then arranged circularly as previously described, and as shown in Fig. 4.8. An inner ground plane diameter of c = 100mm and outer diameter of e = 274mm were used in order to provide sufficient space for the GPS antenna element(s) – the ground plane was designed to be used with any kind of antenna which requires a conductor backing. This criterion also specifies that the starting width of the innermost unit cell is roughly 10.5mm, as previously given in the trapezoidal transmission simulation with an arc length of 12^o. The end width of the outermost unit cell is then roughly 28.8mm. The arc length leads to 30 unit cells around the antenna along the θ axis.

With the period of the unit cell being 29mm, the total radius of the antenna system is 137mm. The entire conductor-backed EBG structure and the inner ground plane was then fabricated on a single slab of 50-mil RO-3010 dielectric using a standard PCB process. The antenna element, a prototype GPS L1 and L2 patch antenna kindly provided by NovAtel Inc. [127], is not shown in order to protect their currently

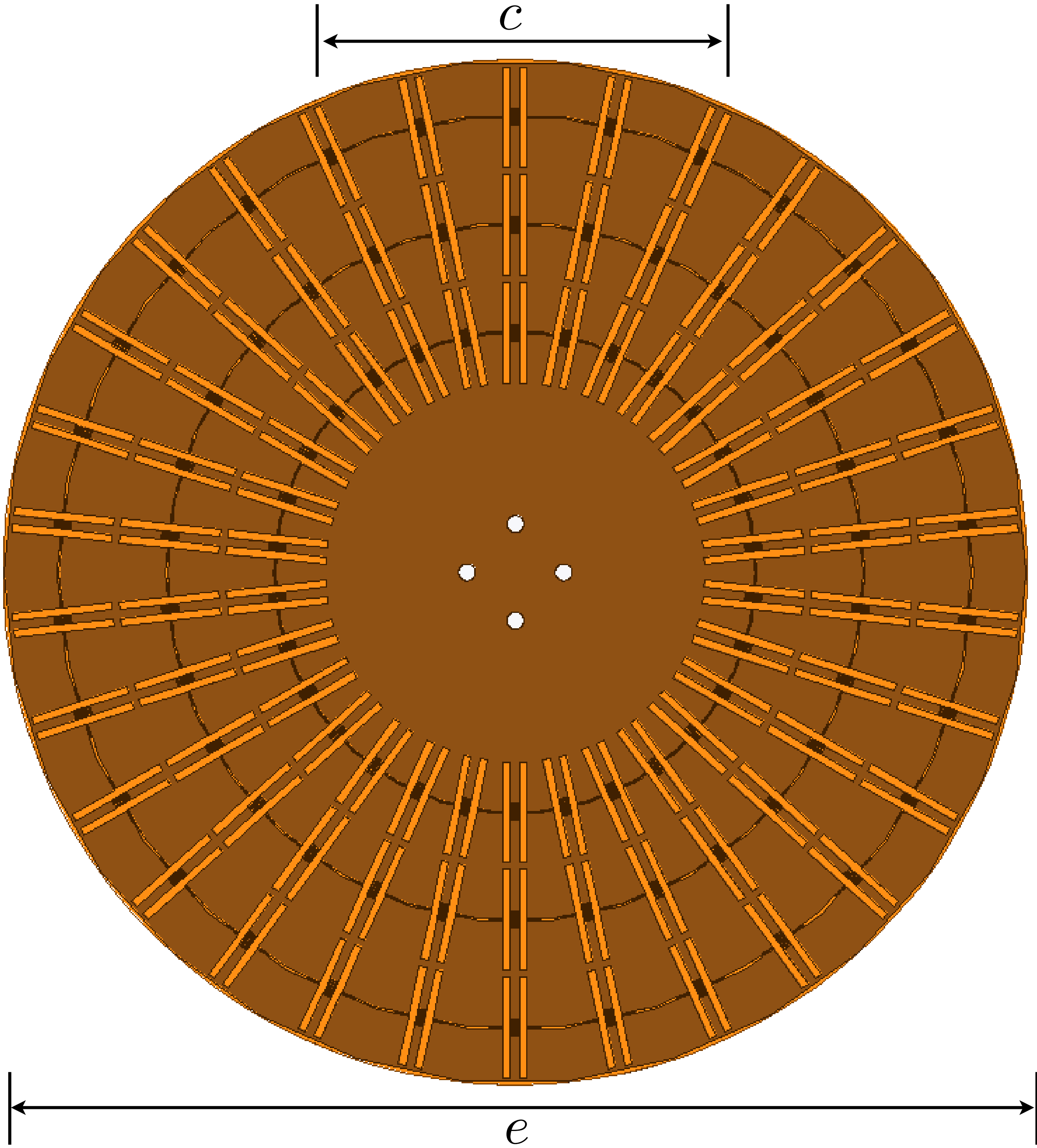

Figure 4.8: Layout of the fully printed GPS antenna ground plane, with circularly arranged EBG. The antenna element (not shown) is fed via the four holes drilled through the ground plane from the back side.

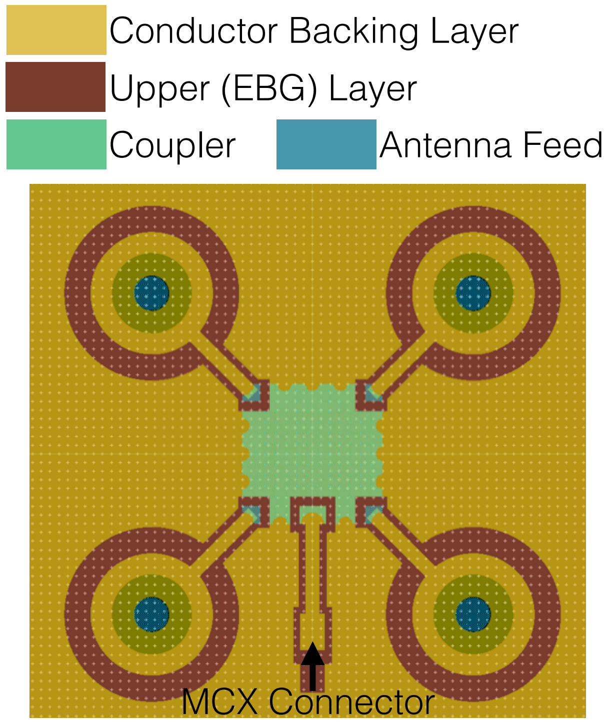

Figure 4.9: Layout of backside of the GPS antenna, with the location of the MCX connector labelled and the four-port coupler shown. The outputs of the couplers are routed to the antenna through the antenna feed lines.

unprotected intellectual property. However, it is sufficient to say that it is excited by four coaxial feed lines – hence the four holes in the center of the ground plane. These four coaxial feeding pins are in turn excited by a four-port 90^o degree coupler (RQF1200Q06), which in turn is fed via an MCX connector attached to the conductor backing of the PCB, as shown in Fig. 4.9.

4.4 Simulation

4.4.1 General Setup

In order to simulate the antenna element with the ground plane (hereon referred to as the *antenna system*), lumped ports with a 50Ω impedance were placed on each of the four coaxial feeding pins on the back side of the dielectric. Each of the ports were excited with equal 1 Watt magnitudes and $\pm 90^o$ out of phase with the neighboring ports, such that the antenna would radiate with a right-handed circular polarization.

The simulation domain was bounded by a cylindrical radiation boundary as shown in Fig. 4.10. The boundary has a radius of 213mm, and a height of 150 mm. There is a vertical space of 76mm between the top of the EBG surface and the top of the radiation boundary.

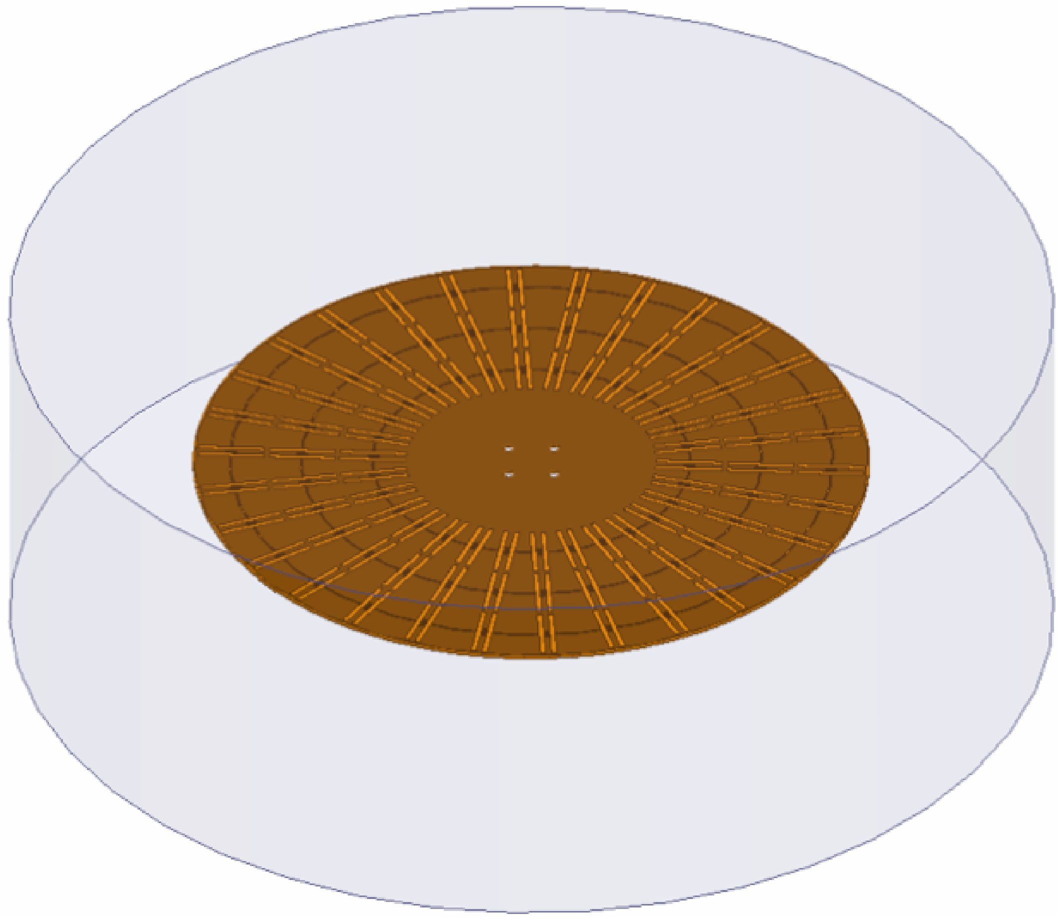

Figure 4.10: Layout of the antenna system with radiation boundary.

This setup was used in all of the following simulations. The data looked for in each simulation is the RHCP and LHCP realized gains, AR and MPR.

The results are plotted in polar-log form, using a standard spherical coordinate system, where θ is the elevation angle and ϕ is the angle around the azimuth.

4.4.2 Antenna Element

The performance of the NovAtel element was simulated independently as a base case for future comparisons. With a ground plane of 64mm radius, the data shown in Figs. 4.11a and 4.11b were obtained.

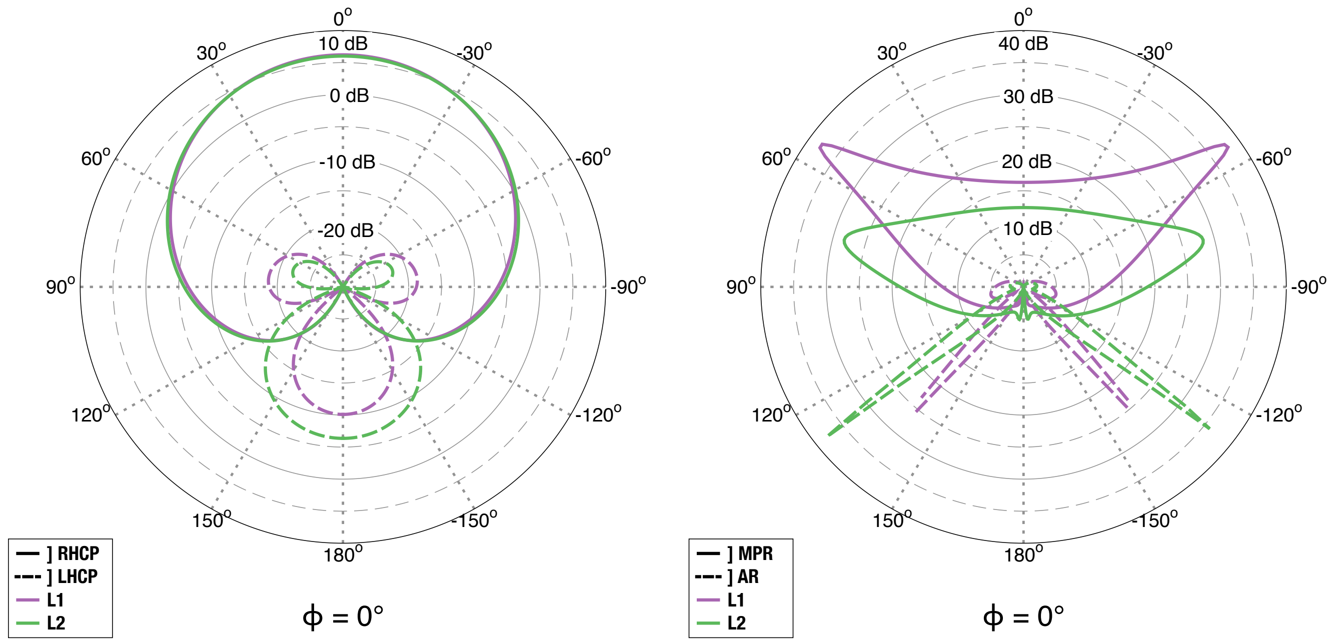

(a) (b)

Figure 4.11: Radiation properties of the unmodified NovAtel antenna at GPS L1 and L2: a) Realized Gains (RHCP and LHCP), b) MRP and AR.

4.4.3 Extended Bare Ground Plane

This is a well-performing antenna. However, detailed studies indicated that the performance of the antenna was strongly linked to the radius of the ground plane, as shown in Figs. 4.12a through 4.12d, in which ground plane radii of different values were studied – which is the case for many antennas which require a ground plane. Such situations occur when these antennas may be mounted on large metallic objects, such as the frame of a vehicle. The presence of the EBG should help to mitigate this effect, since it effectively masks the ground plane from the antenna element.

Next, an extended bare (unloaded) ground plane the same radius as the designed EBG ground plane was simulated, to serve as an adequate comparison for the effects of the EBG. The radiative properties of this design are shown in Figs. 4.13a and 4.13b, in which the general increase in LHCP and AR, and a decrease in MPR near the horizon is expected due to the large extent of the conductive ground plane.

4.4.4 EBG Ground Plane

Lastly, the antenna system with the EBG ground plane was simulated, and the results shown in Figs. 4.14a and 4.14b. This antenna shows greatly reduced LHCP above the horizon, and corresponds to an

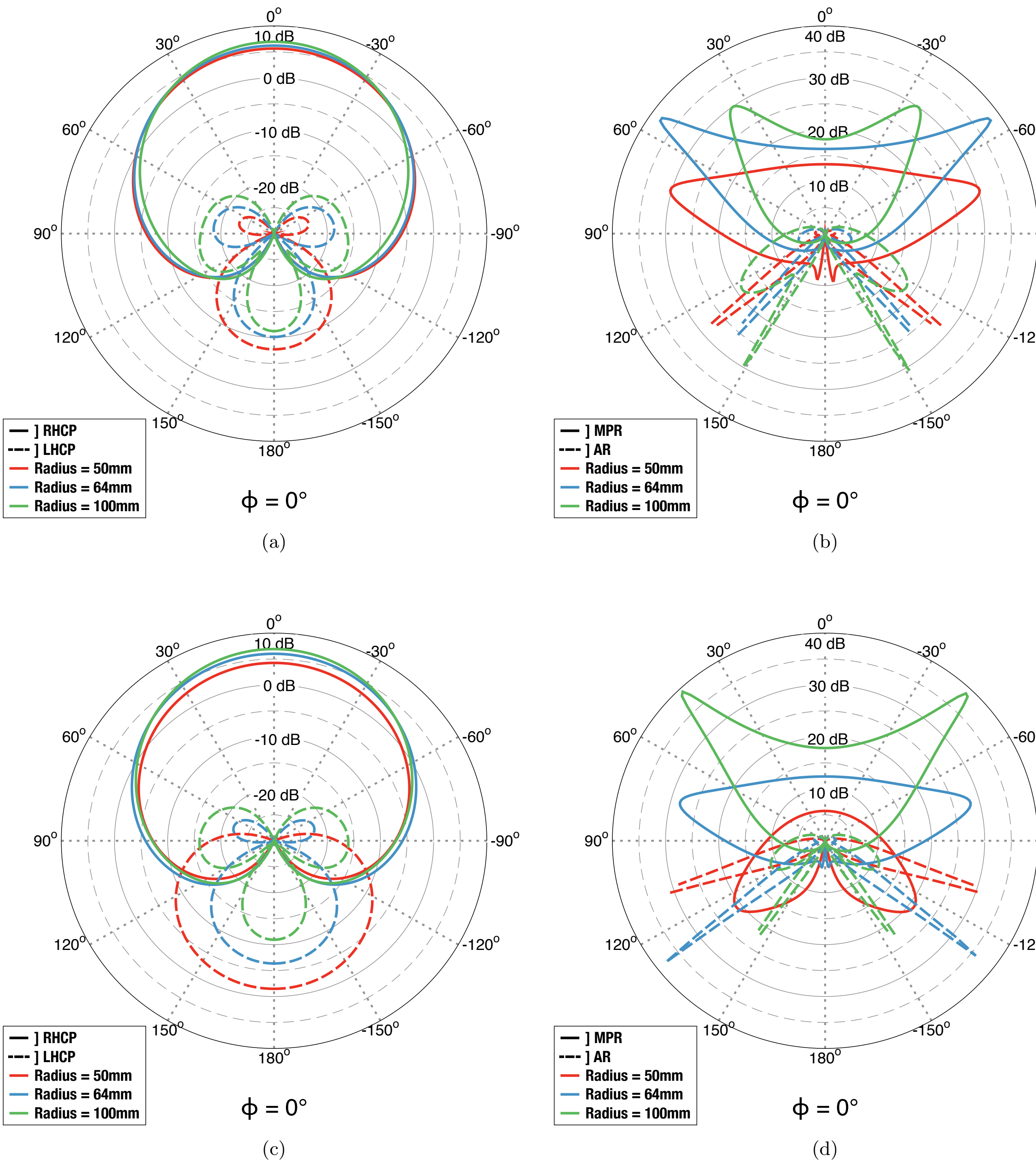

Figure 4.12: Radiative properties comparison of the NovAtel antenna with a swept ground plane radius (50mm, 64mm, and 100mm) at GPS L1 and L2: a) Realized Gains (RHCP and LHCP) at L1, b) MRP and AR at L1, c) Realized Gains (RHCP and LHCP) at L2, d) MRP and AR at L2.

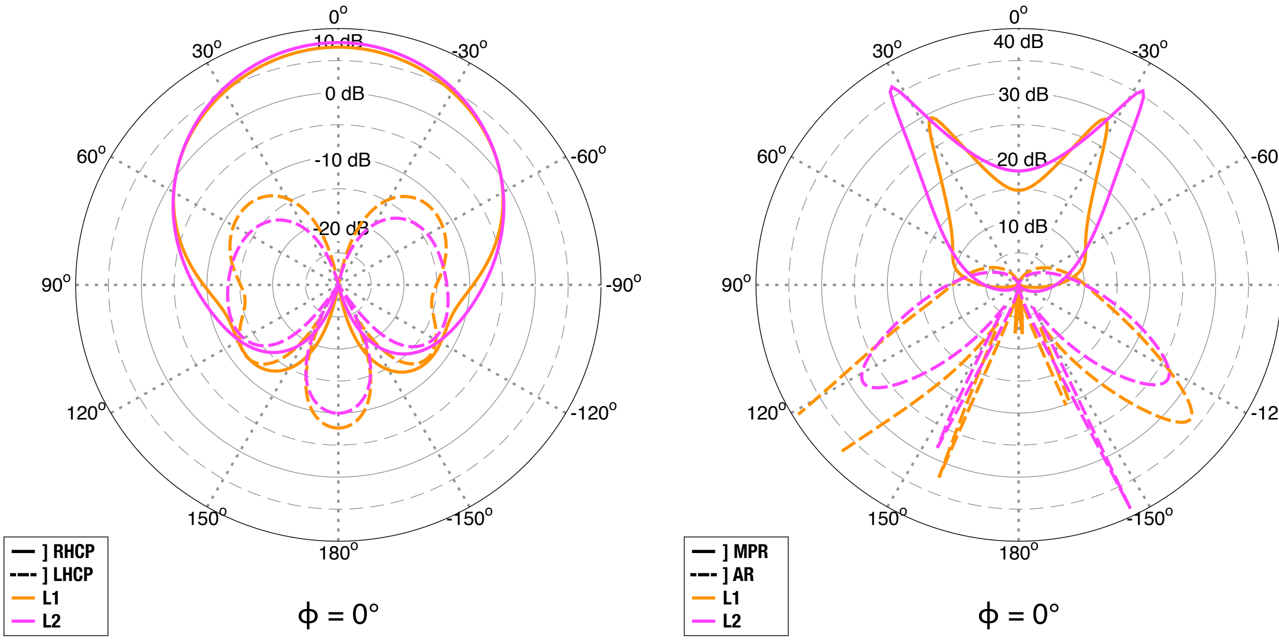

(a) (b)

Figure 4.13: Radiative properties of the antenna system with the bare (unloaded) ground plane at GPS L1 and L2: a) Realized Gains (RHCP and LHCP), b) MRP and AR.

increase in the MPR on and below the horizon. The AR on the horizon is also reduced to approximately 2 dB, which is an improvement over the original antenna. As expected, the RHCP is slightly reduced, but not to an excessive degree.

In an effort to determine the operational bandwidth of the antenna system, a frequency sweep around L1 and L2 was undertaken in which the realized gains of the system were determined in 10 MHz intervals from 1.550 GHz to 1.600 GHz, and 1.200 GHz to 1.250 GHz. These results, shown in Figs. 4.15a through 4.15d, are somewhat distorted due to the limited bandwidth of the antenna element, but it can be seen that best performance is observed near GPS L1 and L2 , with an acceptable performance bandwidth of roughly 20 MHz on either higher or lower side of these frequencies.

In order to examine the antenna's immunity to changes in ground plane size, the metallized substrate was extended to a 1m radius. This is considered an adequate approximation of a large conductor being placed under the antenna, such as the case of the antenna being mounted in the roof of a building. This was done for both the extended unloaded bare ground plane and the EBG ground plane, in which case the EBG was continued in all directions by the metallization. The results of these simulations are shown in Figs 4.16a through 4.16d. The L1 case shows a large reduction in overall gain and increase in axial ratio around the horizon without the EBG. The L2 performances are much more similar, although again the antenna system shows a higher axial ratio and larger LHCP around the horizon. These results indicate the the EBG continues to operate well in both cases, and can be used to mitigate the effects of large

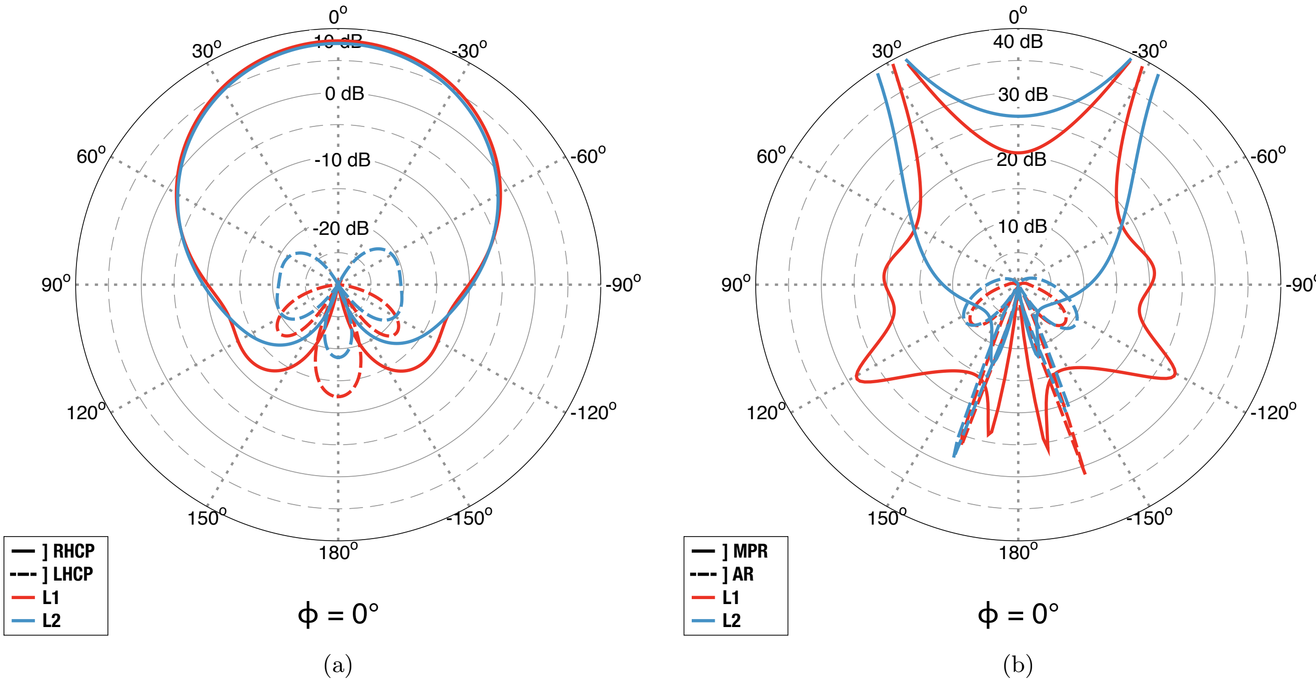

Figure 4.14: Radiative properties of the antenna system with the EBG ground plane at GPS L1 and L2: a) Realized Gains (RHCP and LHCP), b) MRP and AR.

metallic planes in close proximity the antenna.

The azimuthal symmetry was examined by plotting the radiative quantities around the azimuth at both $\theta = 90^o$ for all angles of ϕ. These results are plotted in Figs. 4.17a through 4.17b, and show a very small degree of variation (approximately 0.5 dB in the RHCP), as expected. This is a distinct advantage over EBGs with rectangular unit cells, for which the variation around the azimuth will typically be much larger [122].

4.4.5 Comparison of Results

Comparisons of the original antenna element, the system with a bare ground plane, and the system with the EBG ground plane, are shown in Figs. 4.18a through 4.18d. As expected, the antenna works extremely well at L1, with AR and MPR performance slightly better than the original antenna around the horizon. The L2 performance was not quite as ideal, but still shows much LHCP improvement over the bare ground plane case and a high MPR near broadside, indicating the correct operation of the EBG ground plane.

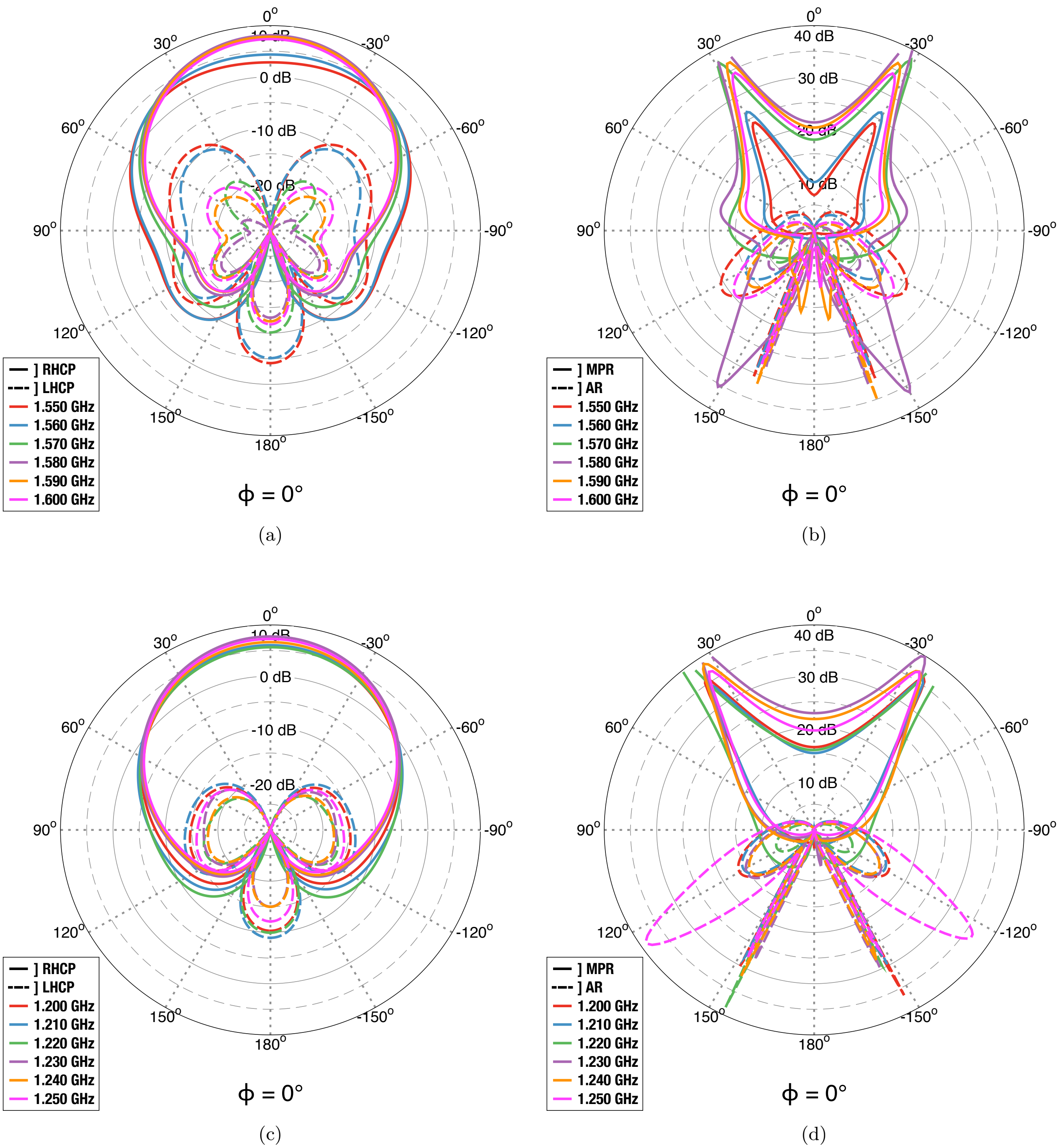

Figure 4.15: Radiative properties of the antenna system for frequencies around GPS L1 and L2: a) Realized Gains (RHCP and LHCP) around L1, b) MRP and AR around L1, c) Realized Gains (RHCP and LHCP) around L2, d) MRP and AR around L2.

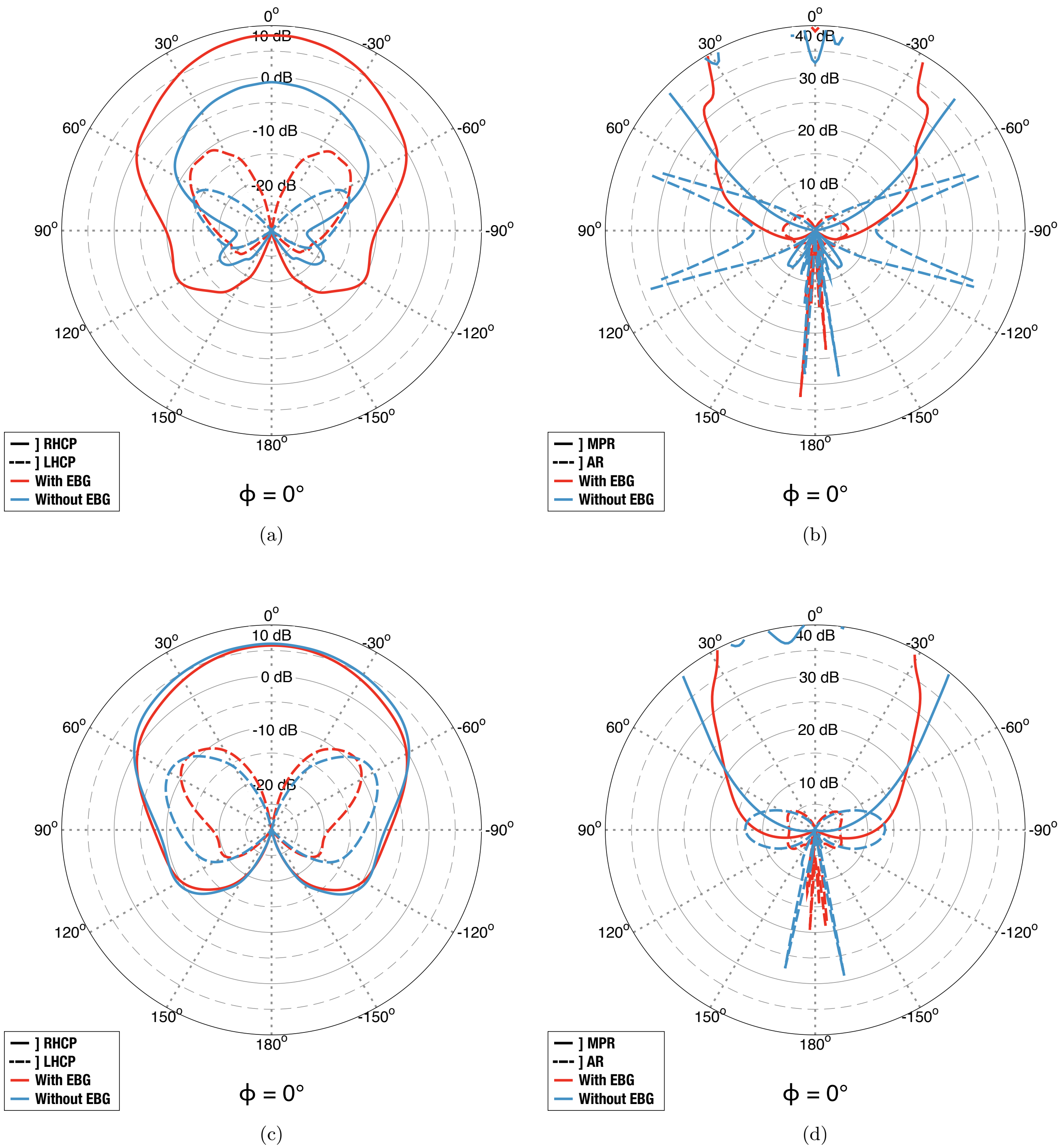

Figure 4.16: Radiative properties of the antenna system with an extended 1m radius ground plane, with and without the EBG at GPS L1 and L2: a) Realized Gains (RHCP and LHCP) at L1, b) MRP and AR at L1, c) Realized Gains (RHCP and LHCP) at L2, d) MRP and AR at L2.

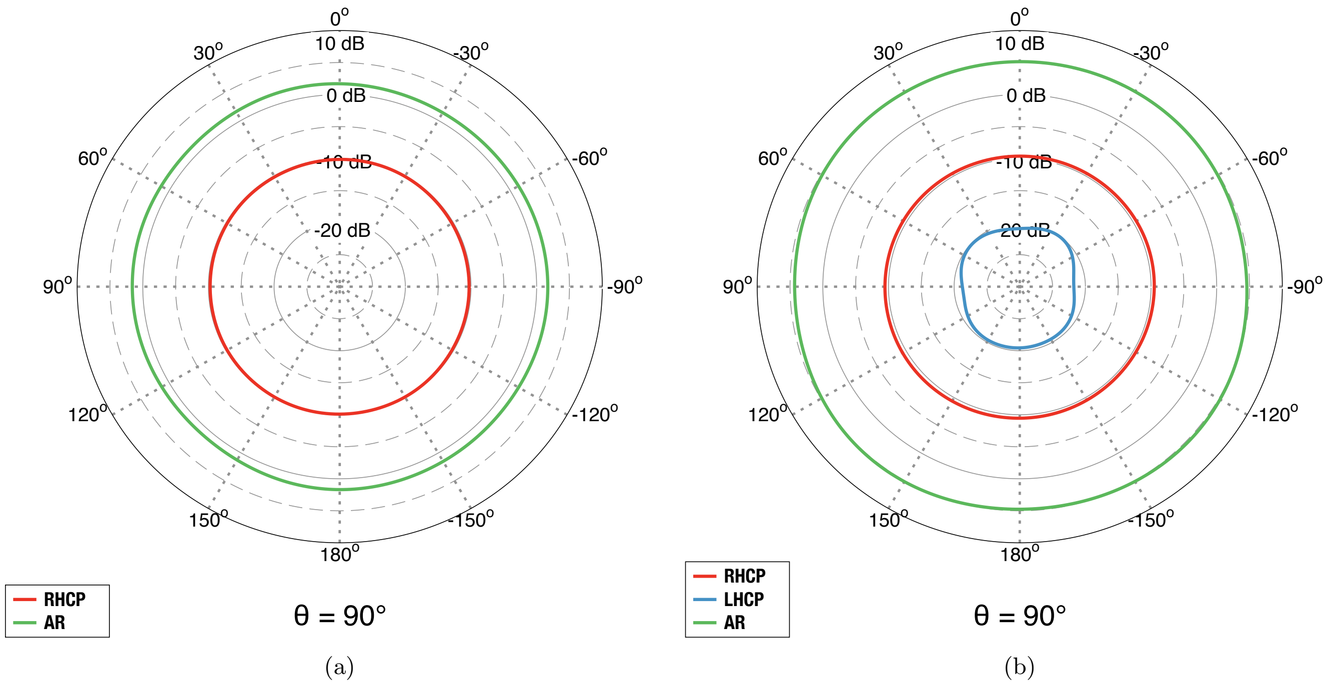

Figure 4.17: Realized gains and AR around the azimuth of the antenna system at an elevation of $\theta = 90^o$, for a) L1, b) L2. The LHCP at L1 is smaller than -30 dB.

4.5 Experiment

The complete antenna system with the EBG ground plane was fabricated and measured in an anechoic chamber, as shown in Figs. 4.19a through 4.19c. The scanning system employed was an NSI near-field measurement system with a complete spherical scan capability. The antenna EBGs were covered with a copper foil (after measuring the EBG properties) in order to approximate the bare ground case.

The results of this measurement are compared with the simulation results in Figs. 4.20a through 4.21d. It appears that similar to the PPW-mode EBG, the dielectric's permittivity was not exactly the simulated value of $\epsilon = 10.2$, but rather a lower value between 9.4 to 10. Unfortunately, this has caused the EBG to function improperly, rather than simply shifting the bandgap frequencies, since each isolated mode has a unique effective permittivity, and will be affected differently by shifts in the dielectric constant. It was found by performing a frequency sweep that best performance near L1 was achieved around 1.595 GHz, and therefore this value has been shown as well.

Unfortunately, it appears that the antenna element provided did not exactly match the simulated version, specifically in the LHCP at broadside. The simulation showed an LHCP null at $\theta = 0^o$, whereas the measured antenna possessed a maximum of -20dBi realized gain at L1 and approximately -12dBi at L2. Accounting for this, the case with the extended bare ground plane (no EBG) did match simulations

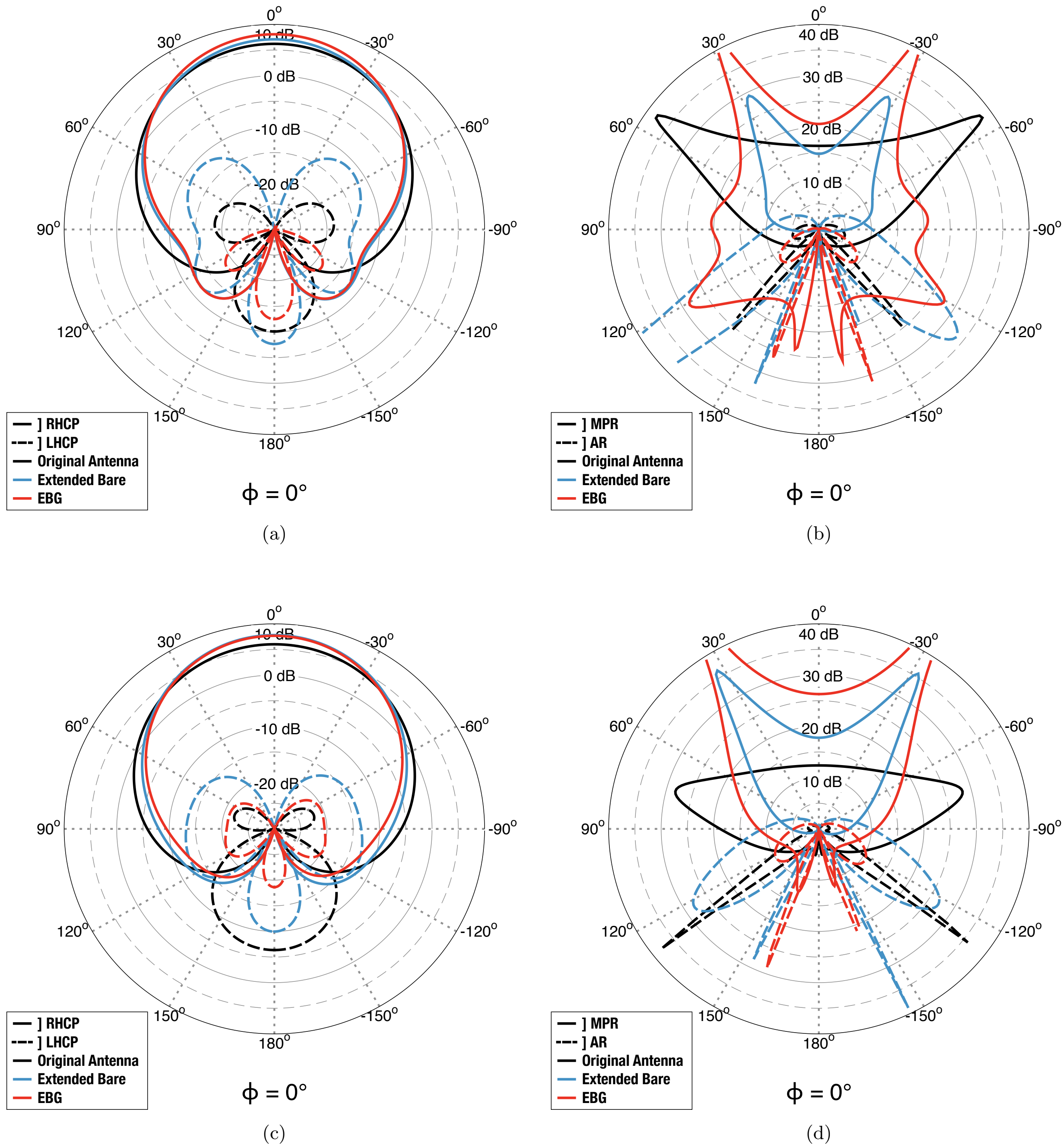

Figure 4.18: Radiative properties comparison of the original antenna, antenna system with bare extended ground plane, and antenna system with EBG ground plane at GPS L1 and L2: a) Realized Gains (RHCP and LHCP) at L1, b) MRP and AR at L1, c) Realized Gains (RHCP and LHCP) at L2, d) MRP and AR at L2.

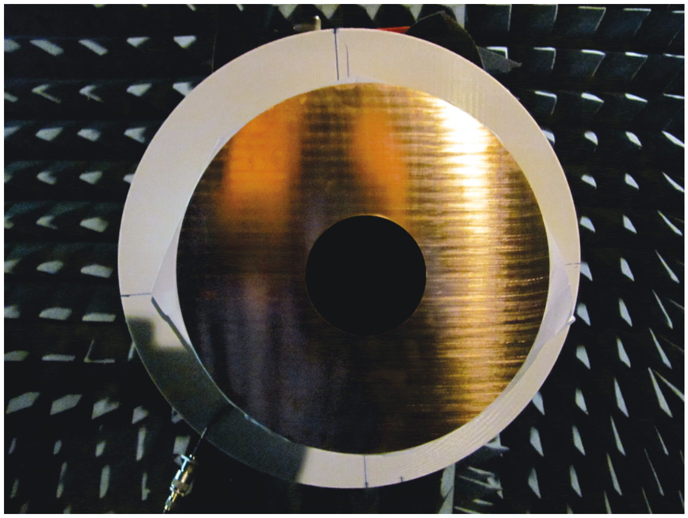

(a)

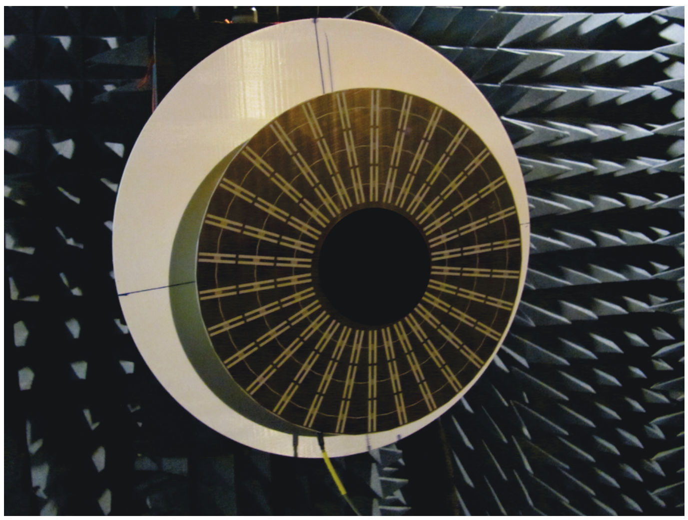

(b)

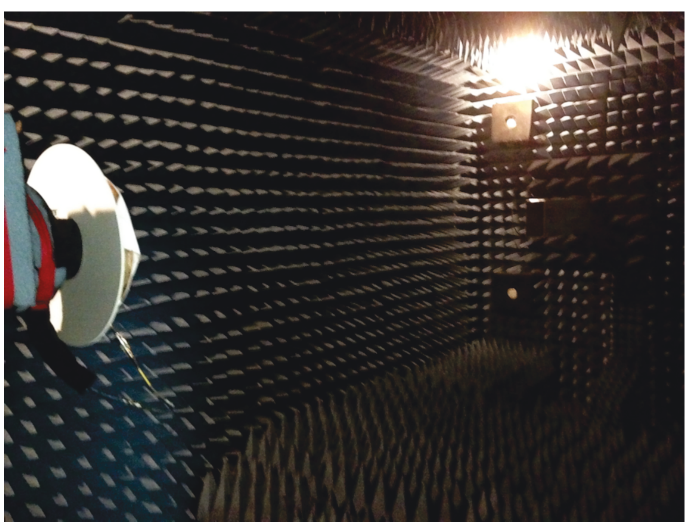

(c)

Figure 4.19: Photographs of the fabricated EBGs and anechoic chamber (antenna element censored), a) Without EBG (bare ground), b) With EBG, c) Chamber setup (antenna, left, and probe, right).

fairly well, although there is an observable drop in RHCP gain in the upper hemisphere of roughly 3 dBi. The simulations with the EBG, while not matching the simulations closely, do show both an observable increase in RHCP, and general decrease in LHCP. As previously indicated, the patterns at 1.595 GHz do show slightly favorable performance over those at 1.575 GHz, indicating a shift in the dielectric constant. Since the EBG's performance is not expected to scale directly with permittivity (due to the fact that each of the various modes possesses a different effective permittivity), the bandgap properties are most likely diminished. Additionally, the bandgaps are fairly narrowband in the optimized case, leaving open the possibility that the frequency sweep performed may not have found the optimal case.

The design could likely be improved by including a manufacturing scaling test. In such a test, the effective permittivity of a particular dielectric is evaluated through the inclusion of a microstrip line by which characteristic impedance or a resonance frequency could be measured. The manufacturer then scales the design appropriately. However, since as discussed the EBG is not expected to scale well, a more appropriate method may be to simply use a dielectric with a much smaller permittivity variance – however, this may be much more expensive, reducing one key feature of this ground plane design. A final option would be to use a dielectric with a lower effective permittivity. While this would necessarily result in unit cells with a larger period, it should also result in larger bandgap widths, reducing the effects of frequency shifts.

In summary, it appears that the novel EBG was successfully used to suppress the SW mode. Non-idealities in the realized devices, such as a dielectric constant shift, most likely contributed to a degradation of performance over the simulations, but the EBG still showed an improvement over a bare ground plane of the same size.

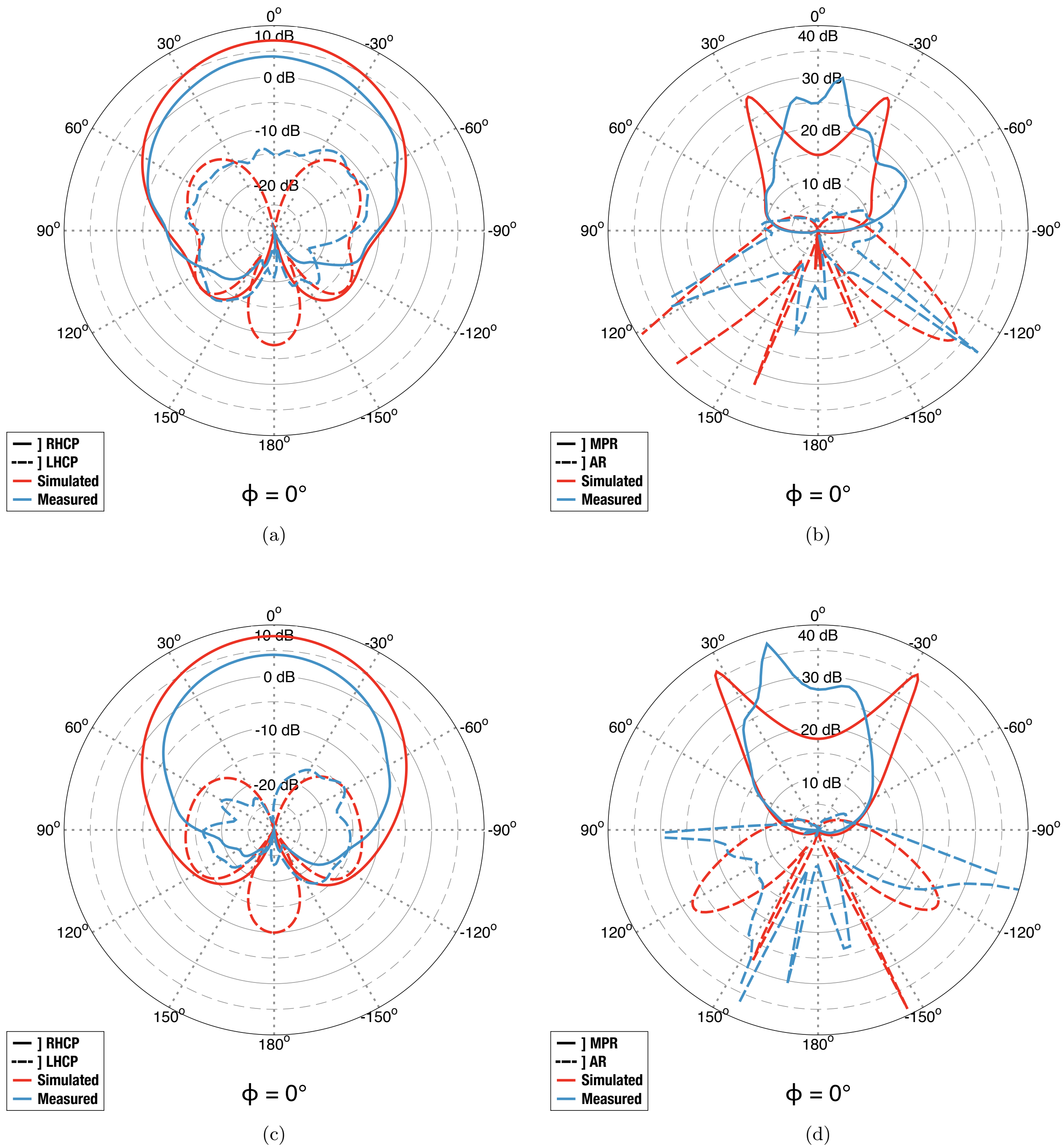

Figure 4.20: Radiative properties comparison of the simulated and measured antenna on a bare extended ground plane (no EBG case) at GPS L1 and L2: a) Realized Gains (RHCP and LHCP) at L1, b) MRP and AR at L1, c) Realized Gains (RHCP and LHCP) at L2, d) MRP and AR at L2.

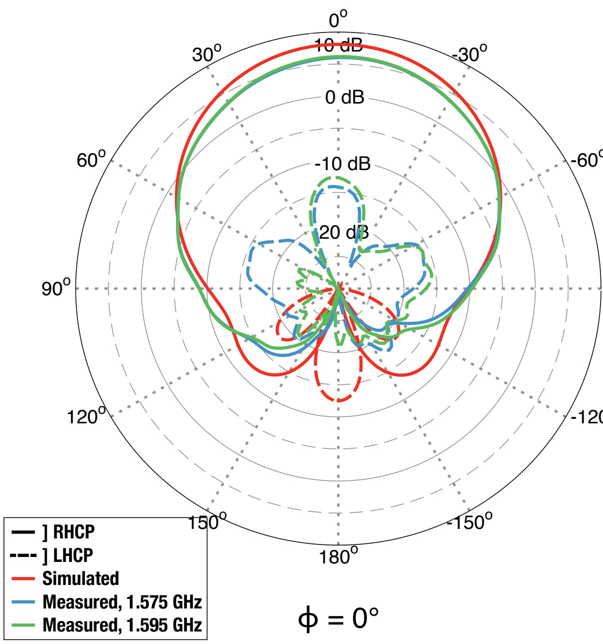

(a)

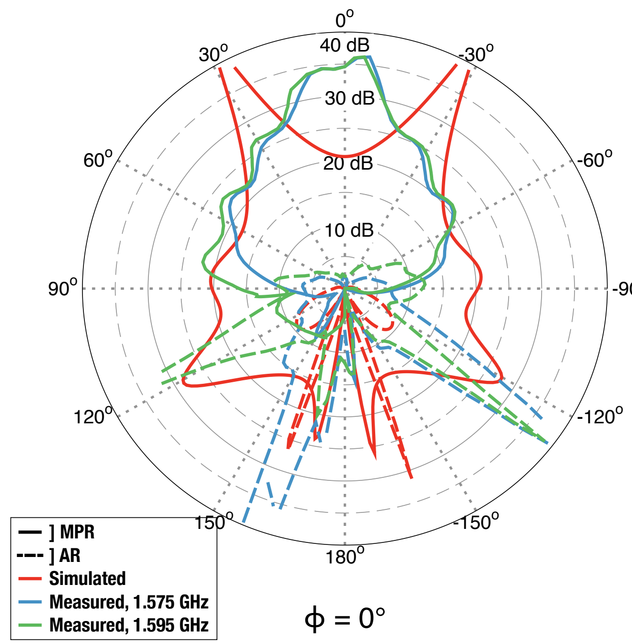

(b)

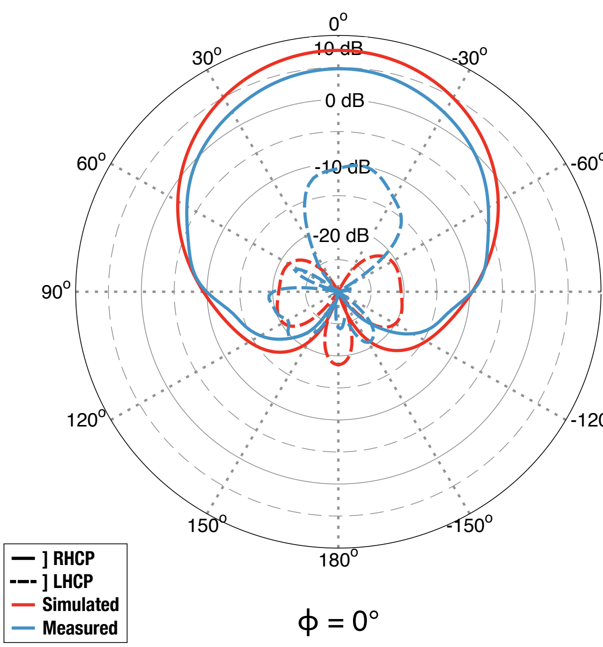

(c)

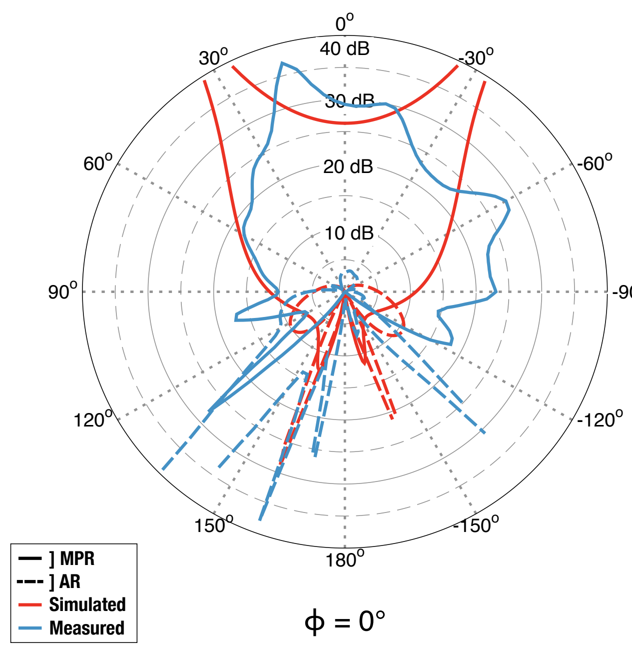

(d)

Figure 4.21: Radiative properties comparison of the simulated and measured antenna on the EBG ground plane around GPS L1 and L2: a) Realized Gains (RHCP and LHCP) at L1, b) MRP and AR at L1, c) Realized Gains (RHCP and LHCP) at L2, d) MRP and AR at L2.

Chapter 5

Conclusion

5.1 Summary

The theory of operation of a uniplanar, metamaterial-inspired EBG was developed with the use of MTL and dispersion analysis. It was shown that in general, complex-mode bandgaps arise as a result of coupling between various modes, and only those modes which couple experience bandgap behavior. Specifically, a CPW mode was loaded with TL-MTM techniques to support a backward mode, and it was shown that this mode interacts with a PPW mode to form a complex-mode bandgap. While the fields in the CPW gaps are essentially orthogonal to those of the PPW mode, the fields supported by the larger CPW grounds are very similar to those of the PPW mode, enabling the modes to couple. The sole purpose of the CPW mode in this context is to allow the creation of a backward-wave mode with a uniplanar structure.

Unlike existing uniplanar structures for the suppression of PPW modes, the bandgap was shown be precisely tuneable to the desired frequency range by adjusting the unit cells' constituent parameters. It was shown that even though the unit cells are one-dimensional in nature, they can be radially arranged such that they can suppress the transmission of power around a point in two dimensions by slightly distorting the unit cells into a trapezoidal shape. This was confirmed by the simulation and experiment on the transmission properties between two vias embedded in a parallel-plate medium, in which the transmission was suppressed over roughly the expected frequency range in the X-band.

It was shown that the loosely-bound SW mode at L-band could be modelled as a vacuum-filled PPW with a sufficiently large height. Under this approximation, the CPW and lower PPW modes could also interact with the SW mode to form bandgaps. An EBG was designed to suppress the SW mode at GPS L1 and L2, and arranged to form a circular ground plane. Simulation of the ground plane and a corresponding dual-band antenna showed a large reduction in LHCP on and above the horizon at these frequencies, along with reduced axial ratio and improved multipath ratio, indicating the suppression of the SW mode.

The development of this miniaturized, uniplanar, printable structure enables the application of EBGs with finely controllable bandgaps to high-frequency and high-component-density systems, which may not have been possible with previously existing structures. The coupling of power between modes which can be modelled with a simple equivalent-circuit model and realized on a standard PCB creates the possibility for novel, miniaturized, microwave circuit components.

5.2 Future Work

The research undertaken to produce this work raises several distinct, relevant questions which may be investigated as part of future studies in this area:

- Optimization of SW coupling. While it was shown that an increase in loading inductance was detrimental to the performance of the SW bandgap, it was not investigated as to how the bandgap performance may be optimized. This process would most likely involve analytically solving the determinant expression of the MTL equivalent-circuit model of the unit cell, which being a quartic equation would not be a trivial task. Anther possible method would be to analyze the EBG structure as an anisotropic metamaterial, by which the effects of the material parameters of the SW coupling could be determined. Since TL-MTMs expressly link the TL parameters to these medium parameters, the resulting unit cell properties could be implicitly determined.

- The two-dimensional EBG introduced in this work is only appropriate for suppressing signals around a point, and only operates well when the angular component θ is small. A true two-dimensional EBG may be necessary in many practical situations. Such a unit cell could be created by the intersection of four one-dimensional unit cells, as was done to create the series- and shunt-node NRI-TL structures [128,129]. Initial observations of this result indicate that the intersection of four loaded CBCPW unit cells should appear to be the UC-EBG structure, in which the solid patch in the center of the unit cell is the intersection of shunt inductive strips, and the gaps between patches are series capacitors in the CPW grounds. This structure has already been used in the applications of SW and PPW mode suppression, indicating a similar functionality to the structure in this work. A rigorous analysis of this system as a TL-MTM should reveal methods by which the UC-EBG may be miniaturized for these applications, and more importantly, yield precise control of the bandgap regions – which has not yet been accomplished. Additionally, the suppression properties may be further understood, being only currently described in terms of an isolated LC resonance.

- The understanding of the fast-wave region was not explored in this work, although the equivalent-circuit model did agree well with the HFSS data in this region. Fast waves have applications to leaky-wave antennas, for which the radiation angle can be well controlled, but alternatively the reciprocal device, which is an absorbing surface. These applications are not new, but this work does suggest some extensions. Firstly, the presence of the CSL mode, with an orthogonal polarization to the CPW mode, could be designed to have the same dispersive properties as the CPW mode. This would allow for devices such as circularly polarized leaky-wave antennas. Secondly, the application of a two-dimensional structure should allow for two-dimensional devices, such as planar, circularly polarized leaky-wave antennas for applications such as GPS, or reciprocally, planar, polarization independent absorbers which operate over a large range of incident angles. Thirdly, detailed knowledge of the coupling of power inside the unit cells should allow a study of methods to increase operating bandwidth and radiation/absorption magnitudes (which are currently not well understood), leading to more effective, compact fast-wave devices.

Appendix A

Verifying the Definition of the Bandgap

In order to verify that the definition of a bandgap encompasses the coupling of a forward mode with both a backward mode and a forward mode, a forward mode was designed to interact with another forward mode in order to create the type of bandgap that is unique to this work. This bandgap does not have complex mode region, nor is it associated with a real (attenuating) propagation component, but rather it operates by redirecting power into its various constituent modes. If this behavior causes suppression of either of the modes, then the definition will be validated.

The forward mode used was simply a shielded PPW loaded with series capacitors. This design was chosen due to the fact that it is produces a well-known dispersion which has a non-zero Γ-point and which, for the cases in which the lower PPW is filled with a dielectric with an ϵ larger than that of air, crosses the vacuum light-line. The designed unit-cell, shown in Fig. A.2, has a period d of 25mm, width w of 10mm, and a slit width g of 0.2mm, which has been loaded with a capacitor with value C of 1pF. The lower dielectric has a thickness of 1.524mm, ϵ of 4.4, while the upper dielectric has a height of 20mm (in order to emphasize the coupling region) and an ϵ of 1.0. The trace thickness is $35\mu m$. The unit cell has PMCs on the transverse boundaries and PBCs on the longitudinal boundaries. The equivalent-circuit model of this setup is shown in Fig. A.1.

The resulting dispersion shown in Fig. A.3 reveals a bandgap around 1.5 GHz, according to both the equivalent-circuit model and the eigenmode simulation, which are in good agreement. In order to confirm

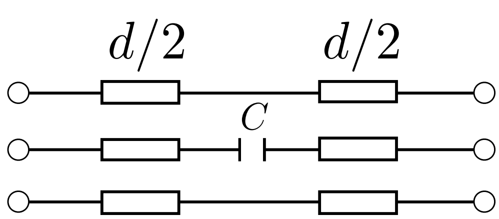

Figure A.1: Equivalent-circuit model for modelling the bandgap formed between the coupling of two forward modes.

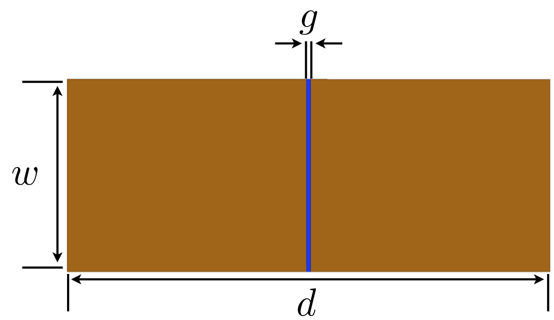

Figure A.2: Simulated setup of a shielded capacitively-loaded PPW unit cell.

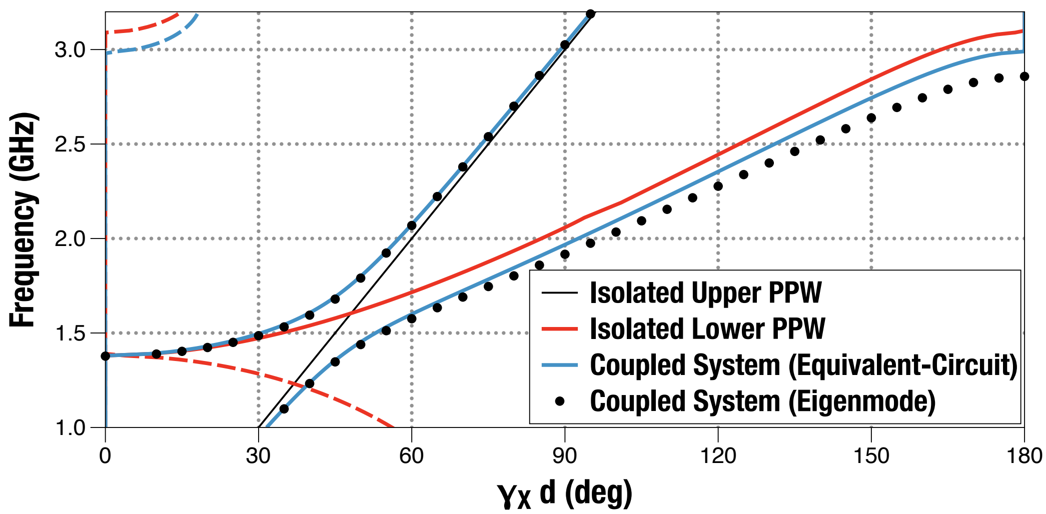

Figure A.3: Dispersion diagram for the coupling of two forward modes, showing the isolated (red) and coupled (blue) dispersions from the equivalent-circuit model, as well as the HFSS data (black dotted).

that this bandgap does indeed suppress the upper PPW mode, a transmission simulation was conducted in which the scattering of both PPW modes were observed. These data are shown in Fig. A.4, and there is clearly suppression of the PPW modes around 1.5 GHz. Additionally, there is an increase in the coupling between the upper and lower PPW modes in the forward direction, as expected from the dispersion. Coincidentally, there is a reduction in coupling between the upper and lower PPW modes in the backward direction, whereas these forward and backward coupling parameters are nearly identical everywhere outside of the expected bandgap. This clearly defines a region in which power prefers to couple forward, as expected from the dispersive properties.

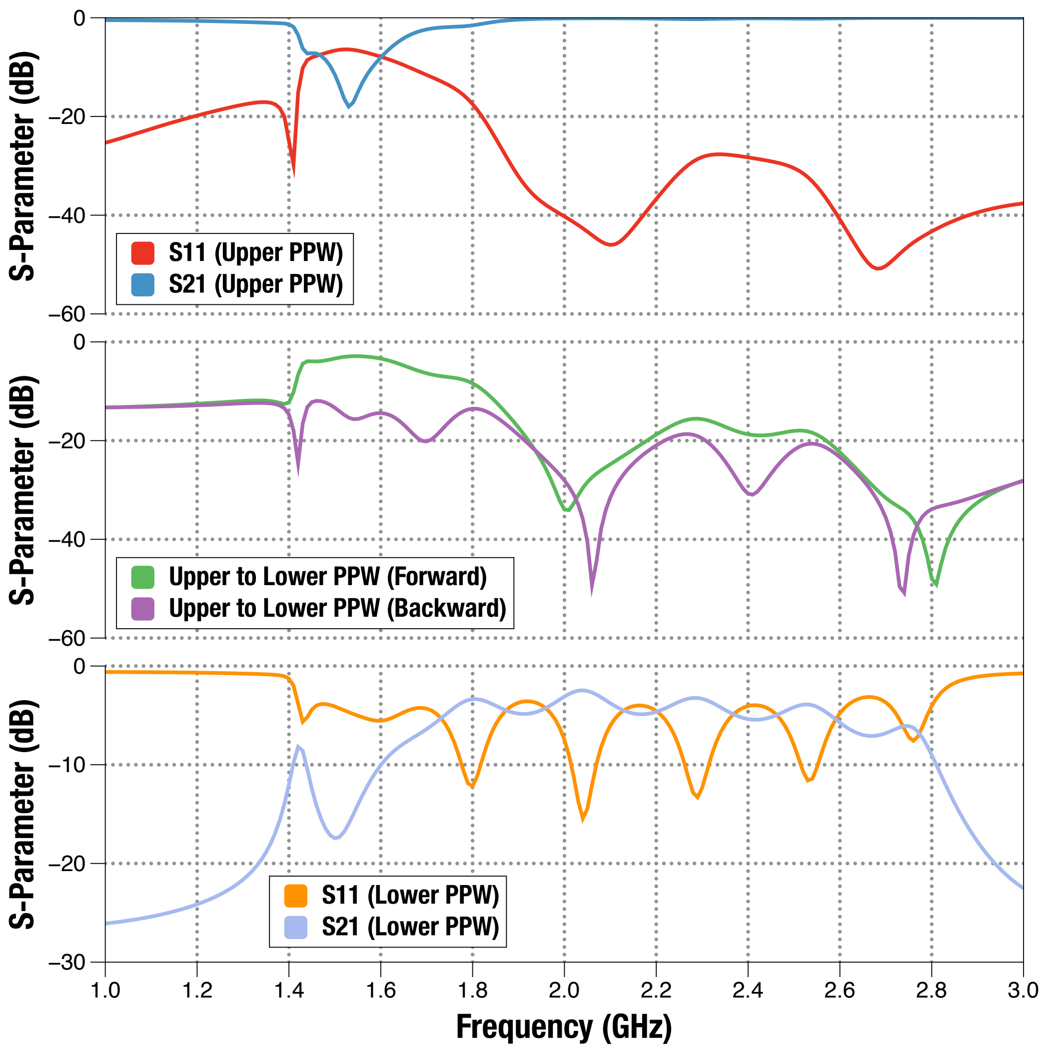

Figure A.4: Simulated scattering parameters of a shielded capacitively-loaded PPW unit cell. The isolated modes are suppressed around 1.5 GHz, where there is strong evidence of coupling between modes in the FW direction.

Appendix B

Traditional SW EBG Characterization

Once the dispersion characteristics of a SW-suppressing EBG is known, it is typically validated using one or more characterization methods. A few of the popular methods are the *incident plane wave test* [10,130], the *microstrip test* [131, 132], and the *antenna transmission test* [5, 20], which are used extensively in the EBG literature. Unfortunately, the first two methods suffer from large deficiencies in the accuracy of their results, while the third is only useful for a particular setup. Therefore, they will not be used in this work. This section will briefly overview the reasoning behind this decision.

B.1 Incident Plane Wave Test

The incident plane wave test is carried out by examining the reflection properties (magnitude and phase) of a plane wave incident on an infinite array of unit cells. As explained in [10], the case of a zero degree reflection corresponds to the behavior of an AMC, which does not support SW mode. Unfortunately, a large approximation was made in this analysis. Specifically, it was assumed that the phase incurred by the SW over the length of the unit cell is negligible. Unfortunately, this is typically not the case for unit cells on the order of $\lambda_g/4$. The point that is examined by this test is the Γ-point, at normal incidence, and due to the nature of the incident plane wave, all other oblique angles correspond to the fast-wave region of the dispersion diagram for similarly polarized modes, as explained in [133] (the incident plane wave can be viewed as the reciprocal of a leaky-wave antenna). Although the zero degree reflection phase at high angles of incidence will approach the upper edge of the SW bandgap, as shown in Figs. B.1 and B.2, the normal incidence test is incapable of finding the slow-wave side of the SW bandgap, and is therefore unusable for determining SW bandgap width or center frequency for modes with appreciable slope.

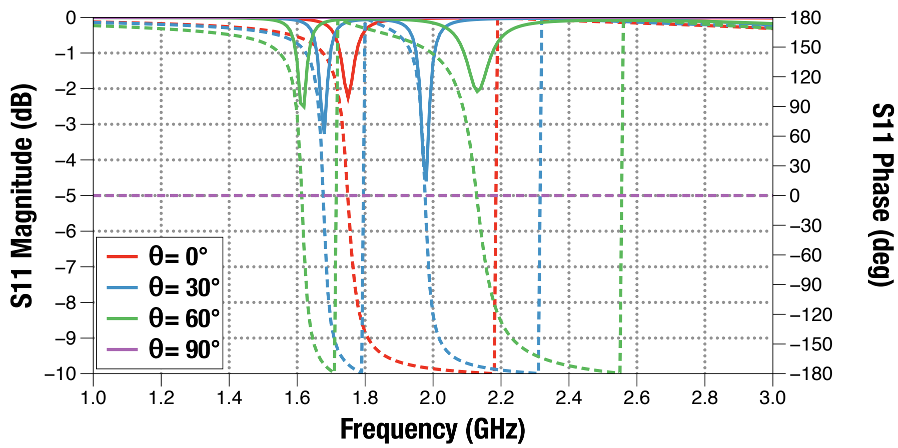

Figure B.1: Magnitude and phase of plane wave reflection for various angles of incidence.

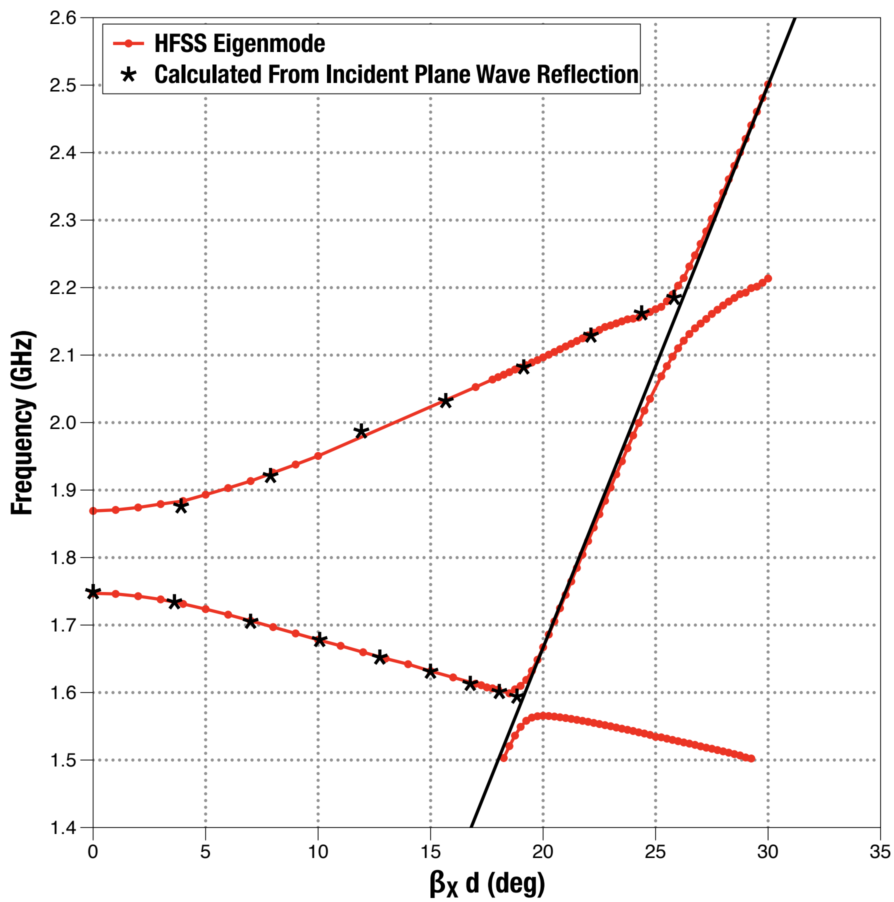

Figure B.2: Dispersion diagram containing calculated dispersion from zero degree reflection frequencies (from angle of incidence in steps of 10^o) and eigenmode solutions.

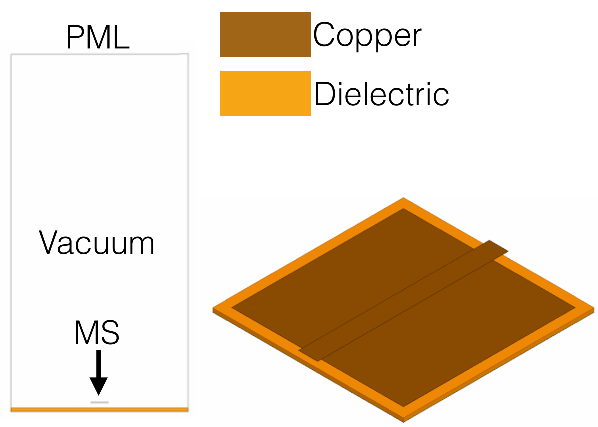

Figure B.3: Layout of the Sievenpiper mushroom structure with suspended microstrip eigenmode simulation.

B.2 Microstrip Test

The microstrip test involves suspending a microstrip line above an EBG surface, exciting a microstrip (MS) mode, and observing the scattering of this mode. It is generally understood that the scattering parameters of the MS mode should be very similar to those of a SW mode, since both contain strong vertical electric fields.

There are several issues with this interpretation. Firstly, there is strong coupling between the MS and the EBG, resulting in a mode whose fields are strongly confined between them. As previously shown with the variable shield height, this confinement of fields can result in a greatly increased bandgap region. Secondly, the fields around the microstrip line are not purely vertical – there can be significant horizontal electric field components around the edges of the microstrip line. This can result in undesired coupling and a deviation of results from those of a true SW mode.

The effects of the modal coupling between the microstrip mode and a Sievenpiper mushroom structure was investigated to determine the validity of this test. The Sievenpiper structure was created with the following properties: a period d of 50mm, a gap between patches of length 5mm, a via radius of 0.5mm, a dielectric height of 1mm, and a relative permittivity of 2. A microstrip was suspended in the air above the Sievenpiper unit cell's patch, centered tangentially on the via, at a height of 1.5mm, and with a width of 5mm. This setup is shown in Fig. B.3 for the eigenmode setup, which also employed PMC tangential boundary conditions and a PML on the upper boundary. The corresponding transmission simulation employs 9 unit cells and excites the MS mode, as shown in Fig. B.4. In order to avoid distorting the MS modal fields, the unit-cells were also cascaded tangentially, such that the simulation contained 5 unit cells on the transverse axis.

The dispersion results are shown in Fig. B.5, and compared to the case without the MS. As expected,

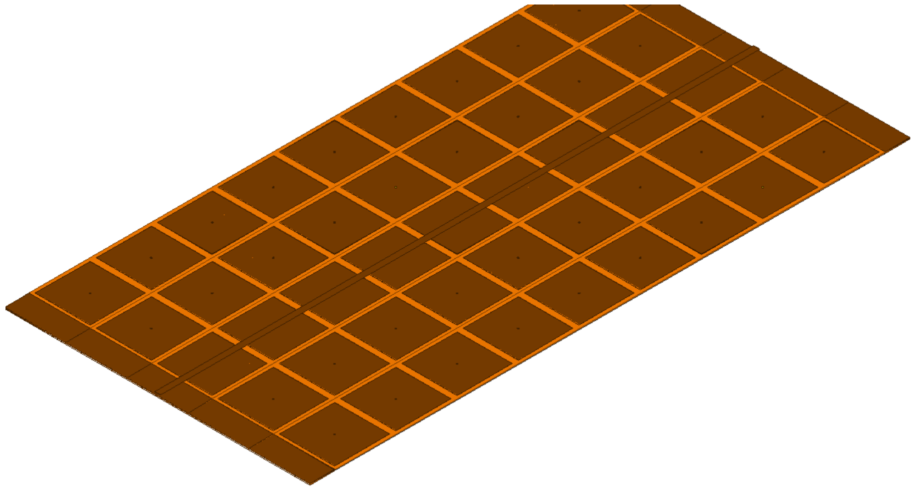

Figure B.4: Layout of the Sievenpiper mushroom structure with suspended microstrip transmission simulation over 9 unit cells.

the true SW bandgap exhibits much less coupling than with the MS mode. Similarly, the transmission results, shown, in Fig. B.6, show that the bandgap is nearly three times wider and exhibits a much higher level of suppression for the MS mode than for the SW mode. These results clearly indicate the inadequacy of the microstrip test for gauging SW suppression at low microwave frequencies, which only becomes more apparent as the unit cells being studied are miniaturized. Subsequently, it will not be used as an evaluation metric in this work.

B.3 Antenna Transmission Test

The antenna transmission test involves separating two antennas on a common substrate by a fixed distance. The transmission properties (S_{21} or S_{12}) between the two antennas are then evaluated with and without an EBG placed between the antennas. In the absence of near-field coupling, this test correctly determines the power carried between the antennas via surface-waves.

However, this test is generally only done when the frequency of operation is high, and/or the substrate is relatively thick, and/or the substrate has a high dielectric constant, whereas if this type of test is conducted in the L-Band (around 1.5 GHz), and on a regular 60-mil FR-4 substrate, the test does not yield very good results. The reason for this is the behavior of surface-waves on these substrates and in these frequency ranges. The SW mode is sensitive to these changes, because these will determine how "loosely" or how "tightly" bound the SW mode is on the substrate.

This "binding" effect is displayed in the following figures, which show the longitudinal field profiles of the SW mode on a grounded dielectric slab. The frequency of operation, dielectric height, and dielectric constant are varied, and the results are plotted in terms of normalized field magnitudes on a logarithmic

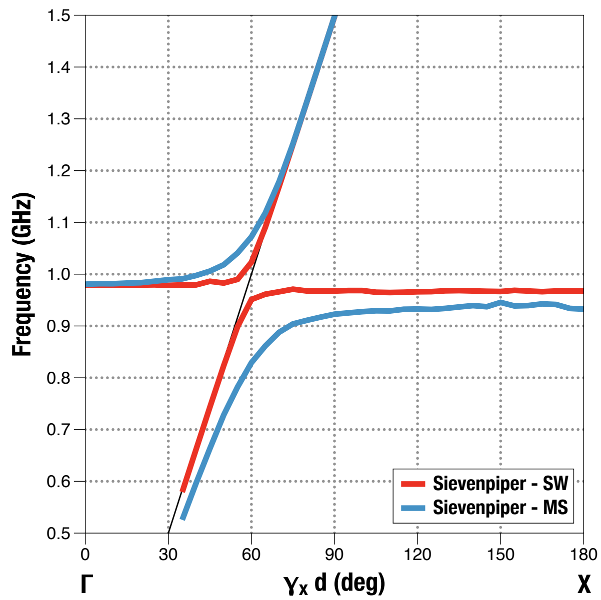

Figure B.5: Simulated dispersion of a Sievenpiper mushroom structure showing coupling with the SW mode (red) and the MS mode (blue).

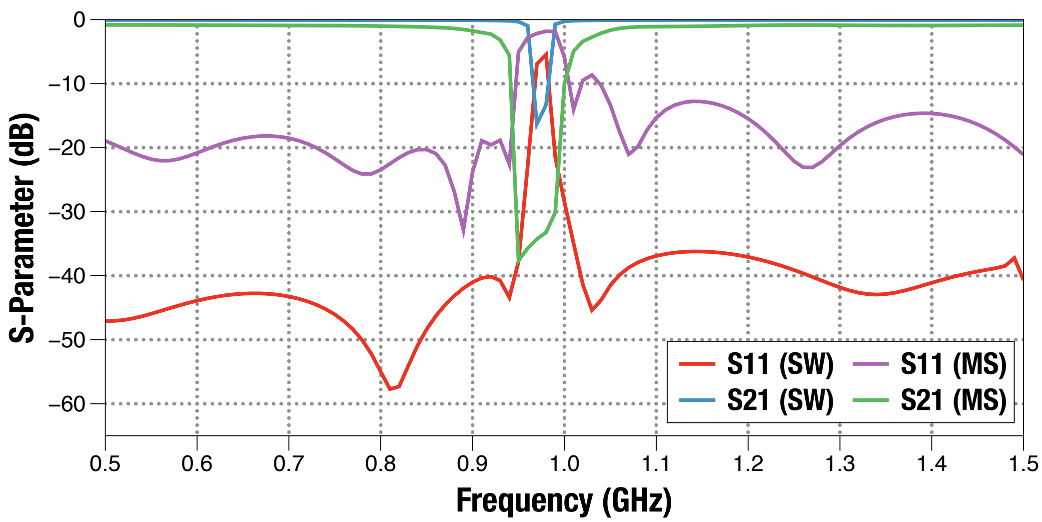

Figure B.6: Simulated transmission over nine Sievenpiper mushroom structures detailing the suppression of the SW mode (red and blue) MS mode (purple and green).

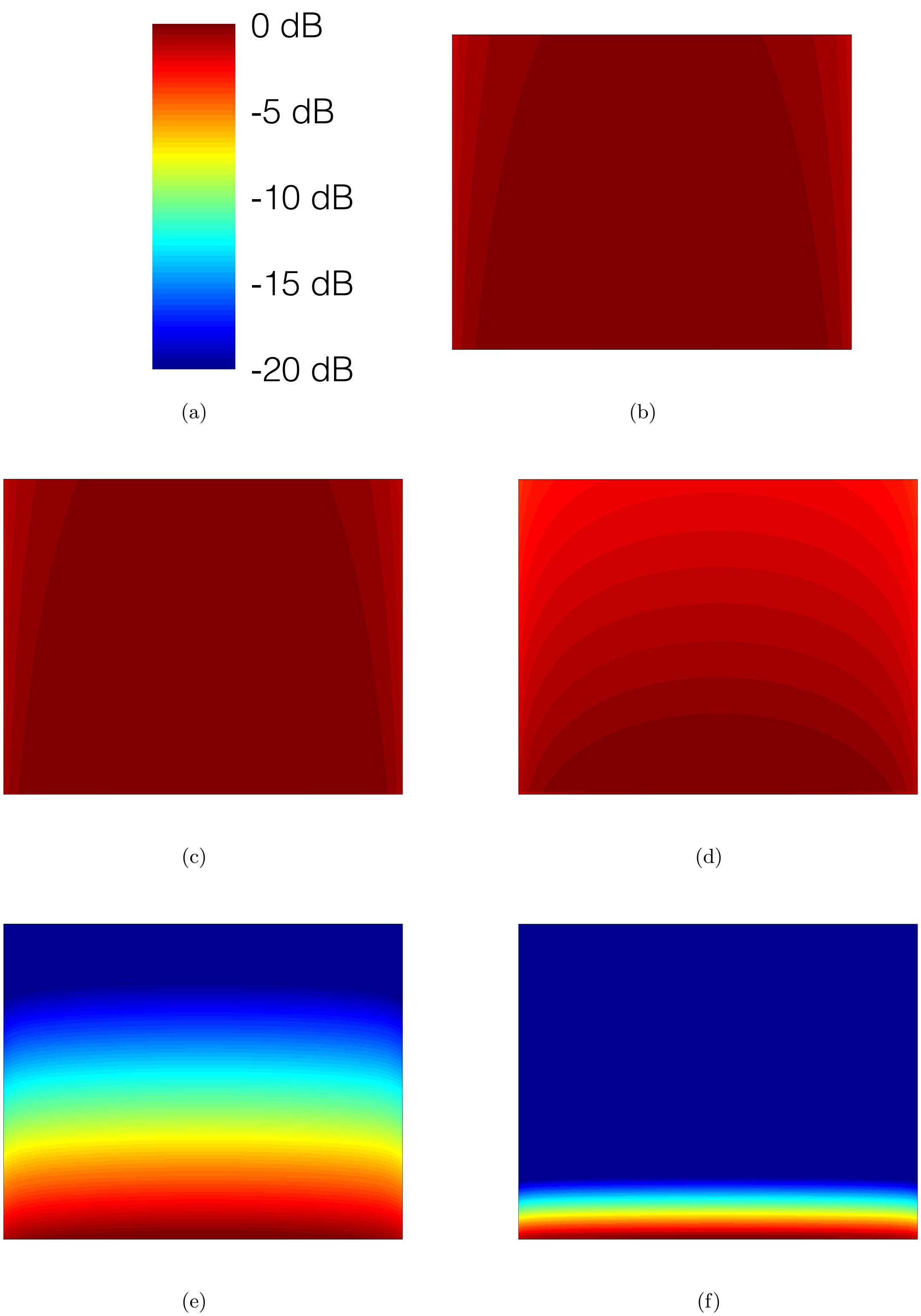

Figure B.7: Longitudinal field profiles of the SW mode on various grounded dielectric slabs: a) Color scale, b) $f = 1.5\ GHz$, $h = 60\ mils$, $\epsilon = 4.4$, c) $f = 1.5\ GHz$, $h = 60\ mils$, $\epsilon = 10.2$, d) $f = 1.5\ GHz$, $h = 300\ mils$, $\epsilon = 4.4$, e) $f = 10\ GHz$, $h = 60\ mils$, $\epsilon = 4.4$, f) $f = 10$, $h = 300\ mils$, $\epsilon = 10.2$.

scale. The "ground" is assumed to be a PEC located along the bottom boundary of each figure. The horizontal axis spans half a guided wavelength in all cases, and the vertical axis spans one meter (the aspect ratios are therefore incorrect, but have been modified for clarity). The scale for all of the figures is indicated in Fig. B.7a, and represents a normalized range from 0 to -20 dB.

The base case is shown in Fig. B.7b, for which the frequency of operation f is 1.5 GHz, the dielectric height h is 60 mil, and the relative dielectric constant ϵ is 4.4. This corresponds to a case for which the SW mode is extremely loosely bound, as indicated by the extremely small field variations. Fig. B.7c shows the field profile for a similar setup, but in which the dielectric constant is much higher at 10.2. There is almost no change from the base case, which is expected due to the extremely electrically thin dielectric. Fig. B.7d shows the field profile for which the dielectric constant is reverted to 4.4, but the dielectric height has been increased five times to 300 mils. In this case, the SW mode is more tightly bound to the surface by a noticeable degree. Fig. B.7e shows the field profile for the case in which the dielectric properties are the same as the base case, but the frequency has been increased to 10 GHz. As can be seen, the SW mode is tightly bound to the dielectric. Finally, all three augmentations were performed at the same time to yield Fig. B.7f, for which f is 10 GHz, the dielectric height h is 300 mil, and the relative dielectric constant ϵ is 10.2. In this setup, the SW mode is nearly completely contained within the dielectric and decays very quickly away from the dielectric-air interface.

As was demonstrated in this thesis, the degree of coupling between the upper PPW mode and the EBG's CPW or lower PPW mode was strongly influenced by the height of the conductor. This conductor served to contain the fields inside a certain region – similar to how increasing the dielectric properties or frequency also contains the fields of the SW mode. Therefore, by increasing the dielectric properties and.or operating frequency, the SW mode can effectively be modelled as a *lower* PPW mode (in the dielectric), instead of an *upper* PPW mode in the vacuum above the EBG surface. This is a critical development, since it has been shown that the lower PPW mode in a dielectric generally experiences much deeper and wider bandgaps than those in the upper PPW mode (typically in a vacuum). Therefore, simply by making a subtle change such as a change in operating frequency from the L-band to X-band, the EBG can be made *much more effective* at suppressing the SW mode, while maintaining the electrical size of the EBG.

This was demonstrated via the previously introduced antenna transmission test – one was completed at 1.5 GHz on a 60 mil substrate with an ϵ of 4.4, while the other was completed at 10 GHz on a 300 mil substrate with an ϵ of 10.2. Microstrip path antennas of resonant length approximately $\lambda_g/2$ were used and spaced apart by $4\lambda_g$ center to center, and three rows UC-EBG structures of length $\lambda_g/2$ were placed in between these patch antennas, as shown in Figs. B.8a (without EBGs) and B.8b (with EBGs). It should be noted that higher order modes are not present, with the cutoff the TM_1 SW mode well above 10 GHz for the case of $\epsilon = 10.2$.

The results of these simulations are shown in Figs. B.9a (L-band) and B.9b (X-band). As expected, since

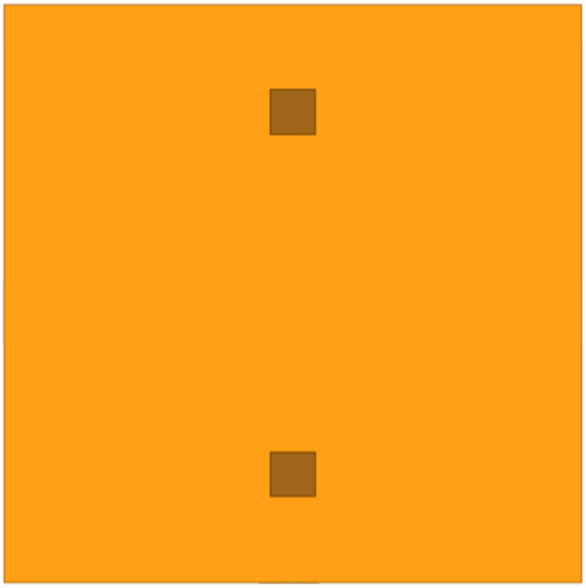

(a)

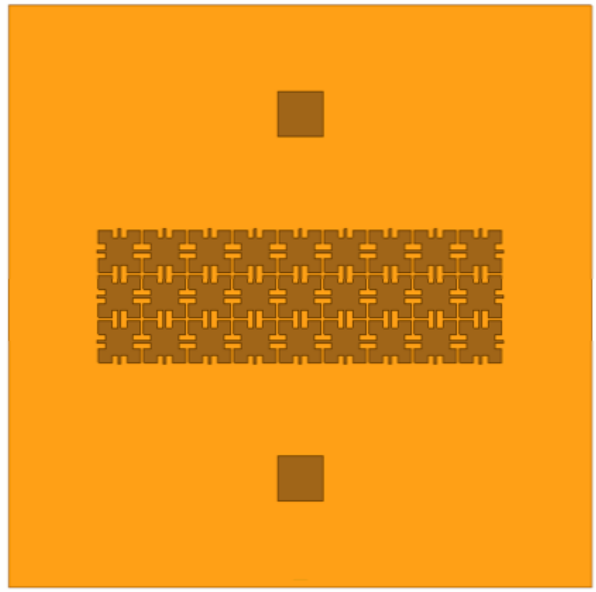

(b)

Figure B.8: Setup of the antenna transmission test, a) without EBGs, b) with EBGs.

the EC-EBGs are designed to suppress the PPW mode, there is nearly no change at L-band where the SW mode is loosely bound, but there is a distinct difference over a large bandwidth at X-band, where the SW mode is tightly bound to the dielectric and therefore imitates the PPW mode. This is why such a test does not work at L-band: even if the UC-EBG was designed to operate in its SW bandgap, the loosely bound nature of the SW mode would not cause much of a difference (which corresponds to the approximately 5 dB drop in S_{21} around 1.45 GHz).

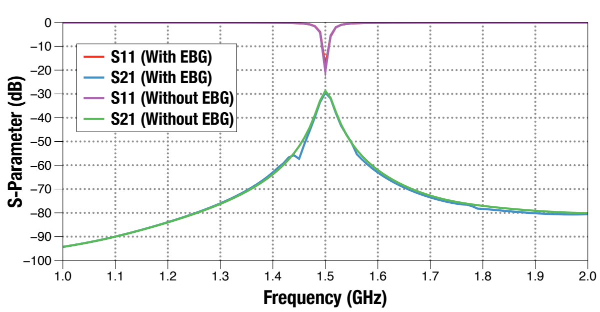

(a)

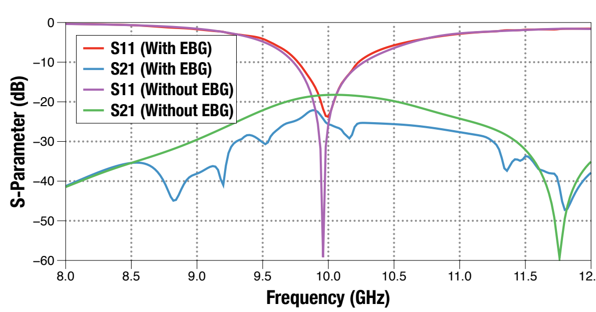

(b)

Figure B.9: Scattering parameters of the antenna transmission test at: a) L-band, b) X-band.

Appendix C

Modelling the TM_0 Surface-Wave Mode

The extension of this theory to encompass the SW mode requires additional investigation. It is well known that only TEM modes may be modelled using TL theory. However, non-TEM modes may be approximated as TEM if the fields are sufficiently similar, e.g., microstripline waveguides are not strictly TEM, but are considered *quasi*-TEM.

The analysis of the SW mode on metallic conductors of finite conductivity reveals that in the low frequency end of the microwave spectrum, these waves have a very small rate of decay away from the surface. Specifically, from [10],

$$\alpha_{SW} \approx \frac{\omega}{c}\sqrt{\frac{\omega\epsilon_0}{2\sigma}} \tag{C.1}$$

where α is the rate of decay away from a metal-air interface, and σ is the conductivity of the metal. From copper, with a bulk conductivity $\sigma_{Cu} = 5.8 \times 10^7 S/m$ at 10 GHz, the decay constant evaluates to 0.015 Np/m – indicating that the electric fields are essentially uniform in close vicinity to the surface. This is the origin of the description of the SW mode as “loosely bound” at these frequencies. At a distance of 100mm, the field strength is only 0.15% smaller than at the surface. This type of field distribution is very similar to a PPW mode, in which the electric field is constant between the plates and uniform in the transverse plane. Therefore, the SW mode should be well approximated by a PPW mode.

The properties of this PPW (i.e., filling dielectric constant and distance between the plates) can be determined by observing the properties of the SW mode. Firstly, the phase constant of the PPW mode is the same as that of the dielectric between the plates. The phase constant of the SW mode is given at microwave frequencies as

$$\beta_{SW} \approx \frac{\omega}{c} \tag{C.2}$$

from which it becomes apparent that a vacuum (air) filled PPW is desired.

Secondly, the height of the PPW is determined by observing the differences in an FEM simulation (described further in Sec. 2.5) between a Sievenpiper structure with an open boundary above it and the

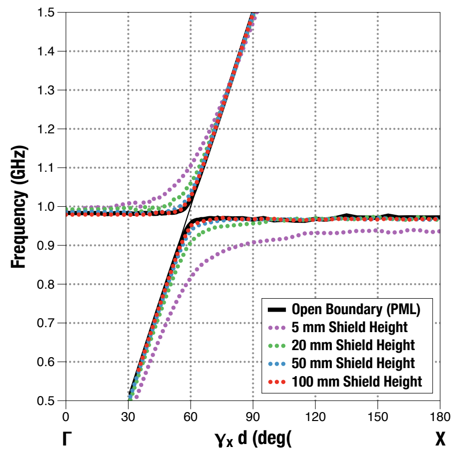

Figure C.1: FEM dispersion simulation of a Sievenpiper mushroom unit cell with a variable shield height vs open boundary, demonstrating effect of shield height on the SW bandgap.

equivalent Sievenpiper structure with a shield above it at a varying height, which will support the proposed PPW mode. The resulting data from this parametric sweep is shown in Fig. C.1, in which it can be seen that using a shield height of greater than or equal to 100mm (0.3 λ_0) seems to yield an adequately accurate dispersion. Therefore, it becomes apparent that an air-filled PPW region of sufficiently large height is an adequate model for the quasi-TEM SW mode.

Bibliography

[1] Y. Park, A. Herschlein, W. Wiesbeck, "A Photonic Bandgap (PBG) Structure for Guiding and Suppressing Surface Waves in Millimeter-Wave Antennas", IEEE Transactions on Microwave Theory and Techniques, Vol 49, No. 10, 2001.

[2] A. Grbic, G.V. Eleftheriades, "Subwavelength Focusing Using a Negative-Refractive-Index Transmission Line Lens", IEEE Antennas and Wireless Propagation Letters, Vol. 2, No. 1, 2003.

[3] J. Garcia-Garcia, J. Bonache, I. Gil, F. Martin, M. d. C. Velazquez-Ahumada, J. Martel, "Miniaturized Microstrip and CPW Filters Using Coupled Metamaterial Resonators", IEEE Transactions on Microwave Theory and Techniques, Vol 54, No. 6, 2006.

[4] M. A. Antoniades, G. V. Eleftheriades, "A CPS Leaky-Wave Antenna With Reduced Beam Squinting Using NRI-TL Metamaterials", IEEE Transactions on Antennas and Propagation, Vol. 56, No. 3, 2008.

[5] F. Yang, Y. Rahmat-Samii, "Microstrip Antennas Integrated with Electromagnetic Band-Gap (EBG) Structures: A Low Mutual Coupling Design for Array Applications", IEEE Transactions on Antennas and Propagation, Vol. 51, No. 10, 2003.

[6] H. Mosallaei, K. Sarabandi, "Magneto-Dielectrics in Electromagnetics: Concept and Applications", IEEE Transactions on Antennas and Propagation, Vol. 52, No. 6, 2004.

[7] S. D. Rogers, "Electromagnetic-Bandgap Layers for Broad-Band Suppression of TEM Modes in Power Planes", IEEE Transactions on Microwave Theory and Techniques, Vol. 53, No. 8, 2005.

[8] T. Wu, S. Chen, "A Photonic Crystal Power/Ground Layer for Eliminating Simultaneously Switching Noise in High-Speed Circuit", IEEE Transactions on Microwave Theory and Techniques, Vol. 54, No. 8, 2006.

[9] J. Garcia-Garcia, J. Bonache, F. Martin, "Application of Electromagnetic Bandgaps to the Design of Ultra-Wide Bandpass Filters With Good Out-of-Band Performance", IEEE Transactions on Microwave Theory and Techniques, Vol. 54, No. 12, 2006.

[10] D. Sievenpiper, L. Zhang, R. F. J. Broas, N. G. Alexopolous, and E. Yablonovitch, "High-Impedance Electromagnetic Surfaces with a Forbidden Frequency Band", IEEE Transactions on Microwave Theory and Techniques, Vol. 47, No. 11, 1999.

[11] E.M.A. Oliveira, S.N. Makarov, "Simple Bandwidth Estimates for Sievenpiper Mushroom Surfaces as Related to Relative Dimensions", IEEE Antennas and Propagation Society International Symposium, 2008.

[12] F. Elek, G. Eleftheriades, "Simple Analytical Dispersion Equations for the Shielded Sievenpiper Structure", IEEE MTT-S International Microwave Symposium Digest, 2006.

[13] D. F. Sievenpiper, J. H. Schaffner, H. J. Song, R. Y. Loo, G. Tangonan, "Two-Dimensional Beam Steering Using an Electrically Tunable Impedance Surface", IEEE Transactions on Antennas and Propagation, Vol. 51, No. 10, 2003.

[14] S. Clavijo, R. E. Diaz, W. E. McKinzie III, "Design Methodology for Sievenpiper High-Impedance Surfaces: An Artificial Magnetic Conductor for Positive Gain Electrically Small Antennas", IEEE Transactions on Antennas and Propagation, Vol. 51, No. 10, 2003.

[15] H. Mosallaei, K. Sarabandi, "Antenna Miniaturization and Bandwidth Enhancement Using a Reactive Impedance Substrate", IEEE Transactions on Antennas and Propagation, Vol. 52, No. 9, 2004.

[16] G. Zhang, Y. Fu, C. Zhu, D. Yan, N. Yuan, "A Circular Waveguide Antenna Using High-Impedance Ground Plane", IEEE Antennas and Wireless Propagation Letters, Vol. 2, No. 1, 2003.

[17] G. A. Kouzaev, *Applications of Advanced Electromagnetics: Components and Systems* Springer-Verlag Berlin Heidelberg, 2013.

[18] G. Wang, E. C. Folk, F. Barlow, A. Elshabini, "Fabrication of Microvias for Multilayer LTCC Substrates", IEEE Transactions on Electronics Packaging Manufacturing, Vol. 29, No. 1, 2006.

[19] L. L. W. Leung, and K. J. Chen, "Microwave Characterization and Modeling of High Aspect Ratio Through-Wafer Interconnect Vias in Silicon Substrates", IEEE Transactions on Microwave Theory and Techniques, Vol. 53, No. 8, 2005.

[20] Z. Iluz, R. Shavit, R. Bauer, "Microstrip Antenna Phased Array With Electromagnetic Bandgap Substrate", IEEE Transactions on Antennas and Propagation, Vol. 52, No. 6, 2004.

[21] G. Goussetis, A.P. Feresidis, J.C. Vardaxoglou, "Tailoring the AMC and EBG Characteristics of Periodic Metallic Arrays Printed on Grounded Dielectric Substrate", IEEE Transactions on Antennas and Propagation, Vol. 54, No. 1, 2006.

[22] J. Baik, S. Han, C. Jeong, J. Jeong, Y. Kim, "Compact Ultra-Wideband Bandpass Filter With EBG Structure", IEEE Microwave and Wireless Components Letters, Vol. 18, No. 10, 2008.

[23] L. Li, Q. Chen, Q. Yuan, K. Sawaya, "Ultrawideband Suppression of Ground Bounce Noise in Multilayer PCB Using Locally Embedded Planar Electromagnetic Band-Gap Structures", IEEE Antennas and Wireless Propagation Letters, Vol. 8, 2009.

[24] A.E.I. Lamminen, A.R. Vimpari, J. Saily, "UC-EBG on LTCC for 60-GHz Frequency Band Antenna Applications", IEEE Transactions on Antennas and Propagation, Vol. 57, No. 10, 2009.

[25] M. A. Antoniades, G. V. Eleftheriades, "Compact Linear Lead/Lag Metamaterial Phase Shifters for Broadband Applications", IEEE Antennas and Wireless Propagation Letters, Vol. 2, No. 1, 2003.

[26] M. A. Antoniades, G. V. Eleftheriades, "A Broadband Wilkinson Balun Using Microstrip Metamaterial Lines", IEEE Antennas and Wireless Propagation Letters, Vol. 4, 2005.

[27] W. E. Kock, "Metal Lens Antennas", Proceedings of the IRE, Vol. 34, No. 11, 1946.

[28] R.E. Collin, "A Simple Artificial Anisotropic Dielectric Medium", IRE Transactions on Microwave Theory and Techniques, Vol. 6, No. 2, 1958.

[29] H. Mosallaei, K. Sarabandi, "Magneto-Dielectrics in Electromagnetics: Concept and Applications", IEEE Transactions on Antennas and Propagation, Vol. 52, No. 6, 2004.

[30] J. Brown, "Artificial Dielectrics Having Refractive Indices Less Than Unity", Proceedings of the IEE, Vol. 100, No. 3, 1953.

[31] J. B. Pendry, A. J. Holden, D. J. Robbins, W. J. Stewart, "Magnetism from Conductors and Enhanced Nonlinear Phenomena", IEEE Transactions on Microwave Theory and Techniques, Vol. 47, No. 11, 1999.

[32] E. Yablonovitch, "Inhibited Spontaneous Emission in Solid-State Physics and Electronics", Physical Review Letters, Vol. 58, No. 20, 1987.

[33] E. Yablonovitch, T. J. Gmitter, K. M. Leung, "Photonic Band Structure: The Face-Centered-Cubic Case Employing Nonspherical Atoms", Physical Review Letters, Vol. 67, No. 17, 1991.

[34] R. M. Fano, A. W. Lawson, Jr., "Microwave Filters Using Quarter-Wave Couplings", Proceedings of the IRE, Vol. 35, No. 11, 1947.

[35] R. E. Collin, *Foundations for Microwave Engineering*, 2nd Edition, Wiley-IEEE Press, 2000.

[36] G. Floquet, "Sur les Equations Differentielles Lineaires a Coefficients Periodique", Annales Scientifiques de L'Ecole Normale Superieure, Vol. 2, No. 12, 1883.

[37] D. Sjoberg, C. Engstrom, G. Kristensson, D. J. N. Wall, N. Wellander, "A Floquet-Bloch Decomposition of Maxwell's Equations Applied to Homogenization", Society for Industrial and Applied Mathematics, Multiscale Modeling & Simulation Vol. 4, No. 1, 2005.

[38] S. G. Johnson, J. D. Joannopoulos, "Introduction to Photonic Crystals: Blochs Theorem, Band Diagrams, and Gaps (But No Defects)", Accessed Online: *http://ab-initio.mit.edu/photons/tutorial/photonic-intro.pdf*, 2003.

[39] David M. Pozar, *Microwave Engineering*, John Wiley & Sons, Inc., 3rd Edition, 2005.

[40] Constantine A. Balanis, *Advanced Engineering Electromagnetics*, John Wiley & Sons, Inc., 1st Edition, 1989.

[41] L. Brilloiun, *Wave Propagation in Periodic Structures; Electric Filters and Crystal Lattices*, 2nd Edition, Dover Publications, 1953.

[42] F. Capolino *Theory and Phenomena of Metamaterials* Taylor and Francis Group, LLC, 2009.

[43] H. Haus, W. P. Huang, "Coupled-Mode Theory", Proceedings of the IEEE, Vol. 79, No. 10, 1991

[44] R. Kompfner and N. T. Williams, "Backward-Wave Tubes", Proceedings of the IRE, Vol. 41, No. 11, 1953.

[45] H. Heffner, "Analysis of the Backward-Wave Traveling-Wave Tube", Proceedings of the IRE, Vol. 42, No. 6, 1954.

[46] M. Mrozowski, *Guided Electromagnetic Waves* Research Studies Press Ltd., 1997.

[47] F. Elek, "Theory and Applications of Multiconductor Transmission-Line Analysis for Shielded Sievenpiper and Related Structures", Ph.D Thesis, Graduate Department of Electrical and Computer Engineering, University of Toronto, Toronto, ON, 2010.

[48] J. D. Joannopoulos, S. G. Johnson, J. N. Winn, R. D. Meade, *Photonic Crystals*, 2nd Edition, Princeton University Press, 1995.

[49] R. Elliott, "On the Theory of Corrugated Plane Surfaces", Transactions of the IRE Professional Group on Antennas and Propagation, Vol. 2, No. 2, 1954.

[50] P. Kildal, "Artificially Soft and Hard Surfaces in Electromagnetics", IEEE Transactions on Antennas and Propagation, Vol. 38, No. 10, 1990.

[51] F. R. Yang, K. P. Ma, Y. Qian, T. Itoh, "A Uniplanar Compact Photonic-Bandgap (UC-PBG) Structure and Its Applications for Microwave Circuits", IEEE Transactions on Microwave Theory and Techniques, Vol. 47, No. 8, 1999.

[52] F. Elek and G. V. Eleftheriades, "Dispersion Analysis of the Shielded Sievenpiper Structure Using Multiconductor Transmission-Line Theory", IEEE Microwave and Wireless Components Letters, Vol. 14, No. 9, 2004.

[53] F. Bongard, J. Perruisseau-Carrier, J. R. Mosig, "Enhanced Periodic Structure Analysis Based on a Multiconductor Transmission Line Model and Application to Metamaterials", IEEE Transactions on Microwave Theory and Techniques, Vol. 57, No. 11, 2009.

[54] K. Payandehjoo, A. Tavallaee, R. Abhari, "Analysis of Shielded Electromagnetic Bandgap Structures Using Multiconductor Transmission-Line Theory", IEEE Transactions on Advanced Packaging, Vol. 33, No. 1, 2010.

[55] Y. Qian, R. Coccioli, D. Sievenpiper, V. Radisic, E. Yablonovitch, T. Itoh, "A Microstrip Patch Antenna Using Novel Photonic Band-Gap Structures", Microwave Journal, Vol. 42, No. 1, 1999.

[56] H. Kim, B. Lee, "Bandgap and Slow/Fast-Wave Characteristics of Defected Ground Structures (DGSs) Including Left-Handed Features", IEEE Transactions on Microwave Theory and Techniques, Vol. 54, No. 7, 2006.

[57] M. Kim, K. Koo, C. Hwang, Y. Shim, J. Kim, J. Kim, "A Compact and Wideband Electromagnetic Bandgap Structure Using a Defected Ground Structure for Power/Ground Noise Suppression in Multilayer Packages and PCBs", IEEE Transactions on Electromagnetic Compatibility, Vol. 54, No. 3, 2012.

[58] N. C. Karmakar, S. M. Roy, I. Balbin, "Quasi-Static Modeling of Defected Ground Structure", IEEE Transactions on Microwave Theory and Techniques, Vol. 54, No. 5, 2006.

[59] D. J. Kern, D. H. Werner, A. Monorchio, L. Lanuzza, M. J. Wilhelm, "The Design Synthesis of Multiband Artificial Magnetic Conductors Using High Impedance Frequency Selective Surfaces", IEEE Transactions on Antennas and Propagation, Vol. 53, No. 1, 2005.

[60] E. Rodes, M. Diblanc, E. Arnaud, T. Monediere, B. Jecko, "Dual-Band EBG Resonator Antenna Using a Single-Layer FSS", IEEE Antennas and Wireless Propagation Letters, Vol. 6, 2007.

[61] A. B. Yakovlev, M. G. Silveirinha, O. Luukkonen, C. R. Simovski, I. S. Nefedov, S. A. Tretyakov, "Characterization of Surface-Wave and Leaky-Wave Propagation on Wire-Medium Slabs and Mushroom Structures Based on Local and Nonlocal Homogenization Models", IEEE Transactions on Microwave Theory and Techniques, Vol. 57, No. 11, 2009.

[62] R. Abhari, G. V. Eleftheriades, T. E. van Deventer-Perkins, "Physics-Based CAD Models for the Analysis of Vias in Parallel-Plate Environments", IEEE Transactions on Microwave Theory and Techniques, Vol. 49, No. 10, 2001.

[63] R. Senthinatan, J. Price, *Simultaneous Switching Noise of CMOS Devices and Systems*, Springer Science and Business Media 2004.

[64] S. H. Hashemi, P. A. Sandborn, D. Disko, R. Evans, "The Close Attached Capacitor: A Solution to Switching Noise Problems", IEEE Transaction on Components, Hybrids, and Manufacturing Technology, Vol. 15, No. 6, 1992.

[65] T. H. Hubing, J. L. Drewniak, T. P. Van Doren, D. M. Hockanson, "Power Bus Decoupling on Multilayer Printed Circuit Boards", IEEE Transactions on Electromagnetic Compatibility, Vol. 37, No. 2, 1995.

[66] M. Xu, T. H. Hubing, J. Chen, T. P. Van Doren, J. L. Drewniak, R. E. DuBroff, "Power-Bus Decoupling With Embedded Capacitance in Printed Circuit Board Design", IEEE Transactions on Electromagnetic Compatibility, Vol. 45, No. 1, 2003.

[67] V. Ricchiuti, "Power Bus Signal Integrity Improvement and EMI Mitigation on Multilayer High-Speed Digital PCBs with Embedded Capacitance", IEEE Transactions on Mobile Computing, Vol. 2, No. 4, 2003.

[68] W. Liu, C. Tsai, T. Han, T. Wu, "An Embedded Common-Mode Suppression Filter for GHz Differential Signals Using Periodic Defected Ground Plane", IEEE Microwave and Wireless Components Letters, Vol. 18, No. 4, 2008

[69] S. Wu, C. Tsai, T. Wu, T. Itoh, "A Novel Wideband Common-Mode Suppression Filter for Gigahertz Differential Signals Using Coupled Patterned Ground Structure", IEEE Transactions on Microwave Theory and Techniques, Vol. 57, No. 4, 2009

[70] A. B. Abdel-Rahman, "Coupling Reduction of Antenna Array Elements Using Small Interdigital Capacitor Loaded Slots", Progress In Electromagnetics Research C, Vol. 27, 2012

[71] H. S. Lee, T. Koo, T. Song, J. Yook, K. Yoo, J. Cheon, S. Lee, "A Compact Common-Mode Suppression Filter Using Modified Ground Structure for High Speed Digital Interconnects on Multi-layered PCB", Proc. of the 2014 International Symposium on Electromagnetic Compatibility, Gothenburg, Sweden, 2014

[72] T. Wu, H. Chuang, T. Wang, "Overview of Power Integrity Solutions on Package and PCB: Decoupling and EBG Isolation", IEEE Transactions on Electromagnetic Compatibility, Vol. 52, No. 2, 2010.

[73] Z. Hao, W. Hong, J. Chen, X. Chen, K. Wu, Fellow, "Compact Super-Wide Bandpass Substrate Integrated Waveguide (SIW) Filters", IEEE Transactions on Microwave Theory and Techniques, Vol. 53, No. 9, 2005.

[74] S. Shahparnia, O. M. Ramahi, "Electromagnetic Interference (EMI) Reduction From Printed Circuit Boards (PCB) Using Electromagnetic Bandgap Structures", IEEE Transactions on Electromagnetic Compatibility, Vol.46, No. 4, 2004.

[75] Official U.S. Government information about the Global Positioning System (GPS) and related topics, Website: *http://www.gps.gov/applications/*

[76] United States of America Department of Defence, *Global Positioning System Standard Positioning Service Signal Specification*, 2nd Edition, 1995, Accessed Online, *http://www.gps.gov/technical/ps/1995-SPS-signal-specification.pdf.*

[77] J. Tranquilla, J. P. Carr, H. M. Al-Rizzo, "Analysis of a Choke Ring Groundplane for Multipath Control in Global Positioning System (GPS) Applications", IEEE Transactions on Antennas and Propagation, Vol. 2, No. 4, 1994.

[78] F. Scire-Scappuzzo, S. N. Makarov, "A Low-Multipath Wideband GPS Antenna With Cutoff or Non-Cutoff Corrugated Ground Plane", IEEE Transactions on Antennas and Propagation, Vol. 57, No. 1, 2009.

[79] R. Coccioli, F. Yang, K. Ma, T. Itoh, "Aperture-Coupled Patch Antenna on UC-PBG Substrate", IEEE Transactions on Microwave Theory and Techniques, Vol. 47, No. 11, 1999.

[80] J. H. Richmond, "Propagation of Surface Waves on a Thin Resistive Sheet or a Coated Substrate", Radio Science, Vol. 22, No. 5, 1987.

[81] Shively, D. "Surface Waves on a Grounded Dielectric Slab Covered by a Resistive Sheet", IEEE Transactions on Antennas and Propagation, Vol. 41, No. 3, 1993.

[82] N. Engheta, R. W. Ziolkowski, *Metamaterials: Physics and Engineering Explorations*, John Wiley & Sons, Inc., 2006.

[83] V. G. Veselago, "The Electrodynamics of Substances with Simultaneously Negative Values of ϵ and μ", Soviet Physics Uspekhi, Vol. 10, No. 4, 1968.

[84] D. R. Smith, W. J. Padilla, D. C. Vier, S. C. Nemat-Nasser, S. Schultz, "Composite Medium with Simultaneously Negative Permeability and Permittivity", Physical Review Letters, Vol. 84, No. 18, 2000.

[85] G. V. Eleftheriades, A. K. Iyer, P. C. Kremer, "Planar Negative Refractive Index Media Using Periodically LC Loaded Transmission Lines", IEEE Transactions on Microwave Theory and Techniques, Vol. 50, No. 12, 2002.

[86] A. Sanada, C. Caloz, T. Itoh, "Characteristics of the Composite Right/Left-Handed Transmission Lines", IEEE Microwave and Wireless Components Letters, Vol. 14, No. 2, 2004.

[87] Clayton R. Paul, *Analysis of Multiconductor Transmission Lines*, John Wiley & Sons, Inc., 1994.

[88] C. R. Paul, "Decoupling the Multiconductor Transmission Line Equations", IEEE Transactions on Microwave Theory and Techniques, Vol. 44, No. 8, 1996.

[89] C. R. Paul, and A. E. Feather, "Computation of the Transmission Line Inductance and Capacitance Matrices from the Generalized Capacitance Matrix", IEEE Transactions on Electromagnetic Compatibility, Vol. 18, No. 4, 1976.

[90] J.R. Silvester, "Determinants of Block Matrices", The Mathematical Gazette, Vol. 84, No. 501, 2000.

[91] J. A. Brando Faria, "On the Transmission Matrix of 2n-Port Reciprocal Networks", Microwave and Optical Technology Letters, Vol. 33, No. 3, 2002.

[92] ANSYS, *High Frequency Structural Simulator*, v. 15.0.3, 2013.

[93] S. D. Assimonis, T. V. Yioultsis, C. S. Antonopoulos, "Computational Investigation and Design of Planar EBG Structures for Coupling Reduction in Antenna Applications", IEEE Transactions on Magnetics, Vol. 48, No. 2, 2012.

[94] N. Llombart, A. Neto, G. Gerini, and P. de Maagt, “Planar Circularly Symmetric EBG Structures for Reducing Surface Waves in Printed Antennas”, IEEE Transactions on Antennas and Propagation, Vol. 53, No. 10, 2005.

[95] H. Boutayeb, T. A. Denidni, “Gain Enhancement of a Microstrip Patch Antenna Using a Cylindrical Electromagnetic Crystal Substrate”, IEEE Transactions on Antennas and Propagation, Vol. 55, No. 11, 2007.

[96] G. Ruvio, M.J. Ammann, X. Bao, “Radial EBG Cell Layout for GPS Patch Antennas”, Electronics Letters, Vol. 45, No. 13, 2009.

[97] G. Feng, J. Fan, “Analysis of Simultaneous Switching Noise Coupling in Multilayer Power/Ground Planes With Segmentation Method and Cavity Model”, IEEE Transactions on Electromagnetic Compatibility, Vol. 52, No. 3, 2010.

[98] M. Pasian, M. Bozzi, L. Perregrini, “Crosstalk in Substrate Integrated Waveguides”, IEEE Transactions on Electromagnetic Compatibility, Vol. 57, No. 1, 2014.

[99] D. Deslandes, K. Wu, “Accurate Modeling, Wave Mechanisms, and Design Considerations of a Substrate Integrated Waveguide”, IEEE Transactions on Microwave Theory and Techniques, Vol. 54, No. 6, 2006.

[100] A. Bhattacharyya, O. Fordham, Y. Liu, “Analysis of Stripline-Fed Slot-Coupled Patch Antennas with Vias for Parallel-Plate Mode Suppression”, IEEE Transactions on Antennas and Propagation, Vol. 46, No. 4, 1998.

[101] L. D. Smith, R. E. Anderson, D. W. Forehand, T. J. Pelc, T. Roy, “Power Distribution System Design Methodology and Capacitor Selection for Modern CMOS Technology”, IEEE Transaction on Advanced Packaging, Vol. 22, No. 3, 1999.

[102] A. Madou, L. Martens, “Electrical Behavior of Decoupling Capacitors Embedded in Multilayered PCBs”, IEEE Transactions on Electromagnetic Compatibility, Vol. 43, No. 4, 2001

[103] M. Xu, Member, T. H. Hubing, J. Chen, T. P. Van Doren, J. L. Drewniak, R. E. DuBroff, “Power-Bus Decoupling With Embedded Capacitance in Printed Circuit Board Design”, IEEE Transactions on Electromagnetic Compatibility, Vol. 45, No. 1, 2003.

[104] M. Swaminathan, J. Kim, I. Novak, J. P. Libous, “Power Distribution Networks for System-on-Package: Status and Challenges”, IEEE Transaction on Advanced Packaging, Vol. 27, No. 2, 2004.

[105] X. Tian, Y. Zhang, D. Liu, L. Gui, Q. Li, J. Fan, “Efficient Analysis of Power/Ground Planes Loaded With Dielectric Rods and Decoupling Capacitors by Extended Generalized Multiple Scattering Method”, IEEE Transactions on Electromagnetic Compatibility, Vol. 57, No. 1 2015.

[106] R. Abhari, and G. V. Eleftheriades, "Metallo-Dielectric Electromagnetic Bandgap Structures for Suppression and Isolation of the Parallel-Plate Noise in High-Speed Circuits", IEEE Transactions on Microwave Theory and Techniques, Vol. 51, No. 6, 2003.

[107] T. Wu, Y. Lin, T. Wang, C. Wang, S. Chen, "Electromagnetic Bandgap Power/Ground Planes for Wideband Suppression of Ground Bounce Noise and Radiated Emission in High-Speed Circuits", IEEE Transactions on Microwave Theory and Techniques, Vol. 53, No. 9, 2005.

[108] J. Qin, O. M. Ramahi, "Ultra-Wideband Mitigation of Simultaneous Switching Noise Using Novel Planar Electromagnetic Bandgap Structures", IEEE Antennas and Wireless Components Letters, Vol. 16, No. 9, 2006.

[109] Y. Toyota, A. E. Engin, T. H. Kim, M. Swaminathan, "Stopband Analysis Using Dispersion Diagram for Two-Dimensional Electromagnetic Bandgap Structures in Printed Circuit Boards", IEEE Microwave and Wireless Components Letters, Vol. 16, No. 12, 2006.

[110] T. Wu, H. Chuang, T. Wang, "Overview of Power Integrity Solutions on Package and PCB: Decoupling and EBG Isolation", IEEE Transactions on Electromagnetic Compatibility, Vol. 52, No. 2, 2010.

[111] Y. He, C. Liang, Q. H. Liu, "Novel Array EBG Structures for Ultrawideband Simultaneous Switching Noise Suppression", IEEE Antennas and Wireless Propagation Letters, Vol. 10, 2011.

[112] H. M. Lu, J. X. Zhao, Z. Y. Yu, "Design and Analysis of a Novel Electromagnetic Bandgap Structure for Suppressing Simultaneous Switching Noise", Progress In Electromagnetics Research C, Vol. 30, 2012.

[113] J. N. Tripathi, J. Mukherjee, P. R. Apte, R. K. Nagpal, N. K. Chhabra, R. Malik, "A Novel EBG Structure with Super-Wideband Suppression of Simultaneous Switching Noise in High Speed Circuits", IEEE 22nd Conference on Electrical Performance of Electronic Packaging and Systems, 2013.

[114] Z. Yan, Y. Xiong, W. Yu, Y. Wang, "An Improved Miniaturized Three-Layer Embedded Electromagnetic Bandgap Structure", IEEE Transactions on Antennas and Propagation, Vol. 62, No. 5, 2014.

[115] LPKF Laser & Electronics AG, Garbsen, Germany, Website: http://www.lpkf.com.

[116] B. R. Rao, J. H. Williams, E. N. Rosario, R. J. Davis, "GPS Microstrip Antenna Array on a Resistivity Tapered Ground Plane for Multipath Mitigation", MITRE Corporation, Accessed Online: *http://www.mitre.org/sites/default/files/pdf/rao_microstrip.pdf*, 2000.

[117] C.C. Tchapwou, T. Bertuch, "Investigation of EBG Surface Performance for High-Precision GPS Applications", Electronics Letters, Vol. 43, No. 24, 2007.

[118] R. Baggen, M. Martinez-Vazquez, J. Leiss, S. Holzwarth, L. S. Drioli, P. de Maagt, "Low Profile GALILEO Antenna Using EBG Technology", IEEE Transactions on Antennas and Propagation, Vol. 56, No. 3, 2008.

[119] H. Lin, K. Lin, C. Kuo, Y. Huang, "Receiving Performance Enhancement of Active GPS Antenna with Periodic Structure", Progress In Electromagnetics Research Symposium Proceedings, 2011.

[120] X. L. Bao, G. Ruvio, M. J. Ammann, M. John, "A Novel GPS Patch Antenna on a Fractal Hi-Impedance Surface Substrate", IEEE Antennas and Wireless Propagation Letters, Vol. 5, 2006.

[121] R. Baggen, M. Martinez-Vazquez, J. Leiss, S. Holzwarth, "Comparison of EBG Substrates With and Without Vias for GALILEO/GPS Applications", The Second European Conference on Antennas and Propagation, 2007.

[122] J. Baracco, L. Salghetti-Drioli, P. de Maagt, "AMC Low Profile Wideband Reference Antenna for GPS and GALILEO Systems", IEEE Transactions on Antennas and Propagation, Vol. 56, No. 8, 2008.

[123] W. E. McKinzie III, "On the Surface Wave Properties of Sievenpiper-Type Metamaterial Absorbers", IEEE Antennas and Propagation Society International Symposium, 2009.

[124] F. Yang, K. Ma, Y. Qian, T. Itoh, "A Novel TEM Waveguide Using Uniplanar Compact Photonic-Bandgap (UC-PBG) Structure", IEEE Transactions on Microwave Theory and Techniques, Vol. 47, No. 11, 1999.

[125] J. K. A. Everard, K. K. M. Cheng, "High Performance Direct Coupled Bandpass Filters on Coplanar Waveguide", IEEE Transactions on Microwave Theory and Techniques, Vol. 41, No. 9, 1993.

[126] G. D. Alley, "Interdigital Capacitors and Their Application to Lumped-Element Microwave Integrated Circuits", IEEE Transactions on Microwave Theory and Techniques, Vol. 18, No. 12, 1970.

[127] NovAtel, Inc. Calgary, Alberta, Canada, Website: http://www.novatel.com.

[128] A. K. Iyer, G. V. Eleftheriades, "Volumetric Layered Transmission-Line Metamaterial Exhibiting a Negative Refractive Index", Journal of the Optical Society of America B, Vol. 23, No. 3, 2006.

[129] A. Grbic, G. V. Eleftheriades, "Periodic Analysis of a 2-D Negative Refractive Index Transmission Line Structure", IEEE Transactions on Antennas and Propagation, Vol. 51, No. 10, 2003.

[130] F. Yang, Y. Rahmat-Samii, "Reflection Phase Characterizations of the EBG Ground Plane for Low Profile Wire Antenna Applications", IEEE Transactions on Antennas and Propagation, Vol. 51, No. 10, 2003.

[131] M. Fan, R. Hu, Q. Hao, X. Zhang, Z. Feng, "Advance in 2D-EBG Structrues' Research", Journal of Infrared Millimeter Waves, Vol. 22, No. 2, 2003.

[132] A. Aminian, F. Yang, Y. Rahmat-Samii, "In-phase Reflection and EM Wave Suppression Characteristics of Electromagnetic Band Gap Ground Planes", IEEE Antennas and Propagation Society International Symposium, 2003.

[133] S. Raza, "Characterization of the Reflection and Dispersion Properties of Mushroom-Related Structures and Their Application to Antennas", M.A.Sc. Thesis, Graduate Department of Electrical And Computer Engineering, University of Toronto, Toronto, Canada, 2012.